



University of  
Massachusetts  
Amherst

## Impact Resistant Glassy Polymers: Pre-Stress And Mode I Fracture

Item Type	dissertation
Authors	Archer, Jared Steven
DOI	<a href="https://doi.org/10.7275/bgsb-8k74">10.7275/bgsb-8k74</a>
Download date	2024-11-27 02:09:01
Link to Item	<a href="https://hdl.handle.net/20.500.14394/39129">https://hdl.handle.net/20.500.14394/39129</a>

IMPACT RESISTANT GLASSY POLYMERS: PRE-STRESS AND MODE II  
FRACTURE

A Dissertation Presented

By

JARED STEVEN ARCHER

Submitted to the Graduate School of the University of Massachusetts  
Amherst in partial fulfillment of the requirements for the degree of

DOCTOR OF PHILOSOPHY

2013

Polymer Science and Engineering

© Copyright by Jared Steven Archer 2013

All Rights Reserved

IMPACT RESISTANT GLASSY POLYMERS: PRE-STRESS AND MODE II  
FRACTURE

A Dissertation Presented

By

JARED STEVEN ARCHER

Approved as to style and content by:

---

Alan J. Lesser, Chair

---

Alfred J. Crosby, Member

---

H. Henning Winter, Member

---

David A. Hoagland

Department Head

DEDICATION

To my loving wife for her patience and support

*lapidem vulpes*

## ACKNOWLEDGMENTS

This thesis would not have been possible without the help of many people. First of all, I would like to thank my advisor, Professor Alan Lesser for his support during my time at UMass. He has taught me many things from effective presentation skills to implementation of creative solutions to experimental quandaries. I have also received helpful feedback and support from my committee members, Professors Alfred Crosby and Henning Winter.

I would like to thank the members of the Lesser group, both past and present. The many discussions we have had in group meetings as well as in informal interactions in the lab were always stimulating and beneficial.

I would especially like to thank my wife, Jessica, for being a constant source of love and encouragement throughout this work. She means the world to me and I couldn't have done this without her.

ABSTRACT

IMPACT RESISTANT GLASSY POLYMERS: PRE-STRESS AND MODE II  
FRACTURE

FEBRUARY 2013

JARED STEVEN ARCHER

B.S., WESTERN WASHINGTON UNIVERSITY

M.S., UNIVERSITY OF MASSACHUSETTS AMHERST

Ph.D., UNIVERSITY OF MASSACHUSETTS AMHERST

Directed by: Professor Alan J. Lesser

Model glassy polymers, polymethyl methacrylate (PMMA) and polycarbonate (PC) are used to experimentally probe several aspects of polymer fracture. In Chapter 1, the method of pre-stress is employed as a means of improving the fracture properties of brittle PMMA. Samples are tested under equi-biaxial compression, simple shear and a combination of biaxial compression and shear. Equi-biaxial compression is shown to increase the threshold stress level for projectile penetration whereas shear pre-stress has a large effect on the overall energy absorbed during an impact. There is also an apparent interaction observed between compression and shear to dramatically increase the threshold stress. Pre-stressed laminates of PMMA and PC show an increase in damage area because of the unique formation of a secondary cone.

In Chapter 2, the effect of stress state on stress relaxation in PMMA and PC is investigated. Direct comparisons are made between uniaxial and biaxial loading conditions. The experimental methods used highlight the effect of hydrostatic stress on the relaxation process. The data shows an increase in relaxation time and increase in the breadth of the relaxation spectrum with increases in hydrostatic stress. This suggests that the stress state can have a significant effect on the useful lifetime of pre-stressed articles.

In Chapter 3, Mode I and II fracture studies are performed from quasi-static to low velocity impact rates on PMMA and PC. Mode II testing utilizes an angled double-edge notched specimen loaded in compression. The shear banding response of PMMA is shown to be highly sensitive to rate, with diffuse shear bands forming at low rates and sharp distinct shear bands forming at high rates. As the rate increases, shear deformation becomes more localized to the point where Mode II fracture occurs. PC is much less rate dependent and stable shear band propagation is observed over the range of rates studied with lesser amounts of localization. A new theory is formulated relating orientation in a shear band to intrinsic material properties obtained from true-stress true-strain tests. In a qualitative sense the theory predicts the high rate sensitivity of PMMA. A kinematic limit for orientation within a shear band is also derived based on entanglement network parameters. Mode II

fracture in PMMA is shown to occur at this kinematic limit. For the case of PC, the maximum impact rates were not high enough to reach the kinematic limit.

In Chapter 4, the deformation response, as observed in a shear band is interpreted through the characterization of the “intrinsic material properties” obtained from true stress - true strain & compression tests. The relatively high rate sensitivity of PMMA deformed at room temperature is related to the proximity of the beta transition to the test temperature. This is also shown in corollary experiments on PC where deformation near the beta transition is accompanied by an increase in rate sensitivity. Physical aging results in a more narrow alpha transition and is shown to increase strain localization and decrease rate sensitivity at low strain rates.

# TABLE OF CONTENTS

<b>ACKNOWLEDGMENTS.....</b>	<b>v</b>
<b>ABSTRACT.....</b>	<b>vi</b>
<b>LIST OF TABLES .....</b>	<b>xii</b>
<b>LIST OF FIGURES .....</b>	<b>xiii</b>

## CHAPTER

### **1. IMPACT RESISTANT GLASSY POLYMERS USING COMPRESSIVE PRE-STRESS .....1**

<b>Abstract .....</b>	<b>1</b>
<b>Introduction.....</b>	<b>1</b>
<b>Experimental .....</b>	<b>6</b>
<b>Materials .....</b>	<b>6</b>
<b>Application of Pre-Stress.....</b>	<b>6</b>
<b>Results and Discussion .....</b>	<b>13</b>
<b>Low-Velocity Failure Mechanism .....</b>	<b>13</b>
<b>High-Velocity Failure Mechanism .....</b>	<b>15</b>
<b>Impact Energy .....</b>	<b>16</b>
<b>Threshold .....</b>	<b>21</b>
<b>Effect of shear .....</b>	<b>23</b>
<b>Pre-stressed transparent composite laminates .....</b>	<b>25</b>
<b>Conclusions .....</b>	<b>29</b>
<b>References .....</b>	<b>29</b>

### **2. EFFECT OF HYDROSTATIC STRESS ON STRESS RELAXATION IN GLASSY POLYMERS .....33**

<b>Abstract .....</b>	<b>33</b>
-----------------------	-----------

Introduction.....	33
Materials .....	34
Experimental .....	35
Relaxation.....	36
Results and Discussion .....	37
Conclusions .....	47
References .....	48

### **3. SHEAR BAND FORMATION AND MODE II FRACTURE OF GLASSY POLYMERS.....50**

Abstract .....	50
Introduction.....	51
Mode II Fracture .....	53
Materials .....	55
Experimental .....	56
Mode I Fracture.....	56
Mode II Deformation and Fracture .....	57
Compression.....	61
Results and Discussion .....	64
Mode I.....	64
Mode II - General Observations .....	69
Intrinsic Material Properties .....	78
Condition For Shear Band Stability .....	78
Kinematic Limit.....	83
Conclusions .....	88

### **References .....89**

### **4. RATE SENSITIVITY OF STRAIN LOCALIZATION IN GLASSY POLYMERS.....93**

Abstract .....	93
Introduction.....	93
Experimental .....	103

Materials .....	103
Compression Testing.....	104
Shear Deformation .....	105
Results and Discussion .....	105
Test Temperature and the Beta Relaxation.....	108
Physical Aging.....	116
Conclusions .....	121
References .....	123
<b>APPENDIX: SHEAR BAND CALCULATIONS AND SUPPLEMENTAL STRESS STRAIN DATA .....</b>	<b>127</b>
<b>BIBLIOGRAPHY .....</b>	<b>146</b>

## LIST OF TABLES

Table	Page
2-1. Summary of relaxation experiments.....	37
2-2 Coded values for regression analysis.....	45
2-3 Summary of regression analysis on relaxation time.....	46
2-4 Summary of regression analysis on stretching exponent.....	46
3-1. Summary of compression testing on PMMA 930 kg/mol.....	75
3-2. Summary of compression testing on PC.....	75
3-3. Required Temperature Increase to Achieve Observed Orientation for PC.....	83
3-4. Required Temperature Increase to Achieve Observed Orientation for PMMA.....	83
4-1. Ratio of isotactic meso-meso ( <i>mm</i> ), atactic meso-racemo ( <i>mr</i> ) and syndiotactic racemo-racemo ( <i>rr</i> ) triads from NMR.....	103

## LIST OF FIGURES

Figure	Page
1-1. Square frame with overlaid image of pre-stressed sample viewed under crossed polars. Scale bar = 25 mm. ....	7
1-2. Schematic of simple shear pre-stress method.....	8
1-3. (a) Shrink fit sample. (b) Shrink fit sample viewed between crossed polars. Scale bars = 25 mm. ....	9
1-4. Dimensions used in shrink fit calculations. ....	10
1-5. Low velocity (~ 2 m/s) failure mechanism. In the control sample, the dominant mechanism is radial cracks. Under pre-stress, cone fracture is most visible. Underlying grid unit = 12.7 mm. ....	13
1-6. Low velocity mechanism change. Top row (frame rate = 4500 fps) - control sample exhibits large radial cracks as well as cone fracture. Bottom row (frame rate = 40,500 fps) - pre-stressed sample shows stunted radial crack growth. Unit of time = ms. Diameter of circular boundary in all images = 42 mm.....	14
1-7. Ballistic impact (\$ 130 m/s) on monolithic plates. Significant reduction of radial cracking seen with pre-stress.....	15
1-8. Effect of pre-stress on impact energy.....	16
1-9. Radial crack surface area for energy estimates. Sample thickness = 5.75 mm.....	17
1-10. Comparative load-deflection curve. Failure mechanism initiation observed by high speed photography.....	18
1-11. Effect of pre-stress on threshold.....	22
1-12. Fractography of radial crack surface for (a) shrink fit sample, (b) shear pre-stressed sample near impact, and (c) shear pre-stressed sample away from impact. All scale bars = 500 $\mu\text{m}$ .....	24
1-13. Surface roughness of radial cracks on shear pre-stressed samples. ....	25

1-14. Effect of shear pre-stress on impact energy and threshold.....	26
1-15. Top image cross section of PC/PMMA/PC laminate using solvent welding on both plies showing secondary cone and brittle fracture of PC distal ply. Bottom images PC/PMMA/PC laminate using solvent welding on impacted ply and polyurethane on opposing ply shows secondary cone as well as containment of PMMA spall. Cone diameter ~50 mm.....	27
1-16. Control laminate - no secondary cone formation. ....	28
2-1. Comparison of uniaxial and biaxial stress relaxation in 930 kg/mol PMMA. ....	38
2-2. Effect of stress state on relaxation time in 930 kg/mol PMMA.....	38
2-3. Effect of stress state on stretching exponent, $\beta$ in 930 kg/mol PMMA. ....	39
2-4. Stress relaxation under uniaxial tension and biaxial compression for PMMA 1,100 kg/mol. ....	39
2-5. Effect of stress state on relaxation time in 1,100 kg/mol PMMA. ....	40
2-6. Stretching parameter $\beta$ from KWW fit for PMMA 1,100 kg/mol. ....	40
2-7. Stress relaxation under uniaxial tension and biaxial compression for PC. ....	41
2-8. Relaxation time from KWW fit for PC. ....	41
2-9. Stretching parameter $\beta$ from KWW fit for PC.....	42
3-1. Cracked Brazilian Disc of PMMA loaded in pure Mode II. Mode I cracks initiate at an angle of $72^\circ$ relative to the pre-crack as predicted by the MTS criterion illustrating that $K_{IIC} > K_{IC}$ . Disc diameter = 101 mm....	54
3-2. Mode II sample dimensions. Thickness = 6 mm.....	56
3-3. Support jig to prohibit buckling during compressive loading in Mode II tests. Center hole is for illuminating and viewing sample deformation.....	58

3-4. Shear strain as measured from image analysis vs. time used to calculate maximum shear strain rate and maximum shear strain. ....	59
3-5. Intrinsic material properties obtained from true-stress true-strain compression tests. $\sigma_y$ , $\sigma_r$ , $G_R$ , and $k_y$ represent the yield stress, rejuvenated stress, strain hardening modulus and strain localization parameter respectively.....	60
3-6. Mode I fracture toughness of PMMA and PC. ....	61
3-7. Mode I fracture surface morphology in PMMA. Numbers indicate impact rate in mm/min. Crack growth is from left to right. Vertical lines in bottom three images indicate boundary of parabolic markings. The height of each image = 1.3 mm. ....	62
3-8. Arrows indicate Mode I kinks. Diameter = 12.7 mm. ....	63
3-9. Effect of rate on shear band formation. First row PC, second and third rows PMMA. Numbers in first two rows indicate shear strain rate in $\text{min}^{-1}$ . Diameter in each image = 12.7 mm. ....	64
3-10. Maximum shear strain vs. shear strain rate for PC and PMMA.....	65
3-11. PMMA prior to complete Mode II fracture viewed under crossed polars. Black lines at $45^\circ$ are surface marks for surface displacement reference. Shear band is identified by offset in reference lines. Shallow micro-tensile cracks form at $\sim 45^\circ$ to shear bands. Scale bar = $500 \mu\text{m}$ ....	66
3-12. Map of birefringence of shear bands in PMMA prior to complete Mode II fracture. The level of birefringence is represented by the continuous grayscale in the image (black = 0, white = $3.34 \times 10^{-4}$ ). Spatial scale bar = $500 \mu\text{m}$ . The arrow indicates the location for the line scan of birefringence shown in Figure 3-13.....	67
3-13. Spatial line scan of birefringence of shear band in PMMA. ....	68
3-14. SEM image of Mode II fracture surface of PMMA. ....	69
3-15. Relationship of sample compliance to crack length for Mode II specimens.....	70
3-16. Mode II critical strain energy release rate for PMMA.....	71

3-17. Comparison of Mode I and II fracture toughness in PMMA.....	72
3-18. True-stress true-strain response of PMMA.....	73
3-19. True-stress true-strain response of PC.....	74
3-20. Predicted relationship between intrinsic material properties and orientation within a shear band. Contour lines represent steps in $k_y$ . Arrows indicate direction of increasing strain rate.....	81
3-21. Molecular network parameters used to define $\gamma_{max}$ in shear.....	84
3-22. Relative rate dependence of yield stress and strain hardening modulus for PC.....	86
3-23. Relative rate dependence of yield stress and strain hardening modulus for PMMA. ....	87
3-24. Rate dependence of the post yield stress drop (PYSD) normalized by strain hardening modulus ( $G_R$ ).....	88
4-1. Dynamic mechanical analysis on PC at 1 Hz and 10 Hz. The high toughness and ductility in PC is attributed to the low beta transition temperature.....	94
4-2. Dynamic mechanical analysis of PMMA 930k at 1 Hz and 10 Hz.....	95
4-3. Tacticity measurements by NMR.....	98
4-4. Copolymer composition determined by NMR. ....	99
4-5. PMMA 930 kg/mol $\tan \delta$ at different frequencies as a function of temperature. ....	100
4-6. PMMA 930 kg/mol activation energies for alpha and beta transitions. ....	100
4-7. PMMA 1,100 kg/mol $\tan \delta$ at different frequencies as a function of temperature. ....	101
4-8. PMMA 1,100 kg/mol activation energies for alpha and beta transitions. ....	101

4-9. PMMA- <i>co</i> -EA tan $\delta$ at different frequencies as a function of temperature. ....	102
4-10. PMMA- <i>co</i> -EA activation energies for alpha and beta transitions. ....	102
4-11. Predicted levels of shear strain based on values of $\sigma_y$ , $k_y$ and $G_R$ as measured by compression tests. The two PMMA homopolymers have very similar rate dependencies. PMMA- <i>co</i> -EA has less rate dependence at the highest strain rates and levels of localization intermediate to the homopolymers. All at 23° C. ....	105
4-12. Rate dependence of strain localization in shear bands for acrylic polymers. The two PMMA homopolymers have very similar rate dependencies. PMMA- <i>co</i> -EA has less rate dependence.....	106
4-13. Predicted shear strain for PMMA 930k at room temperature and at 80° C (above beta transition and below alpha transition).....	107
4-14. Strain localization in shear bands formed in PMMA at 80 °C. Rate sensitivity is decreased above the beta transition temperature.....	108
4-15. Shear bands formed in PMMA at 80° C. ....	108
4-16. Dynamic mechanical analysis of PMMA- <i>co</i> -EA at 1 and 10 Hz.....	110
4-17. Strain localization in shear bands formed in PC at -190° C. Rate sensitivity is increased below $\beta$ transition temperature. ....	111
4-18. Shear bands formed in PC at -190° C. ....	111
4-19. A significant contribution to the $\beta$ relaxation in PMMA is a 180° flip of the pendant group. The flip is coupled to main chain mobility.....	113
4-20. A significant contribution to the $\beta$ relaxation in PC is a 180° flip of phenyl rings in the main chain.....	114
4-21. Predicted strain localization of physically aged PMMA. ....	117
4-22. Strain localization in physically aged PMMA. Localization is higher at lower strain rates. Rate sensitivity is decreased until the highest rate. ....	117
4-23. Predicted strain localization in aged PC.....	118

4-24. Strain localization in physically aged PC. Localization is higher at lower strain rates. Rate sensitivity is decreased.....	118
4-25. Loss modulus from DMA on PMMA both as received and after physical aging. Aging results in narrowing of the alpha transition. ....	119
4-26. Loss modulus from DMA on PC both as received and after physical aging. Aging results in narrowing of the alpha transition.....	119

## CHAPTER 1

### 1. IMPACT RESISTANT GLASSY POLYMERS USING COMPRESSIVE PRE-STRESS

#### Abstract

The application of an externally applied pre-stress on impact properties is studied on polymethyl methacrylate (PMMA) organic glass. Samples are tested under equi-biaxial compression, simple shear and a combination of biaxial compression and shear. Equi-biaxial compression is shown to increase the threshold stress level for projectile penetration whereas shear pre-stress has a large effect on the overall energy absorbed during an impact. There is also an apparent interaction observed between compression and shear to dramatically increase the threshold stress. Pre-stressed laminates show an increase in damage area because of the unique formation of a secondary cone.

#### Introduction

The development of transparent materials that are more impact and ballistic resistant have many possible applications ranging from military vehicle windows to civilian products such as hurricane resistant windows. Two common organic glasses that are used in these applications include polycarbonate (PC) and polymethyl methacrylate

(PMMA). These materials are transparent and are more lightweight when compared with their inorganic counterparts, which is important especially in vehicle and personal protection applications. Each of these materials has a unique mechanism by which energy is absorbed during impact. PC, like other ductile materials, has the ability to absorb large amounts of energy through plastic deformation that accompanies the yielding process. In the case of PMMA, the majority of energy absorption is due to the creation of surface area during fracture. Additionally, there is a stark difference between the macroscopic failure mechanisms of these two materials. Failure in PC is relatively localized while PMMA is effective at delocalizing failure in the form of radial cracking and Hertzian cone fracture (during impact).

The effect of loading rate is also an area where these two materials differ. At low velocity impact rates, PC outperforms PMMA while at ballistic rates the  $V_{50}$  (velocity at which the probability of complete penetration is 0.5) of PMMA can exceed that of PC.<sup>1,2</sup>

The continual goal in materials science is the improvement of the performance of materials to meet applications. In the case of brittle materials, one way to improve their working range is through the application of compressive pre-stress. The idea of using a compressive

pre-stress to enhance the properties of non-polymeric brittle materials has been used with success for quite some time.<sup>3</sup> The use of concrete in structures is made more feasible by the application of a compressive pre-stress through either pre or post-tensioned tendons. In concrete, the tensile strength is very low when compared with its compressive strength. Consequently, a superposed compressive stress can greatly increase the working stress range of the material. Inorganic glasses have also been shown to display improved strength when tempered because of an induced layer of compression on each surface of the glass.<sup>4</sup> The ballistic response of ceramic targets pre-stressed by confinement on all surfaces by titanium or steel was modeled by Holmquist and Johnson.<sup>5</sup> In the case of complete penetration, pre-stress was shown to decrease the exit velocity of the projectile. When only partial penetration was obtained, the extent of penetration was decreased by pre-stress. Similar experimental work by Bao et al. looked into the effects of pre-stress and confinement on ceramic targets.<sup>6</sup> Multi-axial compressive pre-stress was applied to heated alumina tiles by the shrinkage of an aluminum alloy cast around the tile. Critical failure loads were determined by contact of a steel ball on a free surface of alumina under biaxial pre-stress. A 15-fold increase was observed for both the critical load at quasi-static rates as well as the critical impact energy at low velocity rates.

Work has also been done to investigate the effect of pre-stress on polymeric materials. Motahhari and Cameron used an approach similar to pre-stressed concrete by applying a pre-tension to glass fibers during cure to place an epoxy matrix under uniaxial compression.<sup>7,7</sup> They found a 33% increase in impact energy absorbed during Charpy tests. The improvement was explained by residual shear stresses weakening the fiber matrix interface promoting failure in the longitudinal direction. However, the increase in impact properties showed an apparent upper limit because of the weakening of the fibers by residual tensile stresses. Fancey also studied fiber reinforced polymeric composites. Here, the pre-stress was applied to a thermosetting polyester matrix by imbedding pre-tensioned nylon 6,6 fibers before cure. In contrast to the work by Motahhari and Cameron, Fancey used the viscoelastic recovery of fibers to apply the pre-stress.<sup>8-13</sup> The rationale behind this approach was to address some of the challenges with the fabrication of non-planar geometries. Fancey observed a similar improvement of 25% in impact energy with Charpy tests.

One approach to the fabrication of armors relies on the synergistic relationship between brittle and ductile layers. A clear example of the effectiveness of this approach is in composites of PC and PMMA. Hsieh and Song studied composites of alternating layers of PC and PMMA where

the thickness of each component was on the micron length scale.<sup>14,15</sup> It was determined that the critical parameter in the ballistic response of these composites was the thickness of the PMMA. The brittle layer thickness determined the amount of damaged area. When failure is delocalized by PMMA it allows a larger volume of the backing PC layer to participate in yielding and hence increase the performance. Hsieh and Song illustrated this effect nicely by comparing laminates with mm scale thickness of equivalent corresponding ply thicknesses of PC/PC/PC to PC/PMMA/PC. The laminate that incorporated the brittle inter-layer showed a 37% increase in  $V_{50}$ .<sup>2</sup>

In this chapter, we will look at some interesting changes in failure mechanism that occur when the PMMA layer of these laminates is subjected to a compressive pre-stress. In contrast to the aforementioned methods of pre-stress, this work uses methods of pre-stress that maintain transparency of the target. To the author's knowledge, all the work on polymers has focused on uniaxial pre-stress with beam geometries. This chapter focuses on the effects of biaxial pre-stress. Both equi-biaxial and more complicated stress states are investigated. The damage initiation, mechanisms, and sequence are reported for both conventional and pre-stressed laminates as well as for monolithic plates.

## Experimental

### Materials

The principal material under investigation was Acrylite PMMA obtained from McMaster-Carr. The material was supplied in two forms: rectangular sheets and circular samples with a nominal diameter of 102 mm. When circular samples of additional diameters were needed, they were machined from the rectangular sheets using an indexing table. The nominal thickness of both forms was 6 mm. The as-received PMMA showed no noticeable birefringence suggesting that residual stresses due to processing are negligible. The elastic properties of the PMMA were measured according to ASTM D638. Young's modulus,  $E$ , was 3.29 GPa and Poisson's ratio,  $\mu$ , was 0.33. PC sheets with a thickness of 3 mm from McMaster-Carr were also used in the fabrication of laminates. Methylene Chloride was obtained from Sigma-Aldrich and used without purification. Polyurethane adhesive was likewise purchased from McMaster-Carr.

### Application of Pre-Stress

Two methods of pre-stress application were used. One was a square frame made of one-inch steel bar stock (Figure 1-1). In the square frame, bolts at each corner are tightened to apply compressive stress in the glass. Depending on the initial sample geometry, this frame allows for

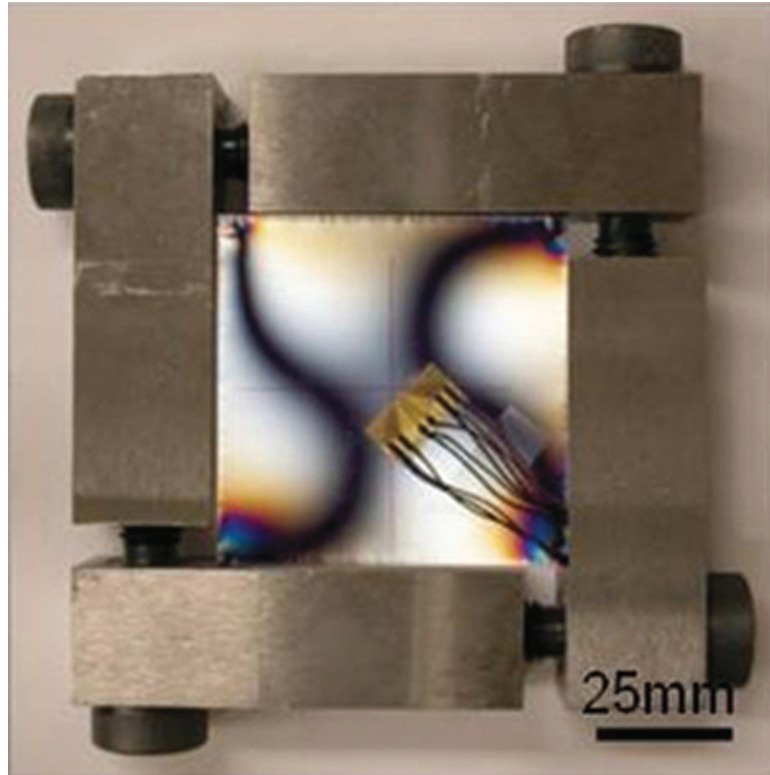


Figure 1-1. Square frame with overlaid image of pre-stressed sample viewed under crossed polars. Scale bar = 25 mm.

application of shear, biaxial compression, or a combination of the two. In the case of biaxial compression, samples were machined as 63.5 x 63.5 mm squares. In an attempt to obtain a state of equi-biaxial compression at the center, the sample was viewed between crossed polars during loading. If extinction is achieved at a point in a specimen under load regardless of rotation, then every direction in the plane at that point is a principal direction and the stress is equi-biaxial.<sup>17</sup> The level of pre-stress was measured by a foil strain rosette mounted on the surface of the sample in the center. The surface of the sample was cleaned with

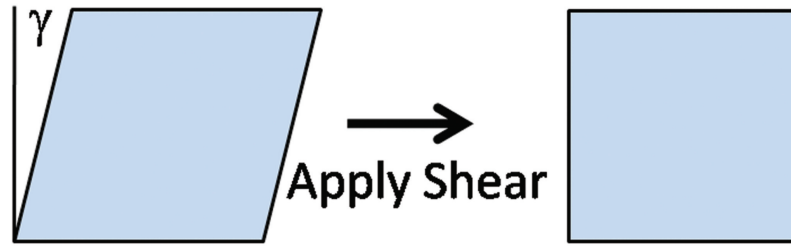


Figure 1-2. Schematic of simple shear pre-stress method.

isopropyl alcohol to ensure good adhesion. The strain gauge was adhered using a few drops of cyanoacrylate adhesive. Data was acquired from the strain rosette using LabView software.

In the case of simple shear, samples were machined to a rhombus and deformed in the frame to a square. The angle machined into the samples was used to estimate the level of shear pre-stress (Figure 1-2).

The other method of pre-stress used a shrink fit technique. A carbon steel pipe was cut into a 12 mm thick ring and the inner diameter was bored out so that it was smaller than the 102 mm diameter of a disk of PMMA at room temperature [Figure 1-3(a)]. The radial mismatch between the inner radius of the steel ring and the PMMA disk ranged from 0.26 to 0.42 mm. The PMMA was cooled down in liquid nitrogen shrinking the disk to a diameter smaller than the steel ring. The shrunken disk was fit inside of the steel ring and upon warming to room temperature a seal pressure developed on the sample. This type of

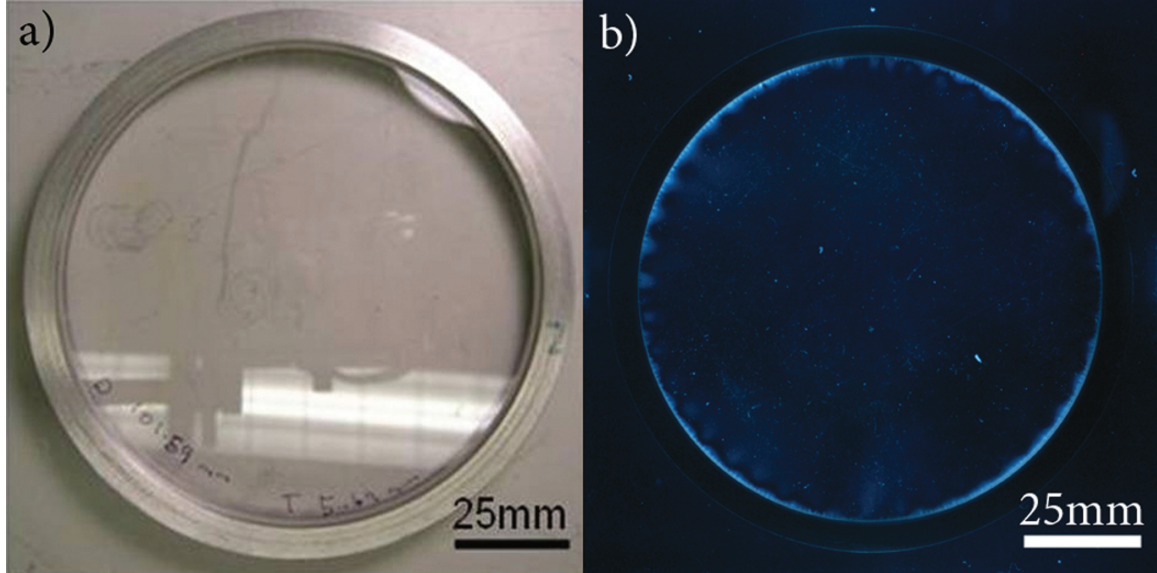


Figure 1-3. (a) Shrink fit sample. (b) Shrink fit sample viewed between crossed polars. Scale bars = 25 mm.

loading condition produces an equi-biaxial stress state throughout the specimen. The image of a shrink fit sample viewed between crossed polars in Figure 1-3(b) shows extinction throughout the sample regardless of rotation because every direction is a principal direction. The level of pre-stress can be determined by considering the radial displacements of the two components according to Equation 1-1, which is derived from Lamé's classical solution.<sup>18</sup>

$$\text{Eq 1-1)} \quad \sigma_{rr} = \sigma_{\theta\theta} = \delta \left[ \frac{a}{E_m} \left( \frac{a^2 + b^2}{b^2 - a^2} + \nu_m \right) + \frac{a}{E_p} (1 - \nu_p) \right]^{-1}$$

The radial mismatch,  $\delta$ , is the difference between the radius of the PMMA disk and the inner radius of the metal ring at room temperature

before assembly. The parameters  $a$  and  $b$  are the radii of the PMMA after assembly and the outer radius of the ring after assembly, respectively (Figure 1-4).  $E$  and  $\nu$  are the modulus and Poisson's ratio and the subscripts  $p$  and  $m$  refer to the polymer and metal ring, respectively. The modulus of the steel was measured to be 200 GPa by a ring compression test, whereas the value of 0.29 for Poisson's ratio was estimated from the average value of 1,955 grades of carbon steel.<sup>19,20</sup> In all cases, pre-stress was applied at 23° C before testing.

Transparent composite laminates with a PC/PMMA/PC architecture were fabricated by either solvent welding with methylene chloride or by a commercial polyurethane adhesive. Each surface of each ply was cleaned with isopropyl alcohol. In the case of solvent welding, the PC ply was partially submerged in a shallow dish of methylene chloride for 10 s then pressed onto the PMMA ply. Pressure was then applied by a toggle clamp

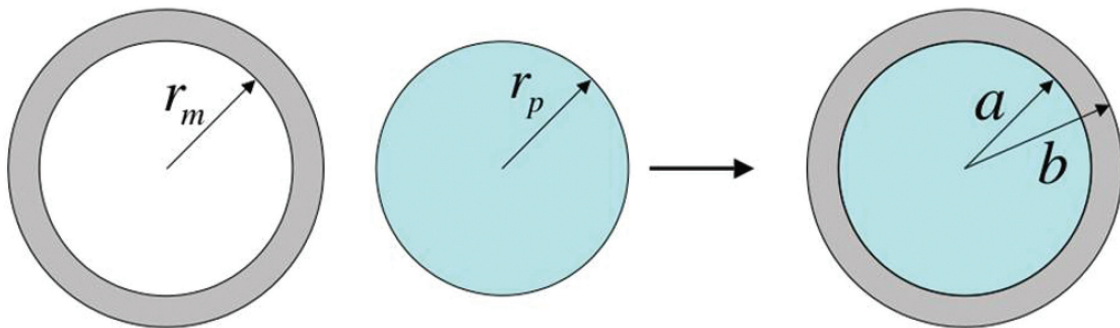


Figure 1-4. Dimensions used in shrink fit calculations.

for 3 min and the solvent was allowed to evaporate overnight. The polyurethane used was a two part adhesive that was mixed with a static mixer. The adhesive was applied to one ply and the other ply was pressed by hand to yield an interlayer thickness on the order of 0.25 mm. The method of pre-stress used on the laminates was exclusively shrink fit. The incorporation of PC plies necessitates higher velocities to achieve failure in the laminates. The impact velocity was chosen so that it was high enough to create damage in the laminate but low enough that the tup base did not impact the sample. At these velocities, the tup does not fully penetrate the sample i.e. all the kinetic energy is absorbed in each test.

Low-velocity impact testing was conducted on a Dynatup 8250 with a 6 mm diameter tup and a hammer mass of 3.256 kg. The capacity of the load cell was 44 kN. Impact velocities ranged from 3 to 6 m/s. The 3-4 m/s range was achieved in gravity mode whereas the 4-6 m/s range required pneumatic assist. The sample was secured during testing via a pneumatic clamp with a force of 1.64 kN. To insure consistent boundary conditions for different methods of pre-stress, steel shaft collars with an inner diameter of 42 mm were placed on each surface of the sample to directly transfer the load of the clamp to the sample. High-speed images

were captured during impact tests by a Kodak Ektapro HS Motion Analyzer model 4540 with frame rates up to 40,500 fps.

Impact tests at ballistic rates were performed at the Army Research Laboratories in Natick, MA. The apparatus used was a helium gas gun firing a 17-grain projectile. The experiments referred to here were performed at ~130 m/s (near the  $V_{50}$  of 6 mm PMMA).

Average roughness,  $R_a$ , was measured using a Veeco Dektak 150 profilometer with a 12.5  $\mu\text{m}$  radius stylus. The value  $R_a$  is defined for a line scan of length  $L$  in the  $x$  direction as the average deviation in the  $y$  direction from the mean line defined by  $y = 0$ .

Eq 1-2) 
$$R_a = \frac{1}{L} \int_0^L |y| dx$$

For each area under investigation, three 500  $\mu\text{m}$  scans were made under a 98  $\mu\text{N}$  force at a rate of 16.6  $\mu\text{m/s}$ . Measurements were made on the radial crack surface of shear pre-stressed samples in the center of the thickness and as near the point of impact as possible.

## Results and Discussion

### Low-Velocity Failure Mechanism

Although investigating the response of monolithic plates under low-velocity impact rates, one of the first observations made on the effect of pre-stress was an apparent change in failure mechanism (Figure 1-5). Samples without pre-stress display radial cracking that extends beyond the boundary of the clamps as well as cone fracture. When a compressive pre-stress is applied, the only clearly visible mechanism is cone fracture. High-speed photography was used during impact to observe the development of each mechanism. From the images, it was determined that radial cracks were indeed formed in pre-stressed samples but the growth of the cracks was stunted so that the radius of the cone exceeded the length of the radial cracks (Figure 1-6). In a general sense, this initial

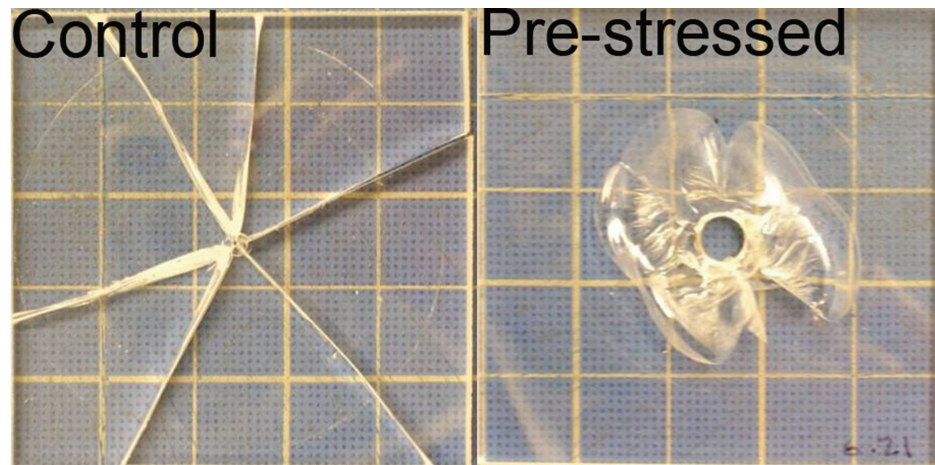


Figure 1-5. Low velocity ( $\sim 2$  m/s) failure mechanism. In the control sample, the dominant mechanism is radial cracks. Under pre-stress, cone fracture is most visible. Underlying grid unit = 12.7 mm.

observation appears to be negating one of the most beneficial aspects of failure in PMMA. Namely, the amount of delocalization of damage area apparently decreases with the application of pre-stress. However, this apparent disadvantageous failure mechanism will take a different advantageous form as will be discussed in the section on transparent laminate composites.

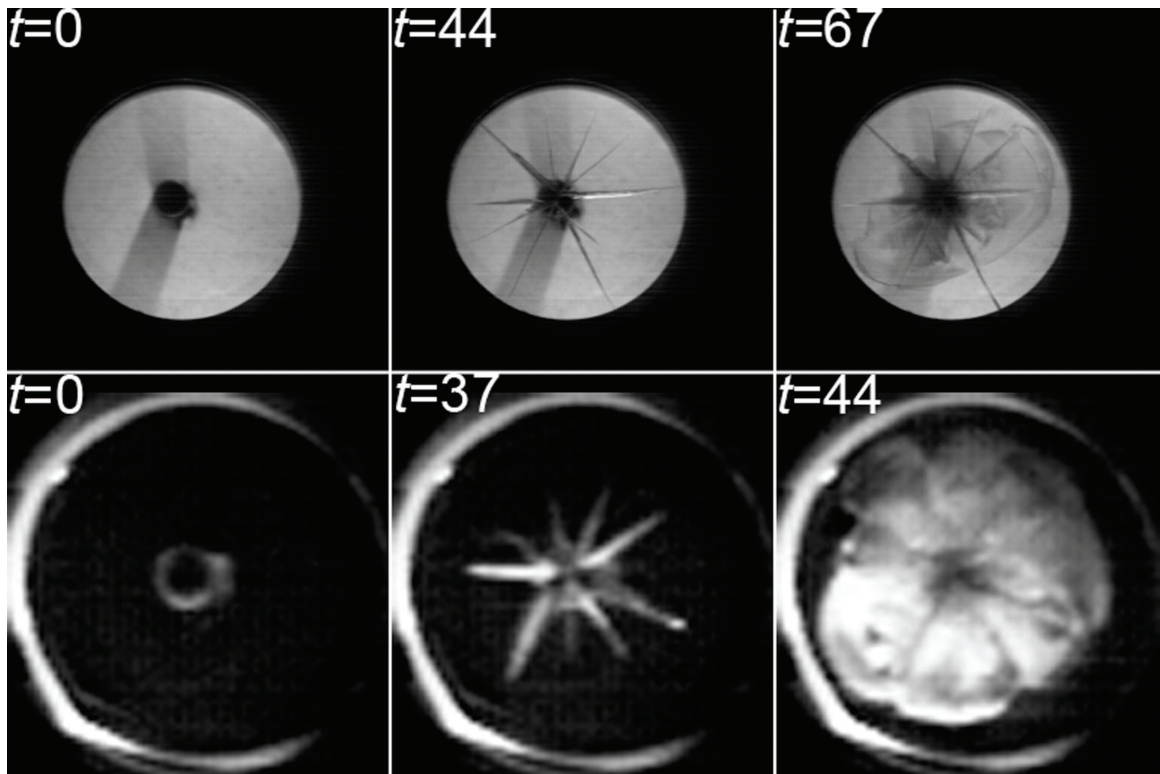


Figure 1-6. Low velocity mechanism change. Top row (frame rate = 4500 fps) - control sample exhibits large radial cracks as well as cone fracture. Bottom row (frame rate = 40,500 fps) - pre-stressed sample shows stunted radial crack growth. Unit of time = ms. Diameter of circular boundary in all images = 42 mm.

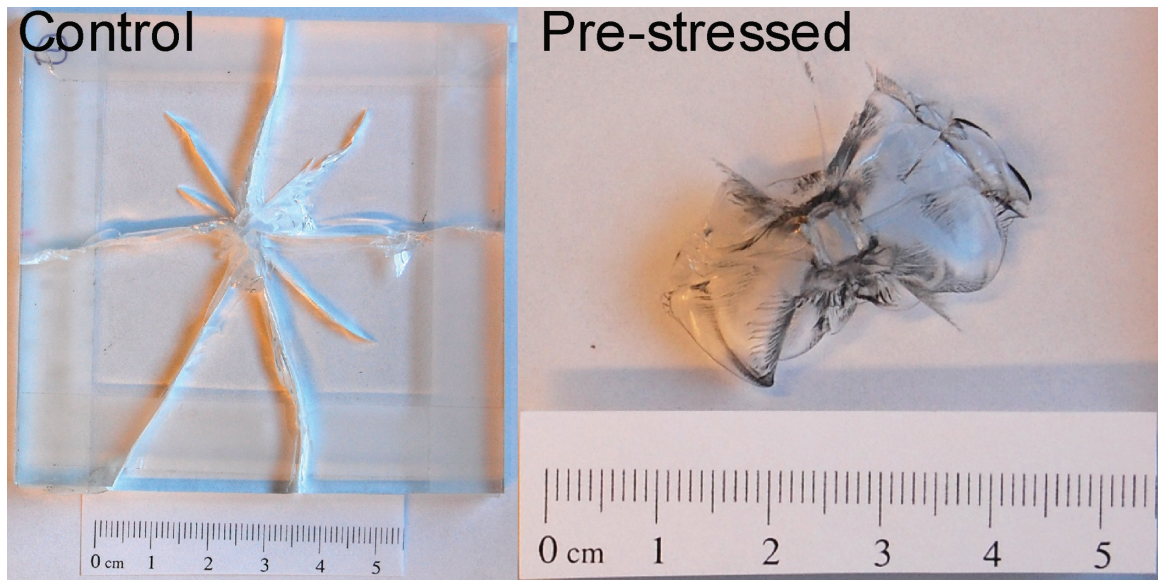


Figure 1-7. Ballistic impact ( $\approx 130$  m/s) on monolithic plates. Significant reduction of radial cracking seen with pre-stress.

### High-Velocity Failure Mechanism

Some preliminary results from ballistic tests on pre-stressed monolithic plates of PMMA suggest there are at least some similarities between the effects of pre-stress at low and high velocities. The failure mechanism of the control sample is largely dominated by radial cracking with a small vestige of Hertzian cone fracture (Figure 1-7). The opposite is observed in the pre-stressed sample. Damage is localized with a prominent Hertzian cone while radial cracking is suppressed. Further work is needed to establish whether or not other trends (such as an increase in threshold) observed at low velocities are also seen at ballistic rates.

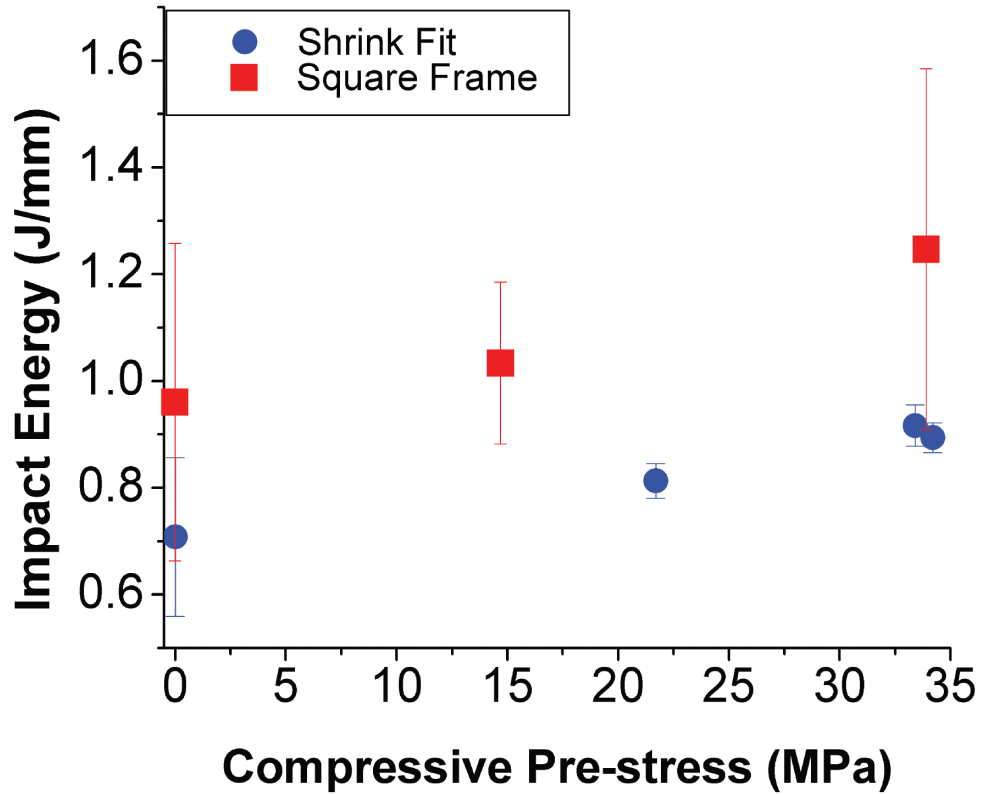


Figure 1-8. Effect of pre-stress on impact energy.

### Impact Energy

When looking at the total impact energy of pre-stressed PMMA, the improvements are modest. The average value of impact energy for the shrink fit method increases from 0.71 J/mm to 0.92 J/mm whereas the square frame method shows increases from 0.96 J/mm to 1.25 J/mm, an ~ 30% increase in impact energy for both pre-stress methods (Figure 1-8). This increase in impact energy is somewhat surprising given the initial observation that pre-stress seems to localize damage resulting in less



Figure 1-9. Radial crack surface area for energy estimates. Sample thickness = 5.75 mm.

created surface area. This observation coupled with the fact that brittle materials absorb energy by surface area creation would lead one to expect a decrease in impact energy with a decrease in created surface area. To investigate this apparent discrepancy, the high-speed images were compared with the load-deflection curves to get estimates on the amount of energy required to create the separate features.

Estimates of the surface area created during cone fracture were made by analyzing images of fractured samples. For the radial crack surface area on control samples, a penetrant dye was used to mark the initial surface area then the sample was fractured in liquid nitrogen to separate each piece (Figure 1-9). For pre-stressed samples, although cone fracture removes most of the evidence of radial cracks, the ends of the cracks are still visible and can be located by analyzing the high-speed images. Since direct measurements were not possible, the shape was

assumed to be triangular, which is likely an overestimate of the surface area. By assuming that radial cracking initiates at the point of nonlinearity in the load-deflection curve, the high-speed images were synchronized with the load-deflection data to determine at which point the different mechanisms began and ended. The energy was calculated by integrating the load-deflection curve over the limits defined in Equations 4 and 5, and in Figure 1-10 and subtracting off the area under the theoretical unloading curve. The unloading curve travels linearly to the

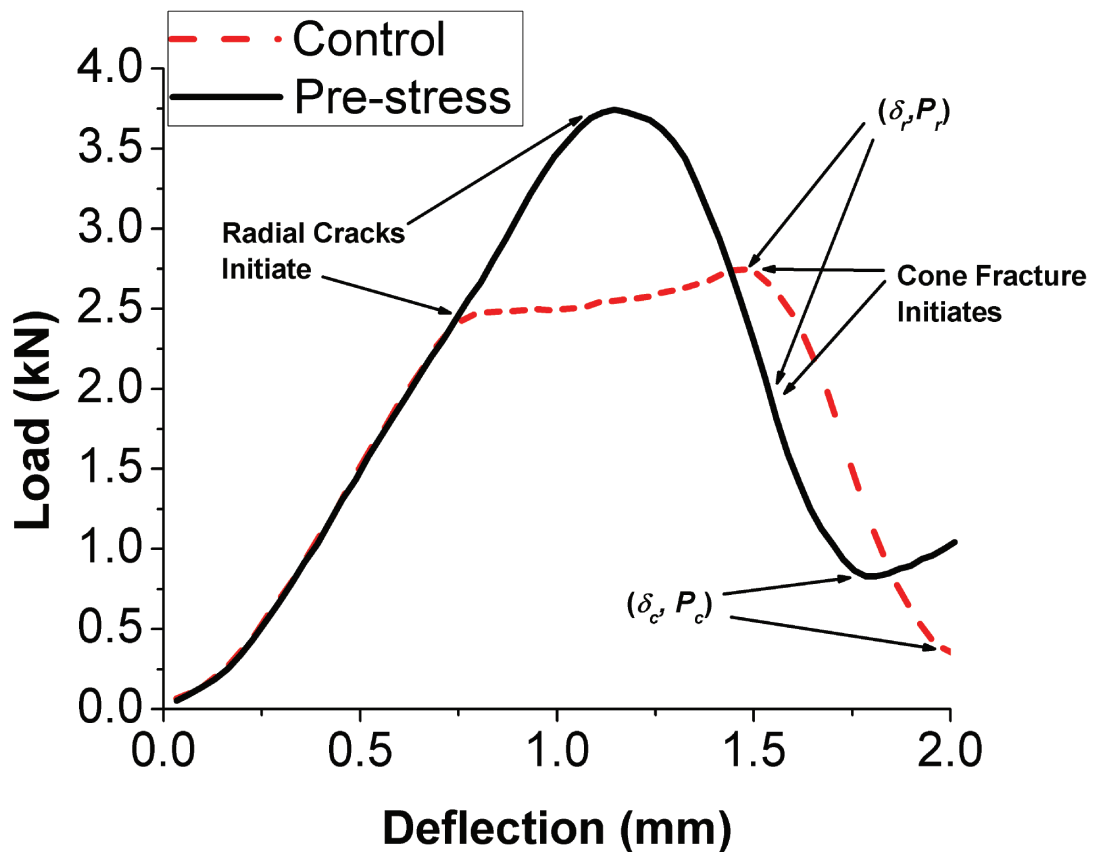


Figure 1-10. Comparative load-deflection curve. Failure mechanism initiation observed by high speed photography.

origin based on the assumption that plastic deformation during fracture

$$\text{Eq 1-3)} \quad E_r = \int_0^{\delta_r} P(\delta) d\delta - \frac{1}{2} \delta_r P_r$$

is negligible for brittle materials such as PMMA.

$$\text{Eq 1-4)} \quad E_c = \int_0^{\delta_c} P(\delta) d\delta - \frac{1}{2} \delta_c P_c - E_r$$

where,

$E_r$  = Energy absorbed by radial fracture mechanism

$P(\delta)$  = Load as a function of displacement

$\delta_r$  = Final deflection for radial fracture mechanism

$P_r$  = Final load for radial fracture mechanism

$E_c$  = Energy absorbed by cone fracture mechanism

$\delta_c$  = Final deflection for cone fracture mechanism

$P_c$  = Final load for cone fracture mechanism

In the control samples, fracture energies were estimated to be  $0.6 \pm 0.1$  kJ/m<sup>2</sup> and  $1.1 \pm 0.3$  kJ/m<sup>2</sup> to create radial cracks and cone surfaces, respectively. With a pre-stress of  $\sim 33$  MPa, the energy to create radial cracks increases dramatically to  $2.8 \pm 0.6$  kJ/m<sup>2</sup> whereas the energy for cone fracture remained relatively unchanged at  $0.9 \pm 0.1$  kJ/m<sup>2</sup>. This

significant increase in the energy for radial cracks can be explained by considering two observations. One, which has already been mentioned, is that pre-stress stunts radial crack growth resulting in less surface area. The other is that the peak or threshold load reached in pre-stressed specimens is significantly higher than the control, which leads to an increase in energy (Figure 1-10). The combination of more energy and less surface area explains this drastic increase. The modest increases in total impact energy are a consequence of normalizing the energy by sample thickness rather than created surface area.

It is interesting to note the relative scatter in the impact energy data (Figure 1-8). The lowest amount of scatter occurs in shrink fit samples. Both the control samples and the square frame pre-stressed samples have greater variation in absorbed energy. It appears that an added benefit of a uniform state of pre-stress is greater reproducibility, which is beneficial from an applications design standpoint.

The comparison of the load-deflection curves in Figure 1-10 illustrates an important consequence of an externally applied pre-stress. In the control sample, following initiation of radial cracking, the load gradually increases with increasing deflection until cone fracture initiates and the load drops. In the pre-stressed sample, the load drops

dramatically upon radial crack initiation. The pre-stressing process stores strain energy in the PMMA. As the plate begins to deflect during impact, the strain energy can be released by impact promoted buckling, which is evidenced by the drop in load. It is important to note that this trend is attributed to the specific method of pre-stress application. If the pre-stress were applied by a laminated architecture, the laminate would be self-stabilizing. Any buckling of a compressively pre-stressed ply would come at the penalty of adding strain energy to the tensile pre-stressed ply.

### Threshold

One of the beneficial effects of pre-stress shown in Figure 1-10 is the increase in the failure threshold. This effect was quantified in two ways. In the first method, the threshold was determined by sequentially increasing the drop height until complete penetration occurred. Without pre-stress, a drop-height of 195 mm (4.9 J) resulted in penetration. With the application of 31 MPa in the square frame the threshold was increased to 396 mm (9.9 J). The second method involved a single specimen approach. The threshold load was defined as the highest load before irreversible damage as indicated by the departure from linearity in the load-deflection curves. This load was, in turn, used to define the threshold stress;

Eq 1-5) 
$$\sigma_t = \frac{P}{h^2}(1 + \nu) \left[ 0.485 \ln \frac{a}{h} + 0.52 \right]$$

where,  $P$  is the threshold load,  $h$  is the thickness,  $\nu$  is Poisson's ratio and  $a$  is the clamped radius.<sup>21</sup> The threshold stress is the maximum tensile stress, from bending, on the surface opposite impact. As is seen in Figure 1-11, the threshold stress increases with pre-stress. In the case of the shrink fit samples, the increase in threshold stress is approximately equal to the pre-stress on the sample. This is an expected result, if the

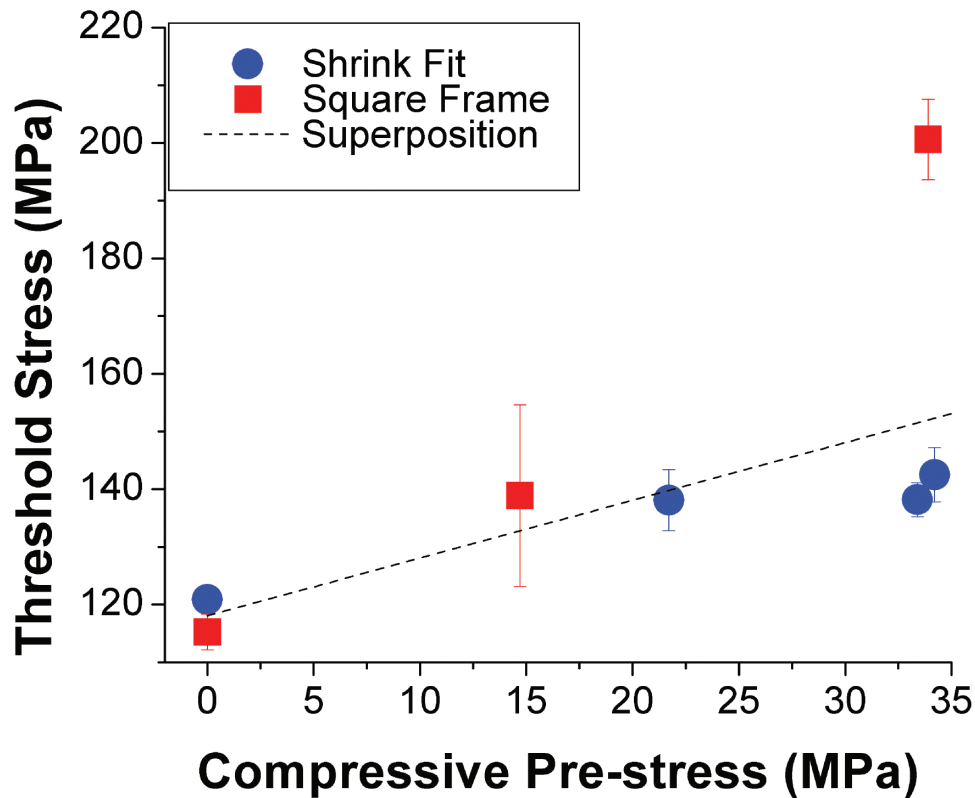


Figure 1-11. Effect of pre-stress on threshold.

increase in threshold is from simple superposition of the pre-stress. However, samples pre-stressed in the square frame deviate significantly from this trend in that they show a dramatic increase in the threshold stress. This observed difference is significant and is the impetus of the content in Chapter 3. The main difference of the two methods of pre-stress lies in the state of stress in the sample. In the case of shrink fitting, the sample is in equi-biaxial compression throughout the plane. The square frame induces some level of shear stress in addition to the biaxial compression as evidenced by the presence of isochromatic fringes seen between crossed polars (Figure 1-1). One possible explanation of this behavior is some level of mode mixity induced by the pre-stress. The Mode II fracture response of glassy polymers will be discussed in detail in Chapter 3.

#### Effect of shear

Samples under simple shear pre-stress exhibit a fracture pattern indicative of the state of stress in the sample. The dominate feature is one large radial crack aligned normal to the principal tensile stress direction. The cone fracture has an elliptical projection with its major axis parallel to the radial crack. Fractography of the radial crack surface reveals circular features near the point of impact that turn into parabolic markings at points further from the center (Figure 1-12). These patterns

give witness to the formation of secondary cracks ahead of the primary crack front and are indicative of a high level of stress at the crack tip.<sup>22,23</sup> These surface features have a rough appearance, which was quantified by profilometry (Figure 1-13). Not only are there finer surface features being created, but the initiation of these secondary cracks will occur at local heterogeneities and is not necessarily confined to a single plane. As the primary crack front proceeds, it will change direction to meet the secondary cracks. This change in direction along with the increase in surface area suggests an increase in energy absorbed during failure, which is indeed observed in Figure 1-14. For a sample under simple shear pre-stress, the first principal stress adds to the tensile stress due to bending of the plate during impact resulting in a decrease in the threshold stress. It is clear from these results that simple shear alone cannot account for the increase in threshold seen for samples pre-stressed in the square frame.

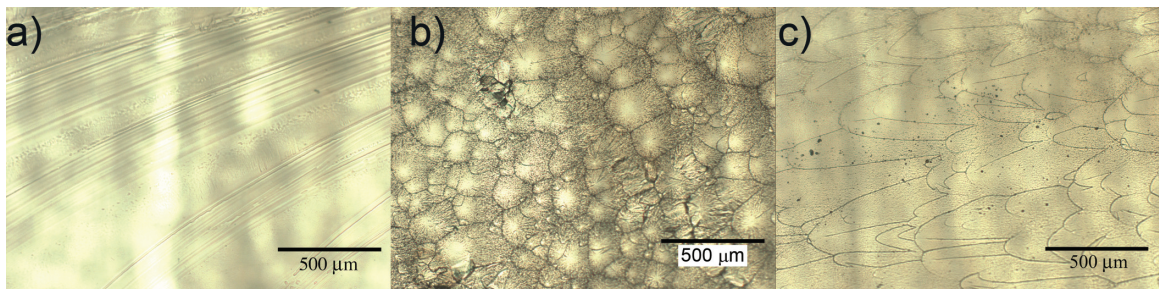


Figure 1-12. Fractography of radial crack surface for (a) shrink fit sample, (b) shear pre-stressed sample near impact, and (c) shear pre-stressed sample away from impact. All scale bars = 500  $\mu\text{m}$ .

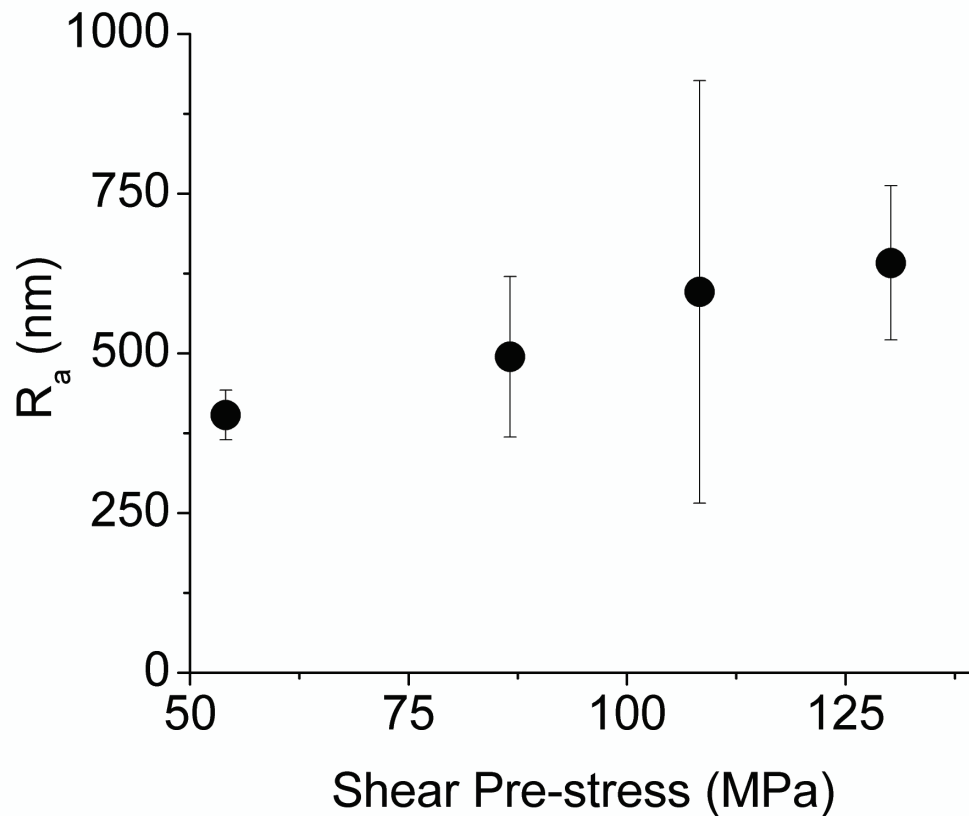


Figure 1-13. Surface roughness of radial cracks on shear pre-stressed samples.

#### Pre-stressed transparent composite laminates

As mentioned above, the laminates were tested at velocities that resulted in arrest of the tup regardless of sample composition and pre-stress level. However, interesting effects of pre-stress can be seen by observing the resultant fracture patterns. The two different methods of adhering the plies give interfaces with different strengths, and the strength of this interface plays an important role in the performance of the laminate. When solvent welding is used the interface is relatively strong compared to the strength of the interface formed with the

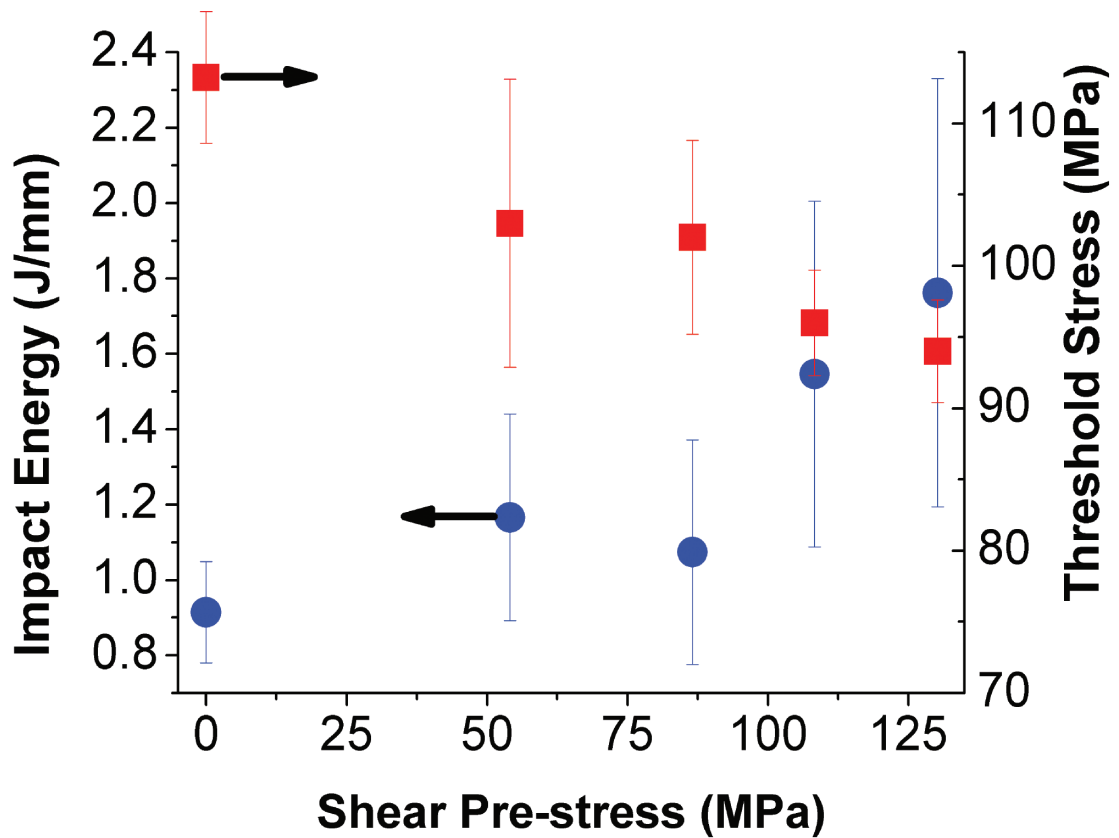


Figure 1-14. Effect of shear pre-stress on impact energy and threshold.

polyurethane adhesive. A most interesting result is observed in pre-stressed solvent welded laminates. In addition to radial cracking and cone fracture, a large secondary cone is formed in the PMMA ply (Figure 1-15).

The secondary cone initiates at the impacted surface and grows radially toward the distal surface of the ply at a shallow angle. All of the damage created by the secondary cone is confined to the PMMA ply. As seen in Figure 1-15, the radius of the secondary cone slightly exceeds the

21 mm radius of the clamp. Work done by Hseih and Song has shown that when impact velocities are increased to ballistic rates and thicker samples are tested, the  $V_{50}$  of PMMA exceeds that of PC.<sup>2</sup> If damage in the PMMA ply absorbs more energy than the PC ply then the formation of a large secondary cone would drastically improve performance at ballistic rates. This secondary cone is not observed in control samples (Figure 1-16).

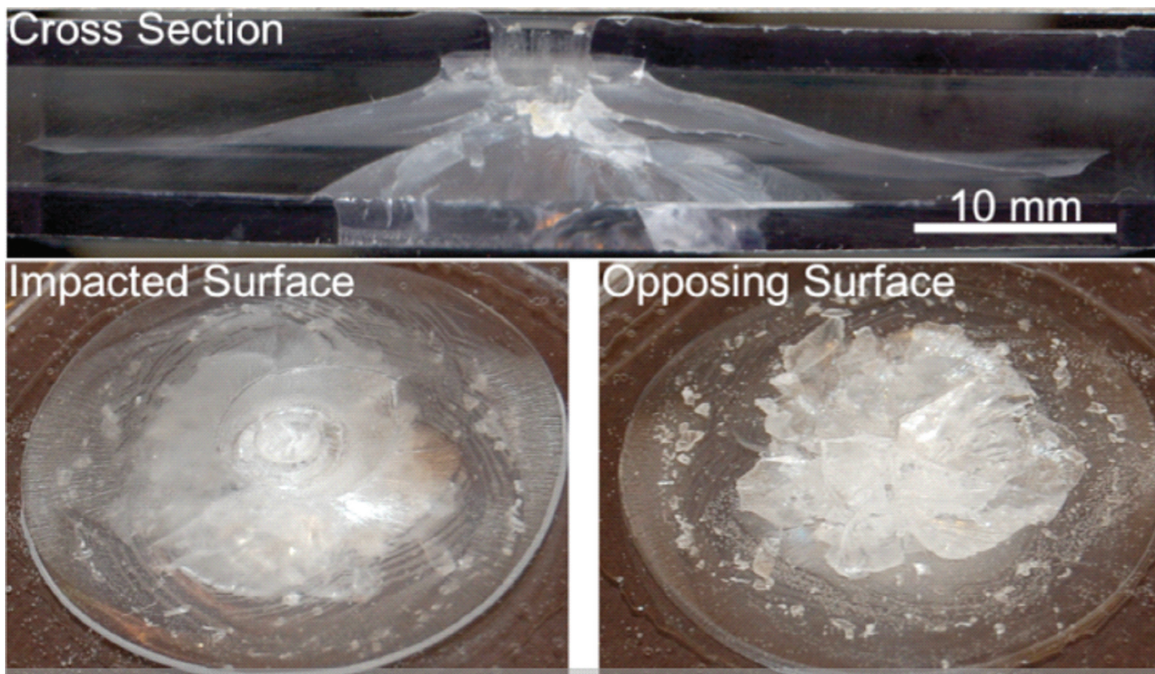


Figure 1-15. Top image cross section of PC/PMMA/PC laminate using solvent welding on both plies showing secondary cone and brittle fracture of PC distal ply. Bottom images PC/PMMA/PC laminate using solvent welding on impacted ply and polyurethane on opposing ply shows secondary cone as well as containment of PMMA spall. Cone diameter ~50 mm.

A negative effect of a strong interface can also be seen in Figure 1-15. Sharp radial cracks are initiated in the PMMA ply, and because of the high strength of the interface, the cracks are able to propagate through the back ply of PC. This is disadvantageous for two reasons. The cracks form in the PC without significant yielding, which should decrease the amount of energy absorbed. Also, the cracked portions peel open allowing PMMA spall to pass. This latter issue would be especially important in transparent armor applications where containment of spall is necessary to protect personnel. When the polyurethane adhesive is used between plies, the failure process changes significantly from that observed in the solvent welded laminates. The secondary cone seen in pre-stressed solvent welded laminates does not occur when the top ply is adhered to the PMMA by polyurethane. With the weaker interface at the back ply, sharp cracks from the PMMA ply do not propagate into the PC. The failed interface maintains the continuity of the PC ply containing spall.



Figure 1-16. Control laminate - no secondary cone formation.

## Conclusions

Pre-stressing PMMA affects several aspects of the impact response of the material. A decrease in damage area is seen at both low velocity and ballistic rates for monolithic plates. Radial crack growth is suppressed leading to higher apparent fracture energies. Total impact energy is increased by ~30% for both methods of pre-stress. The threshold stress is increased by an amount consistent with superposition for equi-biaxially pre-stressed samples. When the glass is subjected to a complicated state of pre-stress involving both shear and biaxial compression, the increase in threshold stress is substantially greater. The application of simple shear pre-stress leads to the formation of secondary cracks ahead of the primary crack front and a subsequent increase in the total impact energy. With the laminates tested, pre-stress interestingly led to the formation of a secondary cone in the brittle PMMA layer with a radius that exceeded the clamped boundary.

## References

1. Lewis, G. & Mladi, S. Correlation between impact strength and fracture toughness of PMMA-based bone cements. *Biomaterials* **21**, 775-781 (2000).
2. Hsieh, A. J., DeSchepper, D., Moy, P., Dehmer, P. G. & Song, J. W. The Effects of PMMA on Ballistic Impact Performance of Hybrid Hard/Ductile All-Plastic- and Glass-Plastic-Based Composites. *Army Research Laboratories* (2004).
3. Freyssinet, E. & Seailles, J. US Patent #2080074, Piece of reinforced concrete. (1937).
4. Minor, J. Focus on Glass. *APT bulletin* **32**, 47-50 (2001).
5. T J Holmquist G R Johnson Modeling projectile impact onto prestressed ceramic targets. *J. Phys. IV France* **110**, 597-602 (2003).
6. Bao, Y. Prestressed ceramics and improvement of impact resistance. *Materials Letters* **57**, 518-524 (2002).
7. Motahhari, S. & Cameron, J. Fibre Prestressed Composites: Improvement of Flexural Properties through Fibre Prestressing. *Journal of Reinforced Plastics and Composites* **18**, 279-288 (1999).
8. FANCEY, K. S. Prestressed Polymeric Composites Produced by Viscoelastically Strained Nylon 6,6 Fibre Reinforcement. *Journal of Reinforced Plastics and Composites* **19**, 1251-1266 (2000).

9. Pang, J. W. C. & FANCEY, K. S. Analysis of the tensile behaviour of viscoelastically prestressed polymeric matrix composites. *Composites Science and Technology* **68**, 1903-1910 (2008).
10. FANCEY, K. S. Investigation into the feasibility of viscoelastically generated pre-stress in polymeric matrix composites. *Materials Science and Engineering: A* **279**, 36-41 (2000).
11. FANCEY, K. S. Fiber-reinforced polymeric composites with viscoelastically induced prestress. *Journal of advanced materials* **37**, 21-29 (2005).
12. Pang, J. W. C. & FANCEY, K. S. An investigation into the long-term viscoelastic recovery of Nylon 6,6 fibres through accelerated ageing. *Materials Science and Engineering: A* **431**, 100-105 (2006).
13. FANCEY, K. S. Viscoelastically prestressed polymeric matrix composites - Potential for useful life and impact protection. *Composites Part B: Engineering* **41**, 454-461 (2010).
14. Hsieh, A. J. & Song, J. W. Measurements of Ballistic Impact Response of Novel Coextruded PC/PMMA Multilayered-Composites. *Journal of Reinforced Plastics and Composites* **20**, 239-254 (2001).
15. Hsieh, A. J. High strain-rate behavior of coextruded polycarbonate/PMMA composites. *Shock compression of condensed matter* **505**, 555-558
16. Archer, J. S. & Lesser, A. J. Impact resistant polymeric glasses using compressive pre-stress. *J. Appl. Polym. Sci.* **114**, 3704-3715 (2009).

17. Dally, J. W. & Riley, W. F. *Experimental Stress Analysis*. (McGraw-Hill: New York, 1991).
18. Saada, A. S. *Elasticity: Theory and Applications*. (Krieger: Malabar, Florida, 1993).
19. Frisch-Fay, R. *Flexible Bars*. (Butterworths: Washington DC, 1962).
20. *MatWeb* at <<http://www.matweb.com>>
21. Timoshenko, S. & Woinowsky-Krieger, S. *Theory of Plates and Shells*. (McGraw-Hill: New York, 1959).
22. Beardmore, P. & Fellers, J. Characteristic fracture features of polymethyl methacrylate. *Materials Science and Engineering* 5, 120-125
23. Bhattacharjee, D. & Knott, J. F. Effect of mixed mode I and II loading on the fracture surface of polymethyl methacrylate (PMMA). *Int J Fract* 72, 359-381 (1995).

## CHAPTER 2

### 2. EFFECT OF HYDROSTATIC STRESS ON STRESS RELAXATION IN GLASSY POLYMERS

#### Abstract

The effect of stress state on stress relaxation in PMMA and PC is investigated. Direct comparisons are made between uniaxial and biaxial loading conditions. Standard dogbone specimens are used for uniaxial tests while a modified shrink fit technique allows for equi-biaxial stress relaxation experiments. The methods used highlight the effect of hydrostatic stress on the relaxation process. The data shows an increase in relaxation time and increase in the breadth of the relaxation spectrum with increases in hydrostatic stress. This suggests that the stress state can have a significant effect on the useful lifetime of pre-stressed articles.

#### Introduction

Having demonstrated some beneficial aspects of pre-stress on impact performance in the previous Chapter, it is appropriate to elaborate on some of the potential disadvantages of the technique. The application of compressive pre-stress increases the impact resistance of PMMA and the magnitude of improvement is proportional to the level of

pre-stress. Since polymeric materials, are viscoelastic, any applied stress will relax with time leading to a likely time dependent decay in pre-stress. With this knowledge in mind, it is sensible to question the feasibility of using pre-stress in “real world” applications. The goal of this thesis is not to develop a working product but rather to advance the understanding of failure mechanisms in glassy polymers. However, with the intent of providing a more complete story, some of these concerns will be briefly addressed here. Additionally, it will be shown that the shrink fit method provides for a unique experimental approach for the investigation of hydrostatic stress on the stress relaxation process.

### Materials

The materials used in this chapter include two PMMA homopolymers with molecular weights of 930,000 and 1,100,000 g/mol. Molecular weight was determined by GPC using THF as a solvent and polystyrene standards. The tacticity of the acrylics were quantified by NMR (See Chapter 4). A homopolymer of PC (Tuffac) finishes out the list of materials.

## Experimental

The viscoelastic response of PMMA and PC was probed with standard and non-standard stress relaxation experiments. Type I ASTM tensile bars were machined from 6 mm sheets using a Tensilkut fixture and router table. Uniaxial tensile stress relaxation was performed on an Instron 5800. The change in load with time was measured on a 50 kN capacity load cell using Instron's Merlin software. Temperature of 25° C was controlled by a Thermcraft oven and temperature controller. For biaxial stress relaxation, the shrink fit method, similar to that described in the previous Chapter, was used. The disks were fabricated from 6 mm thick sheets of PMMA and PC. The circular shape was machined to the appropriate dimensions using a milling machine equipped with a rotating indexing table. The change in stress with time was measured by applying a strain gage on the outer surface of the steel ring so that the strain in the  $\theta$  direction could be measured. The strain was measured using a quarter bridge Wheatstone bridge controlled by LabView software. In this way, the steel ring served as a biaxial load cell. The time dependent stress in the shrink fit polymer disk can be calculated using Hooke's law and the elasticity equations for a cylinder with internal pressure.<sup>24</sup>

$$\text{Eq) 2-1} \quad \sigma_r(t) = \sigma_\theta(t) = \frac{\varepsilon_\theta(t)}{2} \left[ \frac{\nu_m E_m}{(1 + \nu_m)(1 - 2\nu_m)} + \frac{E_m}{(1 + \nu_m)} \right] \left[ \left( \frac{b}{a} \right)^2 - 1 \right]$$

Where,  $\sigma_r$  and  $\sigma_\theta$  are the time dependent stresses in the polymer disk in the radial and theta directions.  $\varepsilon_\theta$  is the time dependent strain on the surface of the steel ring in the theta direction.  $E_m$  and  $\nu_m$  are Young's modulus and Poisson's ratio of steel.  $a$  and  $b$  refer to the inner and outer radii of the steel ring, respectively. In long term experiments such as these, temperature stabilization is critical. Accordingly, extra care was taken to reduce temperature variation throughout the life of the test. The temperature was controlled by placing the assembly inside a polyethylene bag then placing the bag inside a water bath maintained at  $25 \pm 1^\circ \text{C}$ .

### Relaxation

Attempts were made to construct a master curve of stress relaxation in shrink fit samples, however difficulties were encountered. When the temperature was raised, the added thermal expansion of the PMMA caused the disks to buckle so that the relaxation response could not be measured accurately. This highlights one disadvantage of characterizing stress relaxation through the shrink fit technique. Aside from the material properties of the material under investigation and that of the supporting ring, the initial stress in the sample is determined by the radial mismatch between the two. There is no way to "fine tune" the level of strain other than through fabrication of rings and disks with different dimensions.

## Results and Discussion

General trends are consistent across the three materials summarized in Table 2-1 and in Figures 2-1 through 2-9. The time

Eq) 2-2 
$$\tau_{oct} = \frac{1}{3} \left[ (\sigma_1 - \sigma_2)^2 + (\sigma_2 - \sigma_3)^2 + (\sigma_1 - \sigma_3)^2 \right]^{1/2}$$

dependent octahedral shear stress is plotted against  $\log(t)$  and each data set is fit with a KWW type stretched exponential function.

Table 2-1. Summary of relaxation experiments.

### Linear Regression - Relaxation Time

<i>Model</i>		<i>Factors</i>	<i>P-values</i>
P-value	0.02	Intercept	1.6E-05
Adjusted R <sup>2</sup>	0.70	Stress State	0.01
		MW	0.47

In Equation 2-3,  $\tau$  with no subscript represents the relaxation time (not shear stress) for the stress relaxation process and  $\beta$  is the stretching exponent interpreted as a phenomenological characterization of the breadth of the distribution of relaxation times associated with the

Eq) 2-3 
$$\tau_{oct}(t) = \tau_0 \exp\left(-\left(\frac{t}{\tau}\right)^\beta\right)$$

process.

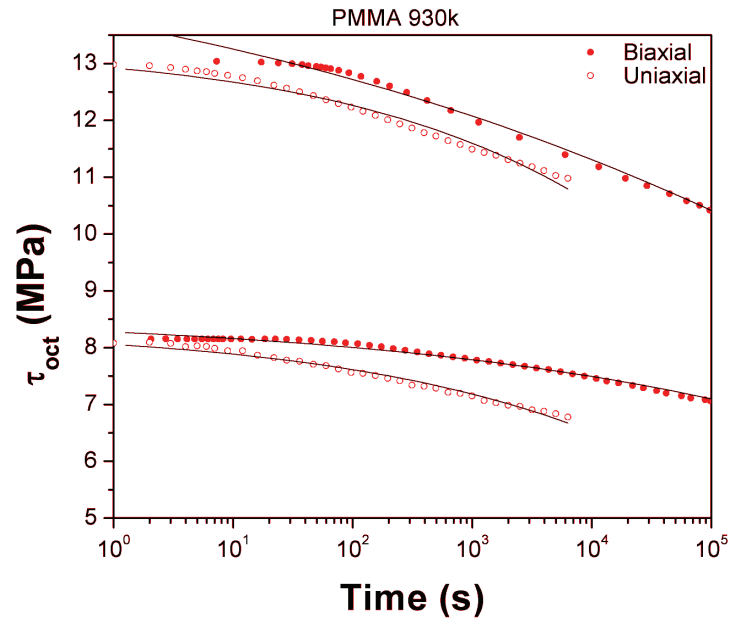


Figure 2-1. Comparison of uniaxial and biaxial stress relaxation in 930 kg/mol PMMA.

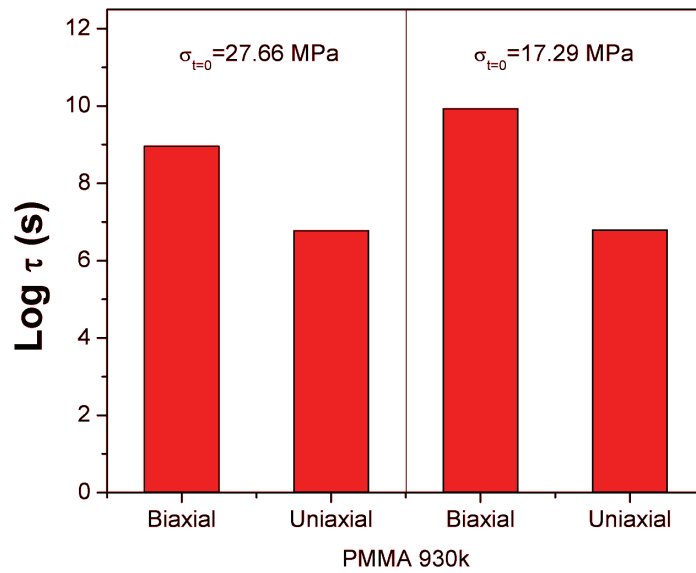


Figure 2-2. Effect of stress state on relaxation time in 930 kg/mol PMMA.

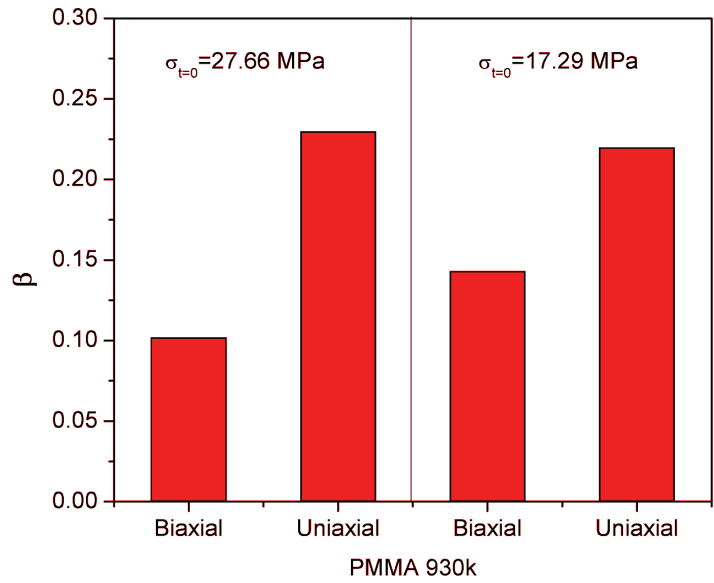


Figure 2-3. Effect of stress state on stretching exponent,  $\beta$  in 930 kg/mol PMMA.

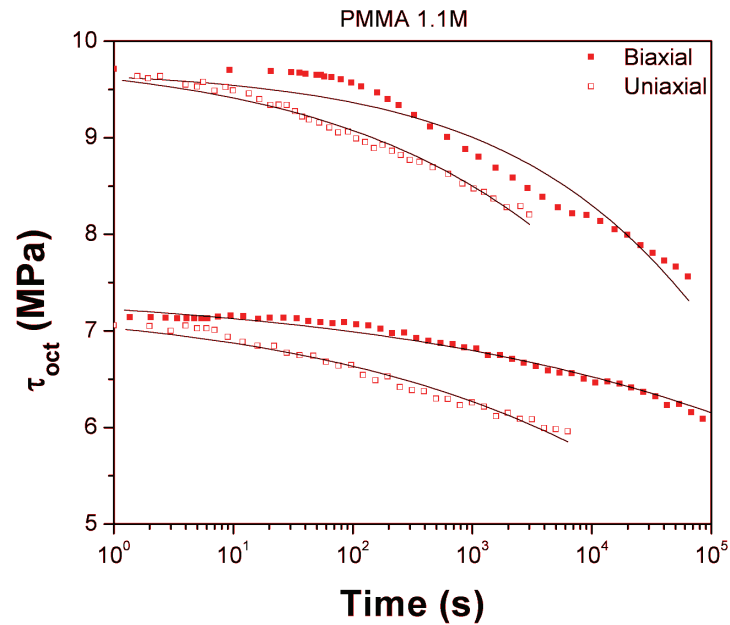


Figure 2-4. Stress relaxation under uniaxial tension and biaxial compression for PMMA 1,100 kg/mol.

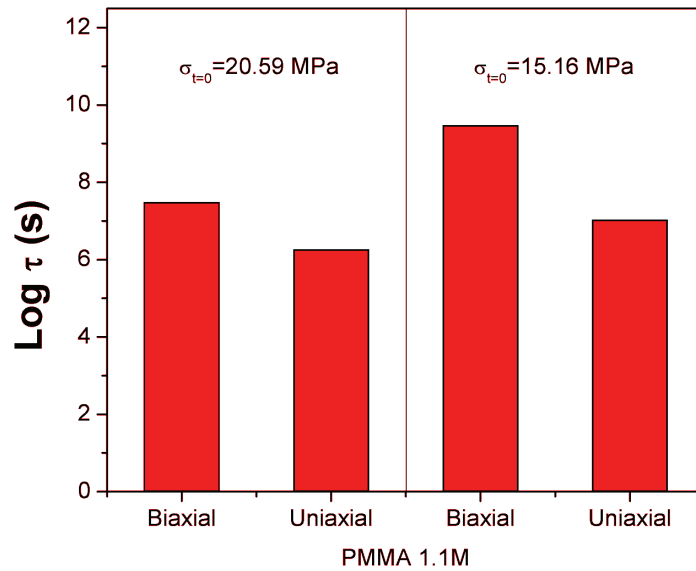


Figure 2-5. Effect of stress state on relaxation time in 1,100 kg/mol PMMA.

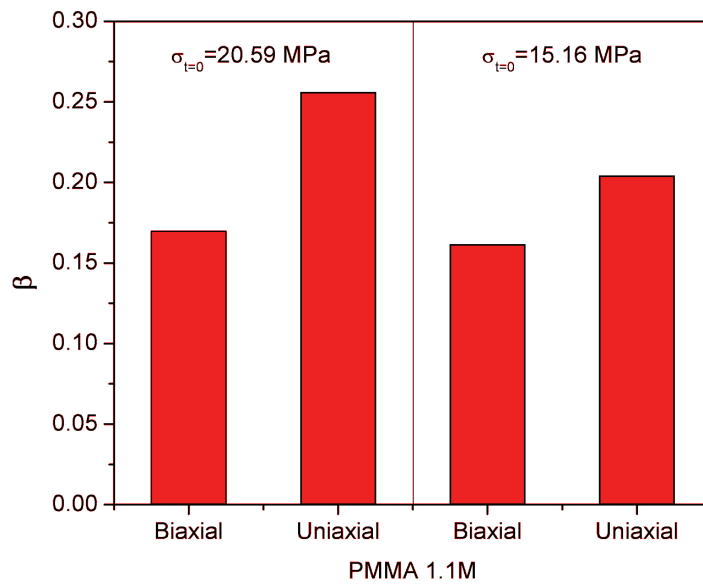


Figure 2-6. Stretching parameter  $\beta$  from KWW fit for PMMA 1,100 kg/mol.

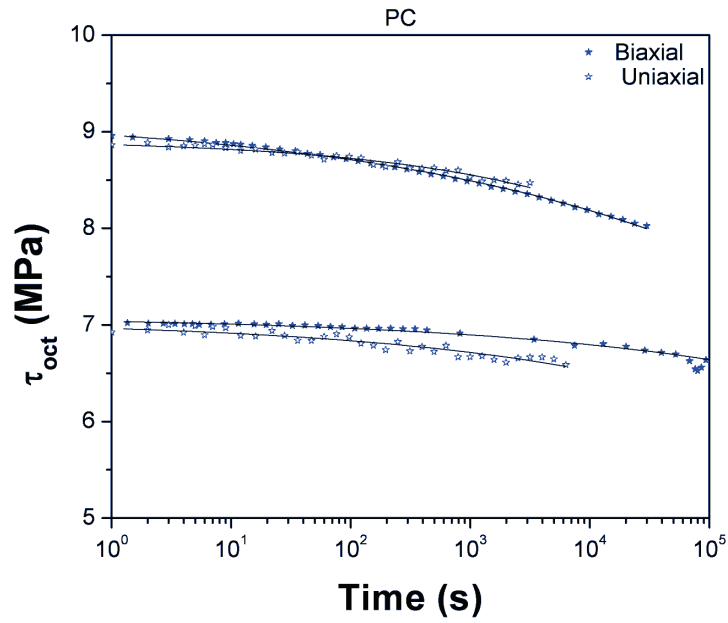


Figure 2-7. Stress relaxation under uniaxial tension and biaxial compression for PC.

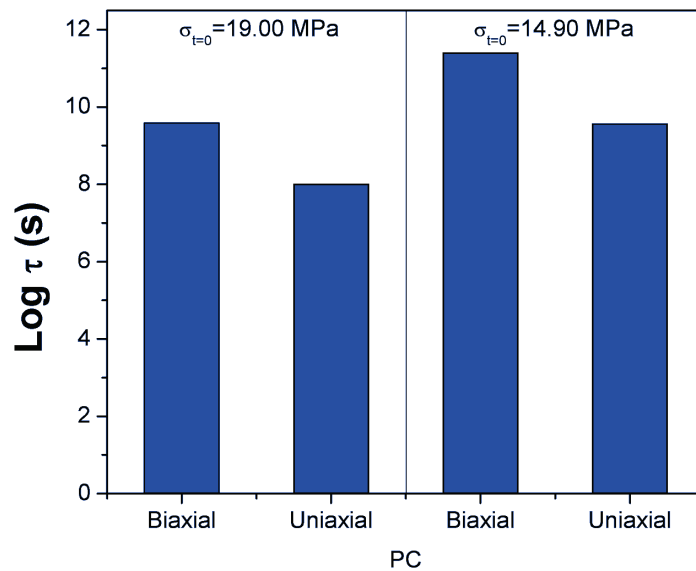


Figure 2-8. Relaxation time from KWW fit for PC.

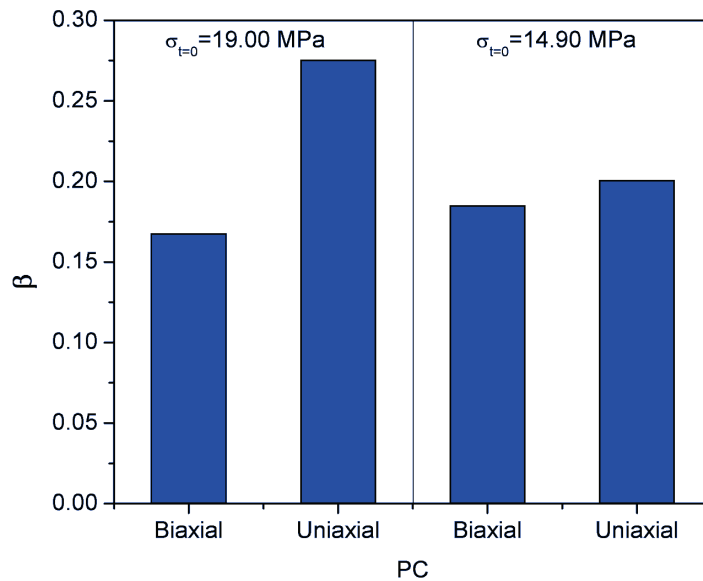


Figure 2-9. Stretching parameter  $\beta$  from KWW fit for PC.

For a given material at equivalent levels of  $\sigma_0$  ( $\sigma_0$  = stress at  $t=0$ ), relaxation times,  $\tau$ , are longer and the stretching exponent,  $\beta$ , is smaller for the case of biaxial compression. The decrease in  $\beta$  corresponds to a phenomenological broadening of the relaxation spectrum. This data suggests that in an application where pre-stress is used to improve impact resistance, the lifetime of the pre-stress will depend on the state of stress. Increasing levels of hydrostatic compression result in increased life of the pre-stress at a give level of shear stress.

We can gain further insight into these results by comparing the hydrostatic stress ( $\sigma_m$ ) and the octahedral shear stress ( $\tau_{oct}$ ) for uniaxial

tension and equi-biaxial compression. For uniaxial tension, let  $\sigma_{11} = \sigma_0$  and for equi-biaxial compression, let  $\sigma_{11} = \sigma_{22} = \sigma_0$ . For these conditions,  $\sigma_m = \sigma_0/3$  for uniaxial and  $\sigma_m = -2\sigma_0/3$  for equi-biaxial (sign convention:  $\sigma_m$  results in an increase in volume). It should be noted that, for a given value of  $\sigma_0$ , the octahedral shear stress is identical for uniaxial and equi-biaxial loading,  $\tau_{oct} = 2^{1/2}\sigma_0/3$ . Also, the corresponding values for the hydrostatic stress are opposite in sign and their difference is conveniently equal to  $\sigma_0$ . Another significant difference between these two stress states is that the magnitude of the hydrostatic stress for the equi-biaxial case is twice that of the uniaxial case and increases more rapidly than the octahedral shear stress for increases in  $\sigma_0$ . Typically, as  $\tau_{oct}$  and  $\sigma_m$  are increased, relaxation times are decreased.<sup>25,26</sup> The shear stress drives the change in shape while the hydrostatic stress accelerates the process for  $+\sigma_m$  and decelerates the process for  $-\sigma_m$ . For members loaded in uniaxial tension, increases in  $\sigma_0$  increase both  $\tau_{oct}$  and  $\sigma_m$  so one would expect relaxation times to decrease with higher levels of  $\sigma_0$ . In contrast, increases in  $\sigma_0$  for the equi-biaxial compressive state of stress increase  $\tau_{oct}$  and decrease  $\sigma_m$ .

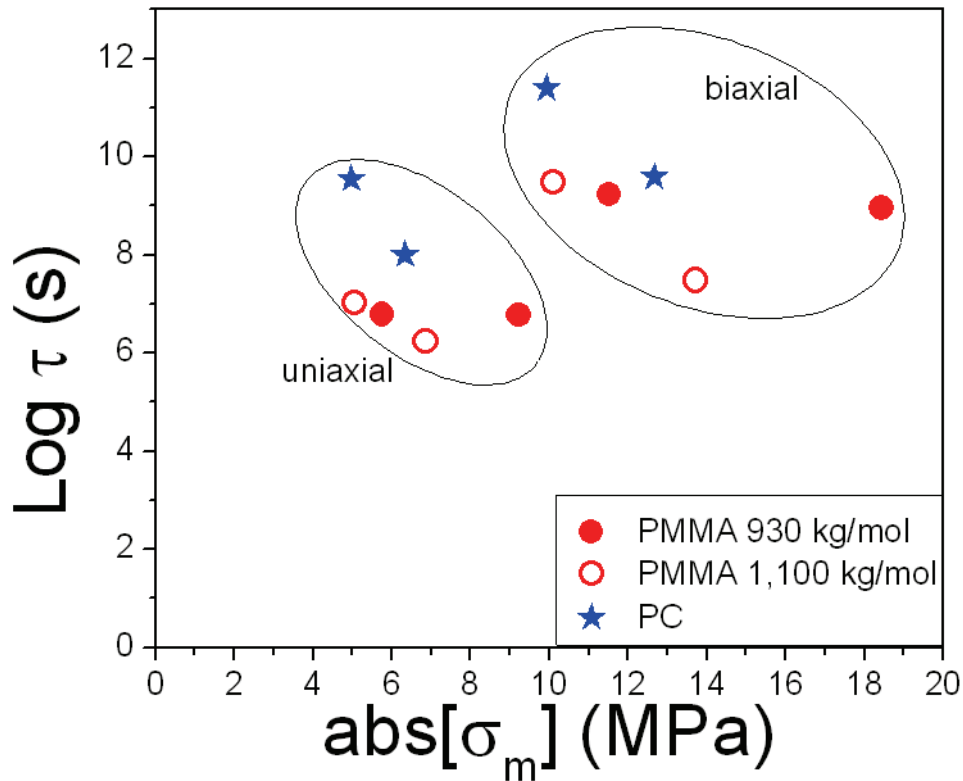


Figure 2-10. Log of relaxation time vs. absolute value of hydrostatic stress.

These effects of hydrostatic stress can be understood in terms of its effect on free volume. As free volume is decreased, cooperative molecular motions such as those required for stress relaxation and the glass transition are restricted. This is seen in the increase of yield stress or  $T_g$  with hydrostatic pressure.<sup>27-33</sup>

The two PMMA homopolymers used in this study differ in molecular weight. Linear regression analysis was conducted using coded levels for molecular weight and stress state (MW: 1,100 kg/mol = 1, 930

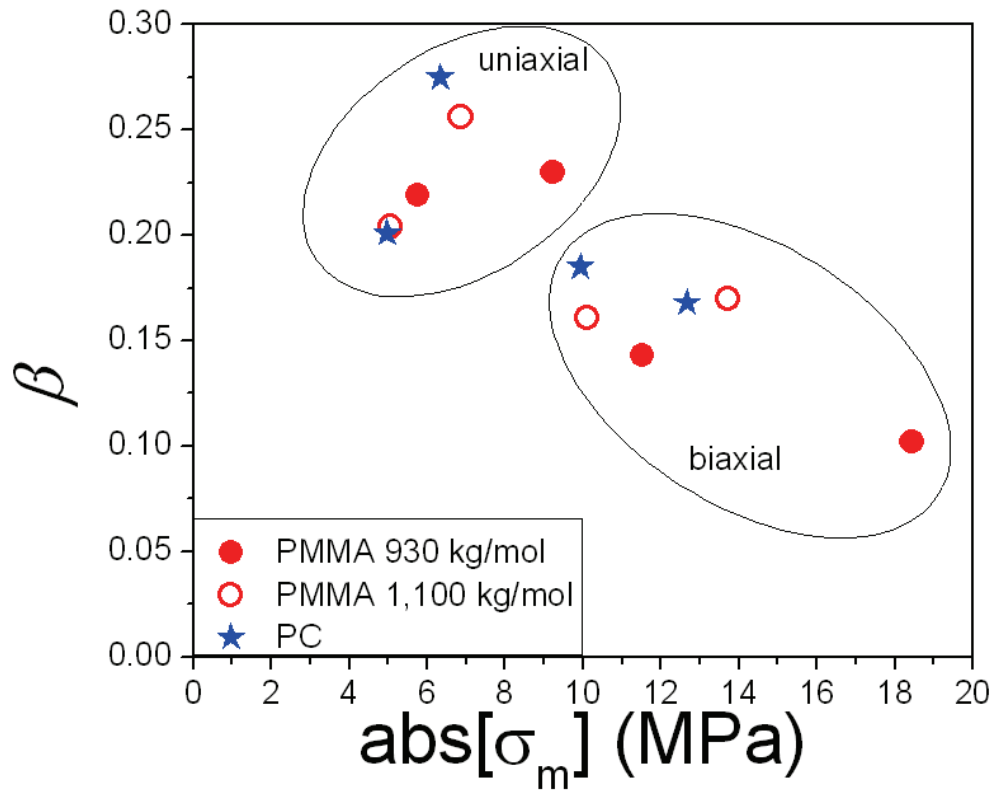


Figure 2-11. Stretching exponent vs. absolute value of hydrostatic stress.

kg/mol = 0; stress state: biaxial = 1, uniaxial = 0). Molecular weight was not shown to have a significant effect on relaxation time or the stretching exponent (significance as determined by  $P < 0.05$ ).

Table 2-2 Coded values for regression analysis.

Linear Regression - Relaxation Time			
Model		Factors	P-values
P-value	0.02	Intercept	1.6E-05
Adjusted R <sup>2</sup>	0.70	Stress State	0.01
		MW	0.47

Table 2-3 Summary of regression analysis on relaxation time.

Linear Regression - Relaxation Time			
<i>Model</i>		<i>Factors</i>	<i>P-values</i>
P-value	0.02	Intercept	1.6E-05
Adjusted R <sup>2</sup>	0.70	Stress State	0.01
		MW	0.47

Table 2-4 Summary of regression analysis on stretching exponent.

Linear Regression - Stretching Exponent			
<i>Model</i>		<i>Factors</i>	<i>P-values</i>
P-value	0.01	Intercept	3.0E-05
Adjusted R <sup>2</sup>	0.77	Stress State	0.005
		MW	0.22

Another interesting result in this data comes from the comparison of PC to PMMA. PMMA has a rather substantial effect of hydrostatic pressure on the stress relaxation process while the effect, although present, is significantly diminished in PC. Similar effects are reported in the literature regarding the effect of pressure on yielding of these two glassy polymers.<sup>30</sup> Perez et al quantified the pressure parameter,  $\mu$ , for PMMA and PC by measuring yield stress as a function of stress state and temperature. They found  $\mu = 0.23$  for PMMA and  $\mu = 0.10$  for PC deformed at 20° C. The authors reported increases in  $\mu$  corresponding with proximity to either the  $\alpha$  or  $\beta$  transition of the polymer. The effect of the  $\alpha$  or  $\beta$  transitions on the deformation response of glassy polymers will be investigated further in Chapter 4.

This experimental approach provides a clean way to probe the effect of hydrostatic stress on relaxation. An example of this is the work by Lu and Knauss who studied the effect of dilation on creep using annular samples of PMMA subjected to mutiaxial loading in the form of torsional and uniaxial loading.<sup>25</sup> One issue with the interpretation of their data arises when comparing the response of a specimen under only shear loading to one that has the same shear load in addition to an axial load. If the applied shear stress is the same, the superposed axial load adds an additional amount to  $\tau_{oct}$  so that the observed result is in response to changes in both  $\tau_{oct}$  and  $\sigma_m$ . If uniaxial and equi-biaxial tests are run at the same value of  $\sigma_0$ , as they are in this chapter,  $\tau_{oct}$  will be the same and any differences in the response will be due to the changes in  $\sigma_m$ .

## Conclusions

The stress relaxation experiments highlight the important role of hydrostatic stress in the stress relaxation process. When the mean stress is compressive, increases in relaxation times follow. This important result suggests that specimens subjected to higher levels of compressive pre-stress will not only perform better under impact but will also retain these improvements for longer times than the uniaxial equivalent.

## References

24. Saada, A. S. *Elasticity: Theory and Applications*. (Krieger: Malabar, Florida, 1993).
25. Lu, H. & Knauss, W. G. The role of dilatation in the nonlinearly viscoelastic behavior of PMMA under multiaxial stress states. *Mechanics of Time-Dependent Materials* **2**, 307-334 (1998).
26. Gol'dman, A. Y., Demenchuk, N. P. & Murzakhanov, G. K. Stress relaxation in polymeric materials under hydrostatic pressure. *Mech Compos Mater* **24**, 707-714 (1989).
27. Price, C. Effect of pressure on the formation of poly(methyl methacrylate) glasses. *Polymer* **16**, 585-589
28. Sauer, J. Deformation, yield and fracture of polymers at high pressure. *Polymer Engineering and Science* **17**, 150-164 (1977).
29. Wang, W. C. V., Kramer, E. J. & Sachse, W. H. Effects of high-pressure CO<sub>2</sub> on the glass transition temperature and mechanical properties of polystyrene. *Journal of Polymer Science: Polymer Physics Edition* **20**, 1371-1384 (1982).
30. Quinson, R., Perez, J., Rink, M. & Pavan, A. Yield criteria for amorphous glassy polymers. *J Mater Sci* **32**, 1371-1379 (1997).
31. Hasan, O., Boyce, M., Li, X. & Berko, S. An investigation of the yield and postyield behavior and corresponding structure of poly (methyl methacrylate). *J. Polym. Sci. B Polym. Phys.* **31**, 185-197 (1993).

32. O'reilly, J. M. The effect of pressure on glass temperature and dielectric relaxation time of polyvinyl acetate. *J. Polym. Sci.* 57, 429-444 (1962).
33. Rabinowitz, S., Ward, I. M. & Parry, J. S. C. The effect of hydrostatic pressure on the shear yield behaviour of polymers. *J Mater Sci* 5, 29-39 (1970).

## CHAPTER 3

### 3. SHEAR BAND FORMATION AND MODE II FRACTURE OF GLASSY POLYMERS

#### Abstract

Mode I and II fracture studies were performed from quasi-static to low velocity impact rates on polymethyl methacrylate (PMMA) and polycarbonate (PC). Mode II tests used an angled double-edge notched specimen loaded in compression. The shear banding response of PMMA is shown to be highly sensitive to rate, with diffuse shear bands forming at low rates and sharp distinct shear bands forming at high rates. As the rate increases, shear deformation becomes more localized to the point where Mode II fracture occurs. PC is much less rate dependent and stable shear band propagation is observed over the range of rates studied with lesser amounts of localization. A new theory is formulated relating orientation in a shear band to intrinsic material properties obtained from true-stress true-strain tests. In a qualitative sense the theory predicts the high rate sensitivity of PMMA. A kinematic limit for orientation within a shear band is also derived based on entanglement network parameters. Mode II fracture in PMMA is shown to occur at this kinematic limit. For the case of PC, the maximum impact rates were not high enough to reach the kinematic limit.

## Introduction

Polymethyl methacrylate (PMMA) and polycarbonate (PC) have been used throughout the literature as model glassy polymers. From a fracture mechanics perspective, these two materials offer a nice contrast in fracture mechanisms. Typically, PMMA fails in a brittle fashion while PC deforms in a ductile manner, as was mentioned in Chapter 1. The plastic deformation that accompanies the ductile failure process in PC absorbs large amounts of energy leading to higher impact energy absorption than brittle PMMA. However, this is not always the case. Song and coworkers have shown that at ballistic rates and high plate thicknesses, PMMA outperforms PC.<sup>34</sup> At the high rates where this crossover occurs, surface area created during radial cracking in PMMA is reduced and the failure pattern is more localized. This is a curious result in that the dominant energy absorption mechanism in brittle fracture is the creation of surface area. If the damage area decreases, one would expect a decrease in energy absorption rather than the observed increase. In Chapter 1, compressive pre-stress also resulted in suppression of radial cracking in PMMA along with increased impact resistance. To further understand this behavior, we will explore the change in fracture properties as a function of rate in this Chapter.

The most striking result from Chapter 1 is that the failure stress increase is significantly higher when samples are subjected to a shear pre-stress in addition to a compressive pre-stress. It is clear from these results that stress state can affect the fracture properties. What remains unclear is whether or not shear pre-stress can induce mixed mode fracture. Moreover, if a Mode II mechanism is activated, what effect will it have on fracture properties?

The work in Chapter 1 and in reference 2 both involve a circularly supported plate impacted normal to the surface.<sup>35</sup> During impact, fracture can initiate on the contact surface or on the non-contact surface. Separating the effects of different fracture modes becomes difficult in these types of tests simply because of the complications introduced by the geometry. To simplify interpretation, we will investigate the rate effects on Mode I and Mode II fracture separately with controlled geometries.

The characterization of Mode I fracture is relatively straight forward and standard techniques are used in this Chapter. However, there are issues surrounding Mode II fracture in polymers that warrant further background and explanation.

## Mode II Fracture

The general approach to achieve Mode II fracture is to apply a critical shear stress to a pre-cracked specimen. If Mode II fracture occurs, a crack should propagate along the direction of the pre-crack. However, the typical response is propagation via a Mode I kink.<sup>36,37</sup> This behavior is nicely illustrated by Figure 3-1, which shows a PMMA Cracked Brazilian Disc loaded in compression under pure Mode II conditions. Rather than growing collinear with the diametral pre-crack, the cracks initiate at an approximate angle of 72° relative to the pre-crack. During propagation the path of the crack curves in the direction of the loading axis and by doing so, minimizes the amount of shear stress at the crack tip. This observation that pre-cracks loaded under shear propagate at some angle to the pre-crack led to the development of the Maximum Tangential Stress (MTS) criterion of Erdogan and Sih.<sup>38</sup> This theory essentially states that a loaded pre-crack will grow in the direction in which the tangential stress is the highest and therefore, will proceed through a Mode I dominate mechanism. This suggests that for most materials, the Mode I fracture toughness,  $K_{IC}$ , is less than the Mode II fracture toughness,  $K_{IIc}$ . If this is the case, a necessary condition for achieving Mode II fracture is suppression of Mode I fracture. Accordingly, Melin posited that a pre-crack loaded under Mode II conditions will extend without Mode I kinking if the in plane compressive stresses are high enough to suppress Mode I

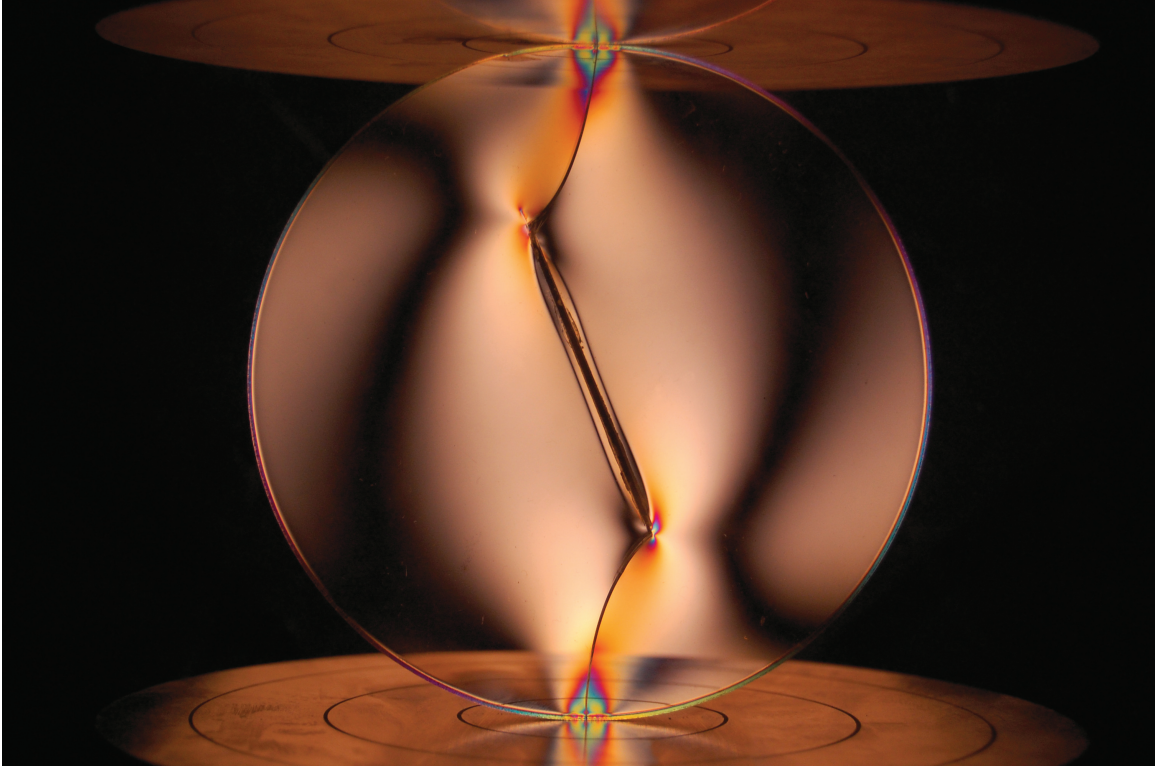


Figure 3-1. Cracked Brazilian Disc of PMMA loaded in pure Mode II. Mode I cracks initiate at an angle of  $72^\circ$  relative to the pre-crack as predicted by the MTS criterion illustrating that  $K_{IIc} > K_{Ic}$ . Disc diameter = 101 mm.

fracture.<sup>39</sup> Broberg experimentally verified this prediction by loading a pre-cracked plate of PMMA under biaxial compression.<sup>40</sup> The rate of loading was not specified but was likely in the quasi-static range. This is generally agreed to be the first evidence of the realization of Mode II fracture in a polymer. Values of  $K_{IIc}$  were shown to be  $\sim 2.5$  times higher than  $K_{Ic}$ .<sup>40</sup>

Other examples from the literature have shown that a transition to Mode II fracture can also occur at high loading rates. Kalthoff used the shadow optical method of caustics to investigate dynamic Mode II loading

in high strength maraging steel.<sup>41</sup> At low loading rates ( $\sim 10$  m/s) cracks would grow under Mode I conditions at an approximate angle of  $70^\circ$  as predicted by the MTS criterion. However, above some critical loading rate the failure mechanism changed from a Normal Stress dominated failure to that initiated by shear bands extending in the direction of the pre-cracks. Ravi-Chandar et al. took a similar approach to Kalthoff and studied PMMA and PC.<sup>42</sup> Their work used photoelasticity and high speed imaging to measure the dynamic fracture toughness of both materials. A rate dependent transition to Mode II fracture was also observed.

The motivation for the work presented in this Chapter is to investigate in depth the rate-dependent material properties that can lead to Mode II fracture in glassy polymers. Since shear bands are the precursor to Mode II fracture, we will characterize the effect of rate on shear band formation. We will also develop conditions for shear band stability based on both a force balance and a kinematic approach.

## Materials

The PMMA used was Acrylite GP purchased from K-Mac Plastics. The PC was Tuffak general-purpose grade supplied by Arkema.

## Experimental

### Mode I Fracture

To test Mode I properties a three point bend specimen was used. Samples were machined to nominal dimensions of 28 x 85 x 6 mm. Pre-cracks were made at the center of the 85 mm edge with nominal length of 14 mm. The pre-crack was formed by first making a cut with a diamond saw and then a sharp crack tip was achieved by taping a razor blade in the slot with a hammer. Three point bend tests were conducted on an Instron 5800 at quasi-static crosshead displacement rates and on a Dynatup 8250 at low-velocity impact rates. The displacement rates tested were 0.1, 1, 10, 100, 100k, 148k, 196k, and 245k mm/min, where k = 1000. The first four rates were within the capabilities of the Instron while the final four made use of the Dynatup with a 3.27 kg mass. The loading pins were 6 mm in diameter with exception of tests performed on the Dynatup, where a 9.5 mm diameter hemispherical tup impacted the

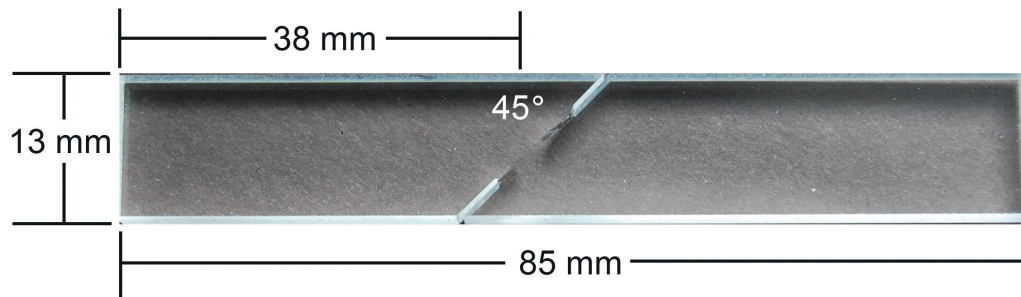


Figure 3-2. Mode II sample dimensions. Thickness = 6 mm.

sample. The span of the bottom loading pins was 60 mm. Testing was done at standard ambient conditions of 23° C and 50% relative humidity.

### Mode II Deformation and Fracture

Mode II specimens were machined to rectangular shapes with nominal dimensions of 13 x 85 x 6 mm (Figure 3-2). Each specimen was pre-cracked from both edges at an angle of 45° so that the center of the area between the pre-cracks was ~38 mm from one edge. The pre-crack was formed by the same method as the three point bend specimens. The total pre-crack length was on the order of 13 mm. The specimen was loaded in compression along the axis corresponding to the 85 mm dimension. To prevent buckling of the sample during compressive loading, a simple steel support jig was used during testing at all rates (Figure 3-3). The sample was aligned so that the area between the pre-cracks was visible in the viewing hole. The four screws were finger tightened to lightly secure the sample without significantly restricting deformation during testing. When the sample was loaded in the jig, ~10 mm of length was left unsupported to allow for adequate axial compression of the sample prior to failure. Compressive crosshead displacement rates ranging from 0.1-500 mm/min were achieved in an Intron 5800. For testing at rates up to 253 k mm/min, a Dynatup 8250 was used. To measure the shear strain within the shear bands, a series of

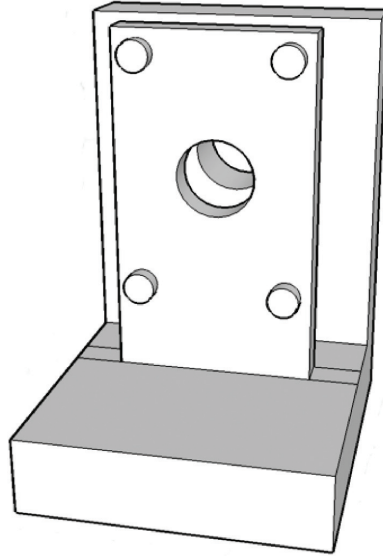


Figure 3-3. Support jig to prohibit buckling during compressive loading in Mode II tests. Center hole is for illuminating and viewing sample deformation.

lines normal to the plane of the shear band were drawn on the surface. During the shear banding tests, images were taken at known time intervals. For crosshead displacement rates less than 100 mm/min, a digital still camera was used to capture the images. The time interval between images from the still camera was determined by two methods. At a crosshead displacement rate of 0.1 mm/min, a timer with an LCD showing elapsed seconds was placed next to the sample so that each image contained the time difference to the nearest second. This gave adequate precision considering the deformation takes place over 30 minutes. For crosshead displacement rates from 1-32 mm/min, a dial indicator displaying crosshead displacement was placed so that its reading was contained in each image. The time interval between images

was calculated using the crosshead displacement rate and the change in the displacement between images. For crosshead displacement rates 100 mm/min and higher, a high speed camera was used to capture the images. The time interval between images was determined by the camera frame rate. The local maximum shear strain rate in the shear band was calculated by measuring the shear strain in the images and plotting this against time (Figure 3-4). A sigmoidal curve was fit to the data, and then this function was differentiated to arrive at the local maximum shear

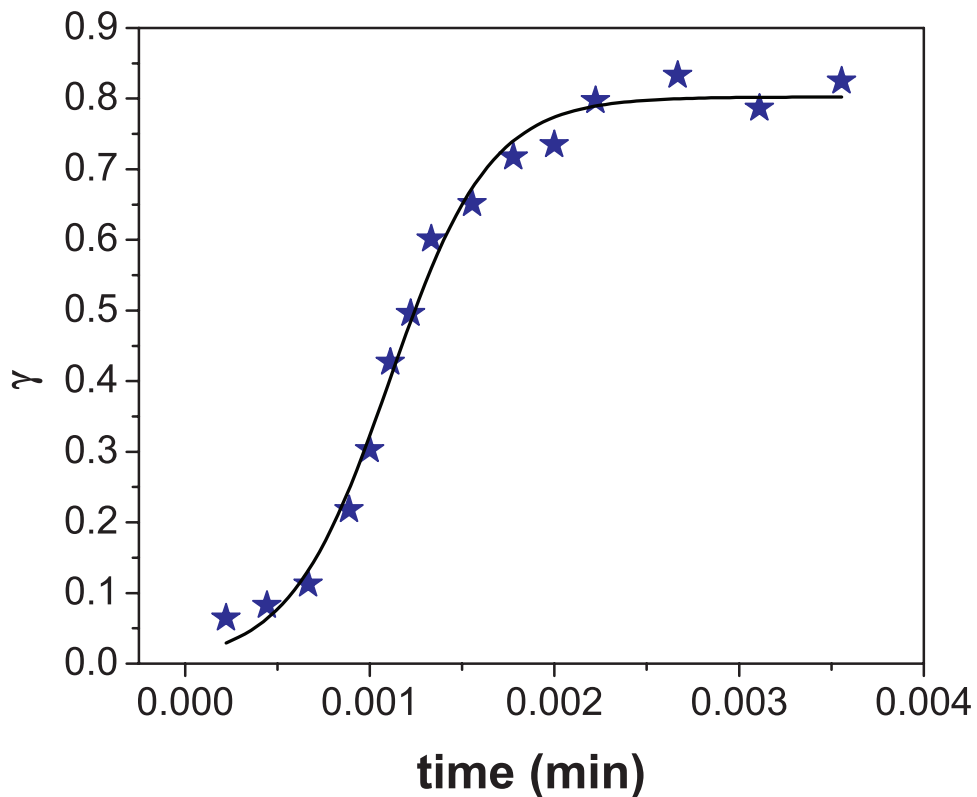


Figure 3-4. Shear strain as measured from image analysis vs. time used to calculate maximum shear strain rate and maximum shear strain.

strain rate. This curve was also used to define the maximum shear strain,  $\gamma_{max}$ . Low frame rate imaging of the samples during testing was captured with a Nikon D40 digital SLR camera. High speed imaging was performed on a Kodak Ektapro HS4540. Frame rates from 30–40,500 fps were used.

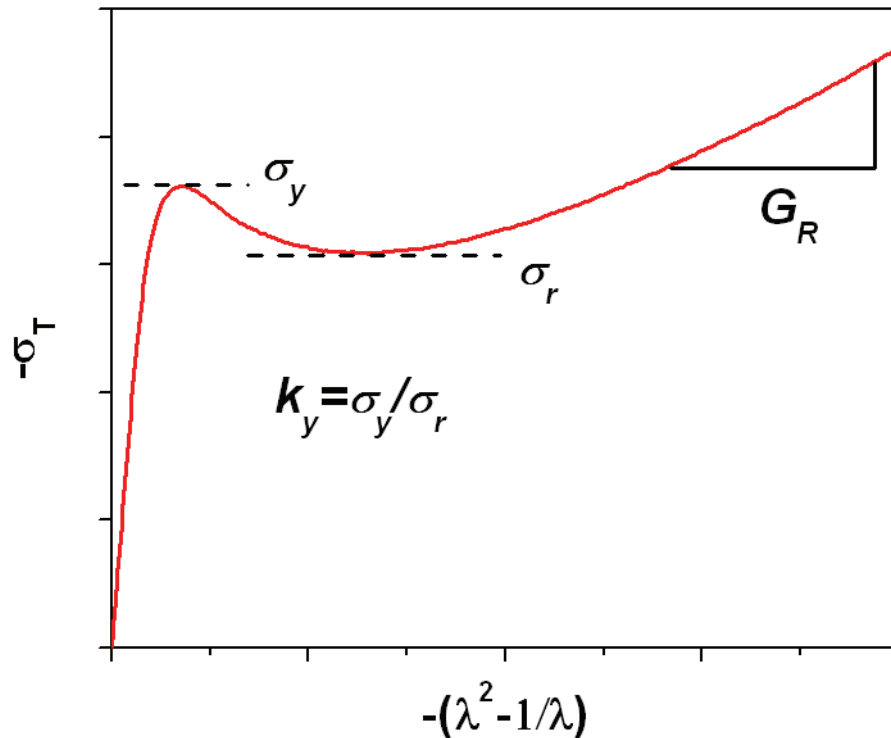


Figure 3-5. Intrinsic material properties obtained from true-stress true-strain compression tests.  $\sigma_y$ ,  $\sigma_r$ ,  $G_R$ , and  $k_y$  represent the yield stress, rejuvenated stress, strain hardening modulus and strain localization

## Compression

True stress-true strain compression tests were performed on both PMMA and PC over a range of temperatures and strain rates. Cylindrical samples were machined from sheet stock using a hole-cutting end mill with an inner diameter of 4.4 mm. The machining was done in a water bath to prevent excessive heating and consequent orientation at the machined surface. One end of the cylinder was then machined and wet polished with a polishing wheel using successively smaller grit down to 9 micron. Nominally, the final dimensions were height = diameter = 4.35

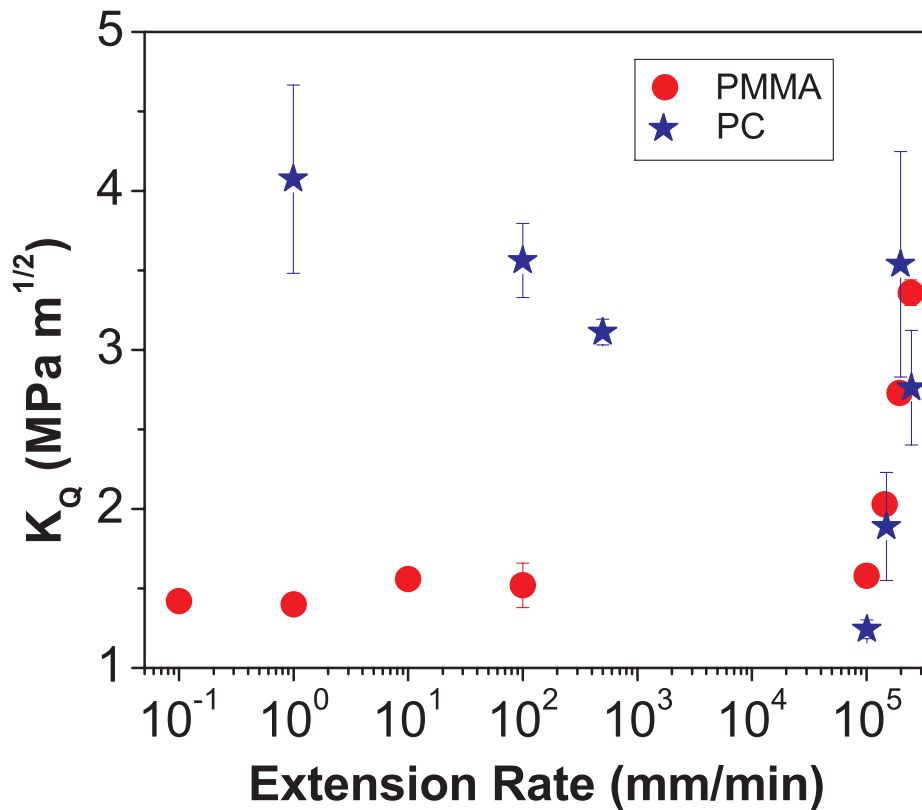


Figure 3-6. Mode I fracture toughness of PMMA and PC.

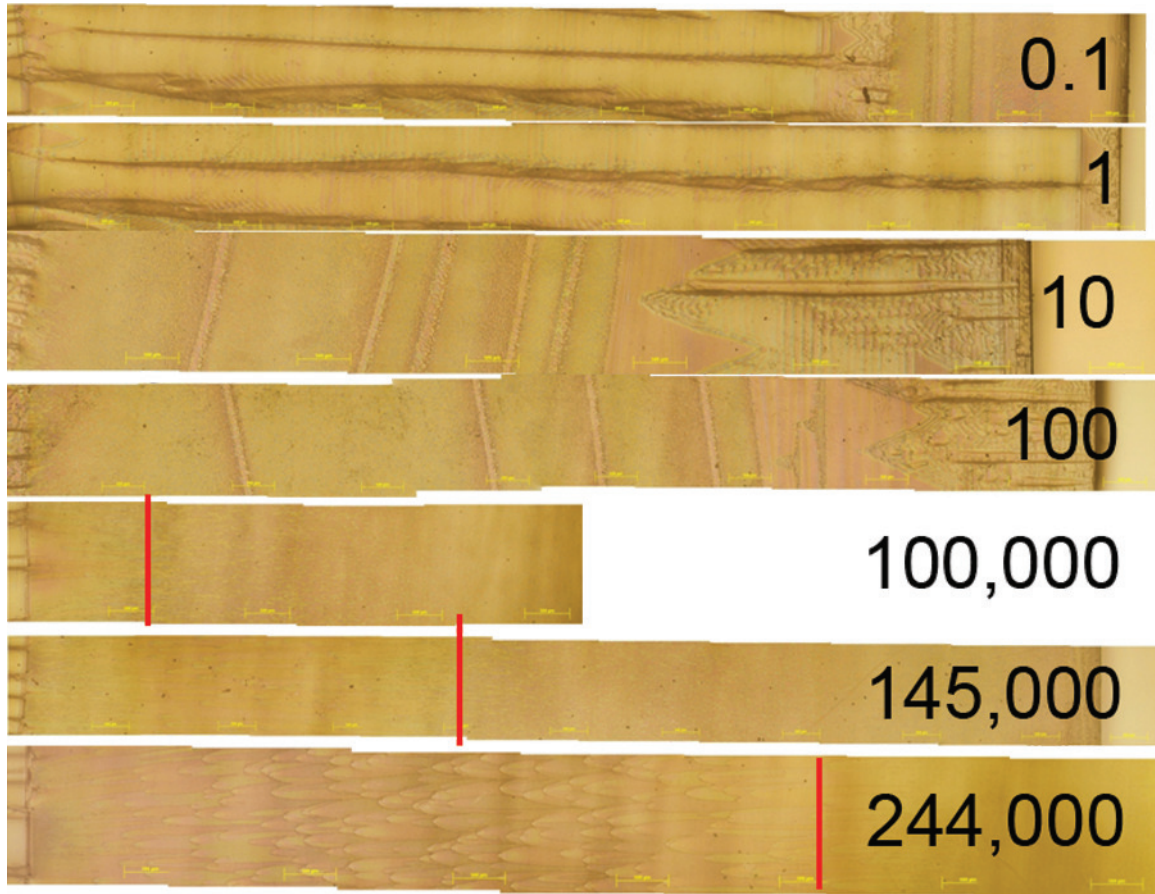


Figure 3-7. Mode I fracture surface morphology in PMMA. Numbers indicate impact rate in mm/min. Crack growth is from left to right. Vertical lines in bottom three images indicate boundary of parabolic markings. The height of each image = 1.3 mm.

mm. To ensure affine deformation, each end of the cylinder was covered with PTFE tape and a drop of lubricant was placed on each compression platen. For PMMA, silicone oil was used as a lubricant. For PC, uncrosslinked polydimethyl siloxane (PDMS) with molecular weight of 6000 g/mol was used. These silicone based lubricants were used rather than a water-surfactant mixture because of low temperature testing. PDMS was used for PC to avoid environmental stress cracking. The test

temperatures were 23°, -20°, and -60° C. Temperature was controlled with an oven using a Thermcraft controller and liquid nitrogen as the coolant. Samples were allowed to equilibrate at the test temperature for 1 h prior to testing. The load cell was maintained at room temperature during low temperature testing by wrapping the adjacent section of the load train with heating tape connected to a temperature controller. The constant strain rates used were 0.01, 0.1, and 1 min<sup>-1</sup>. The analysis of the data took into consideration the load train compliance, which was measured to be 2.40 x 10<sup>-8</sup> m/N. The material properties measured from these tests were the yield stress,  $\sigma_y$ , rejuvenated stress,  $\sigma_r$ , the strain hardening modulus,  $G_R$ , and the strain localization parameter  $k_y = \sigma_y / \sigma_r$  (Figure 3-5).  $\sigma_y$  and  $\sigma_r$  were determined from the local maxima and minima shown in

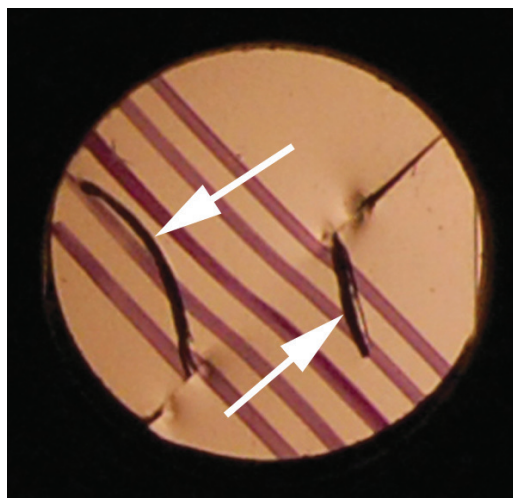


Figure 3-8. Arrows indicate Mode I kinks. Diameter = 12.7 mm.

Figure 3-5.  $G_R$  was determined from a linear regression of the data in the extension range;  $-(\lambda-1/\lambda) = 1.5:2$ .

## Results and Discussion

### Mode I

#### PMMA

The effect of rate on Mode I fracture toughness has been studied before and the results shown here are typical of those reported in the literature.<sup>43,44</sup> In the quasi-static range, the Mode I fracture toughness of PMMA shows modest increases with rate (Figure 3-6). Above a rate of 105 mm/min, the fracture toughness increases rapidly with rate. There is a

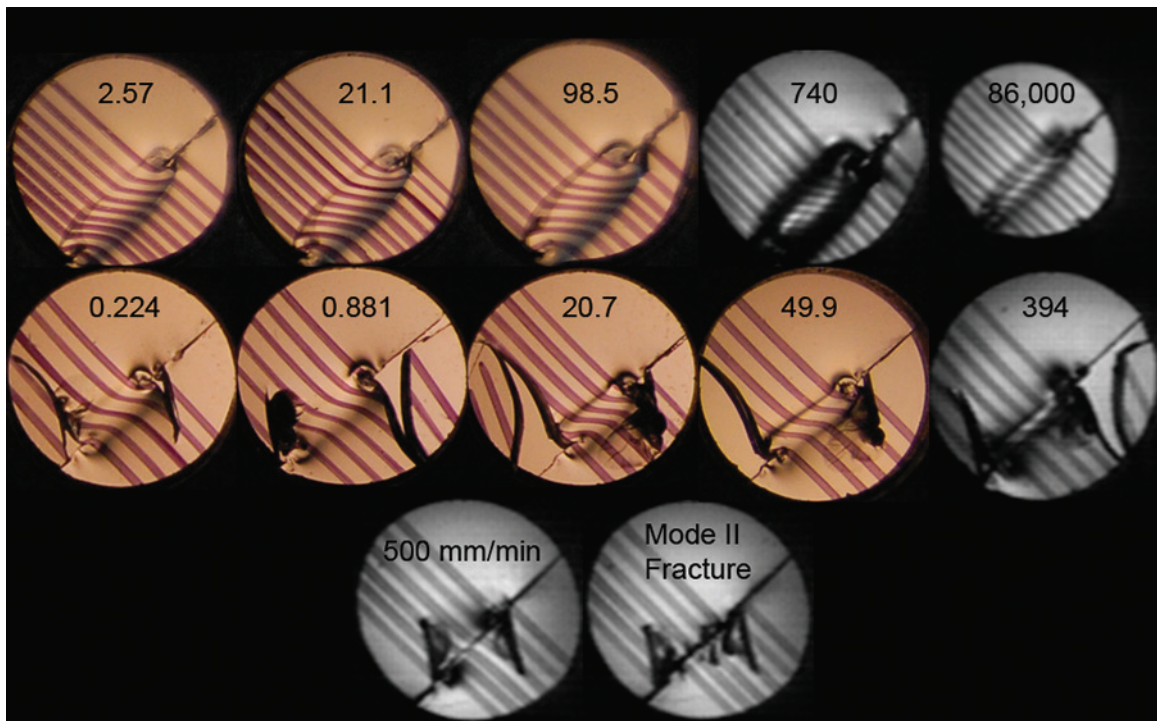


Figure 3-9. Effect of rate on shear band formation. First row PC, second and third rows PMMA. Numbers in first two rows indicate shear strain rate in  $\text{min}^{-1}$ . Diameter in each image = 12.7 mm.

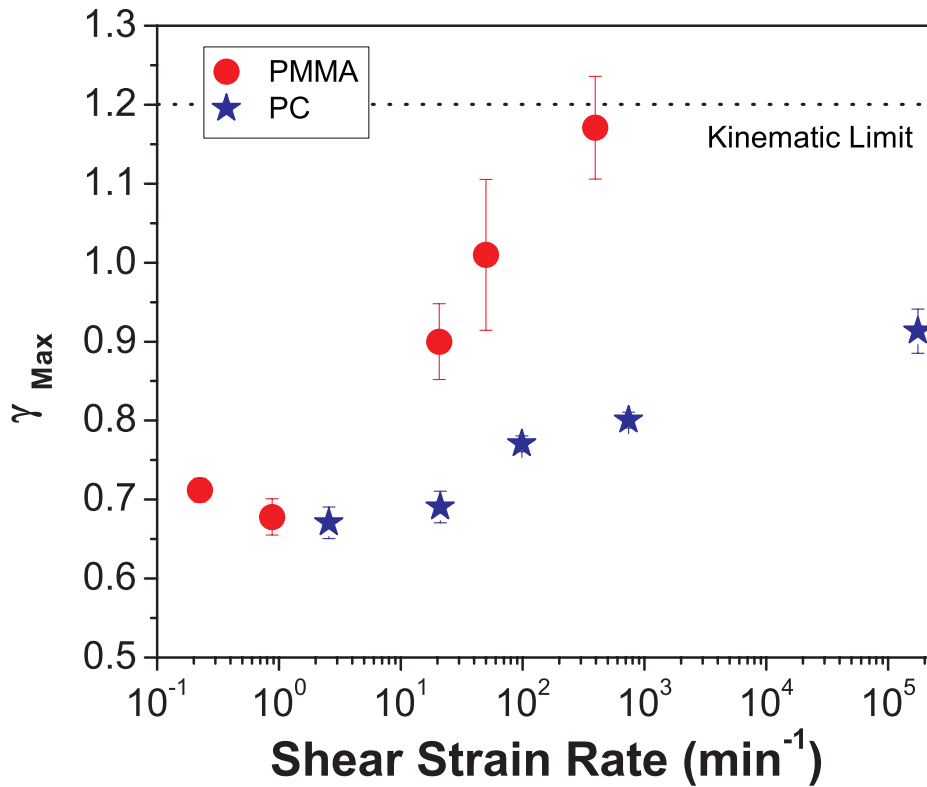


Figure 3-10. Maximum shear strain vs. shear strain rate for PC and PMMA.

corresponding shift in crack propagation stability and fracture surface morphology (Figure 3-7). At lower rates, crack growth is stable and morphologically the surface contains striations in the direction of crack growth along with fan markings toward the end of the crack. As impact speed increases, crack growth becomes more unstable as evidenced by lines of crack arrest on the surface. At the highest impact speeds, crack growth is unstable and the fractured surface shows parabolic markings associated with the initiation of secondary cracks ahead of the primary crack front.<sup>45,46</sup> With the onset of these parabolic markings comes the

drastic increase in fracture toughness. This high rate response is significant to this work in that it suggests a possible additional route to achieving Mode II fracture. In the shear banding experiments outlined in the following sections, Mode I failure is suppressed by compressive stress normal to the plane of interest. If by increasing the impact rate, the

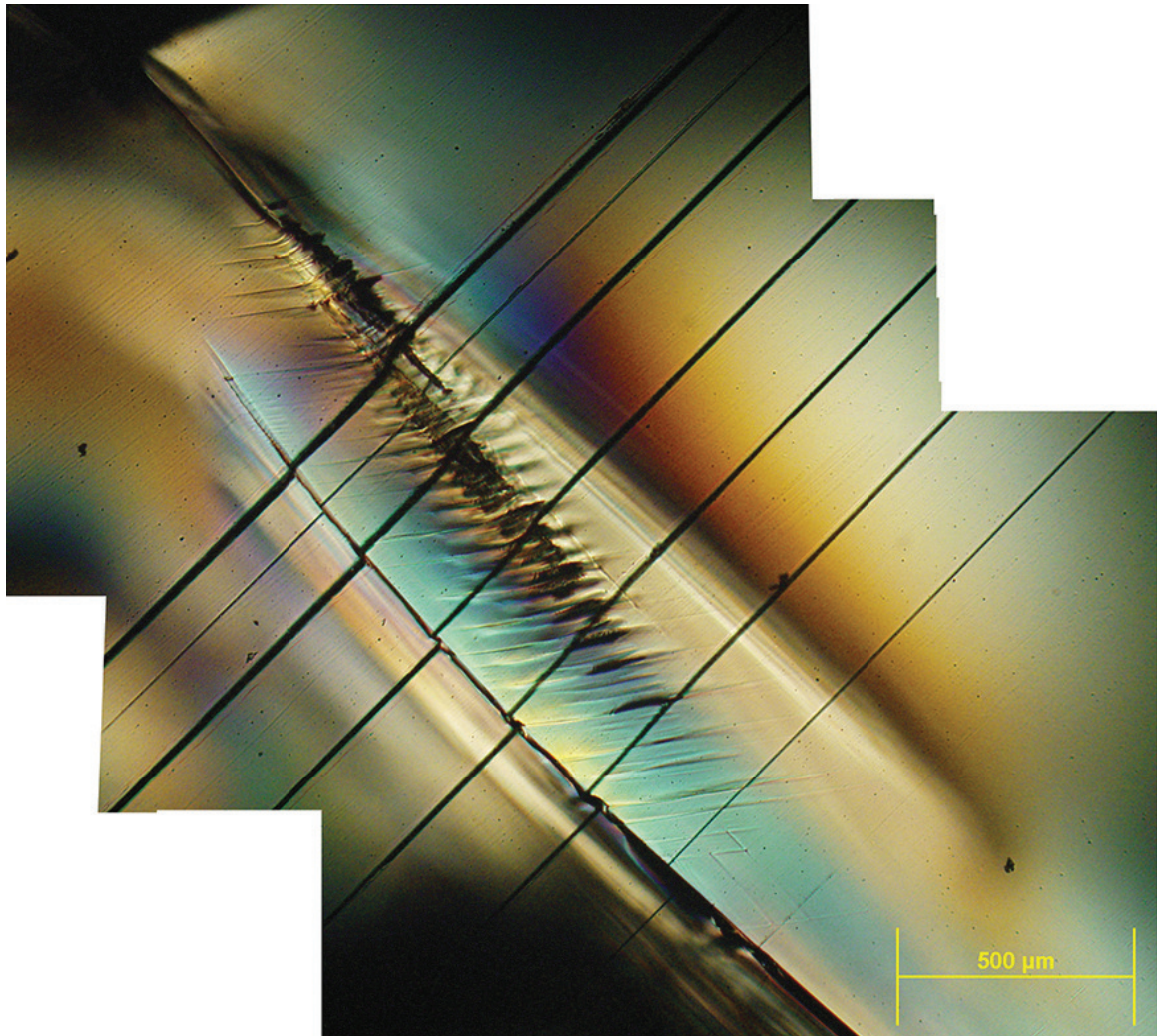


Figure 3-11. PMMA prior to complete Mode II fracture viewed under crossed polars. Black lines at  $45^\circ$  are surface marks for surface displacement reference. Shear band is identified by offset in reference lines. Shallow micro-tensile cracks form at  $\sim 45^\circ$  to shear bands. Scale bar =  $500 \mu\text{m}$ .

Mode I fracture toughness can be increased such that  $K_{IC} > K_{IIc}$ , Mode II will be the preferred fracture mechanism.

### PC

At low rates, the Mode I fracture toughness of PC exceeds that of PMMA by a factor of  $\sim 2.6$  (Figure 3-6). At these rates, the deformation behavior is highly ductile. As rate is increased there is a decrease in

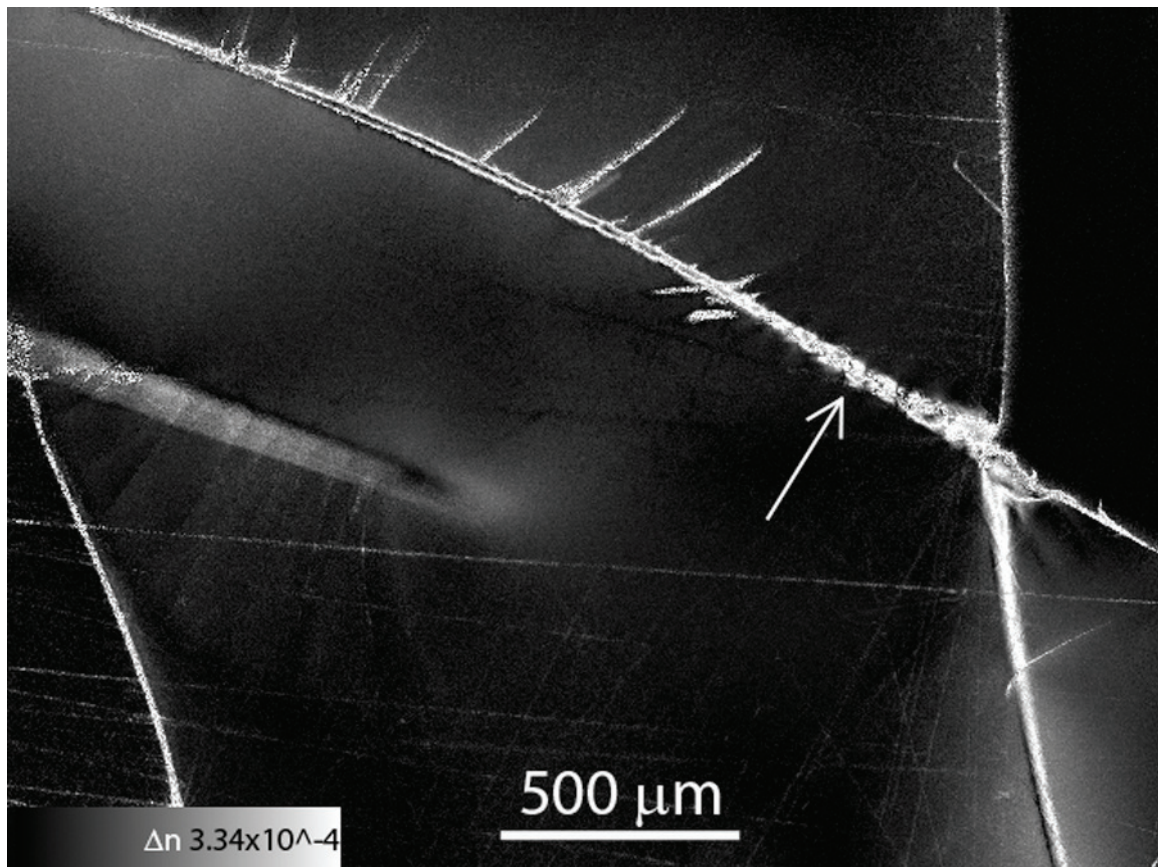


Figure 3-12. Map of birefringence of shear bands in PMMA prior to complete Mode II fracture. The level of birefringence is represented by the continuous grayscale in the image (black = 0, white =  $3.34 \times 10^{-4}$ ). Spatial scale bar =  $500 \ \mu\text{m}$ . The arrow indicates the location for the line scan of birefringence shown in Figure 3-13.

fracture toughness until the rate of 105 mm/min. At the crosshead displacement rate of 1 mm/min, PC undergoes ductile failure while at 500 mm/min, every sample fails in a brittle fashion. This ductile to brittle transition can be explained in terms of the Ludwig-Davidenkov-Orowan hypothesis.<sup>47</sup> This is simply a comparison of the effect of rate (or temperature) on the yield stress and the brittle fracture stress. At low rates, the yield stress is lower than the brittle fracture stress and the specimen will fracture in a ductile manner. As the rate increases, so does

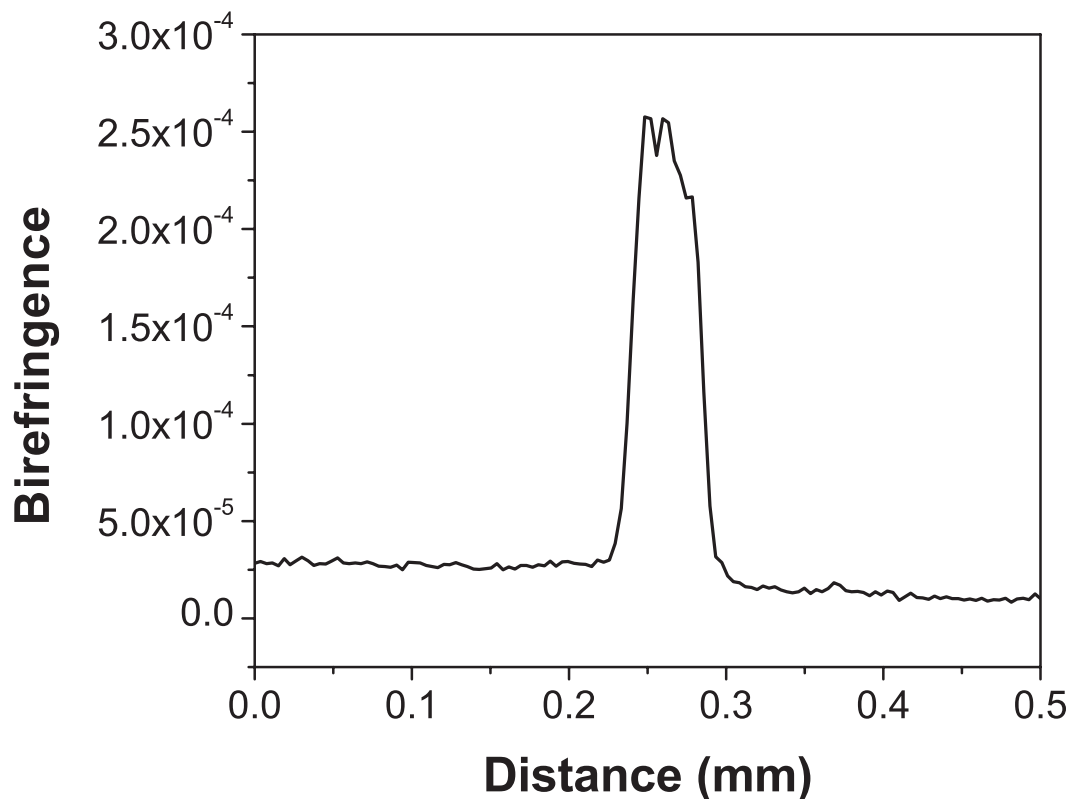


Figure 3-13. Spatial line scan of birefringence of shear band in PMMA.

the yield stress until a point where it exceeds the brittle fracture stress and a transition to brittle fracture is observed. At this point, a sharp increase in fracture toughness is observed similar to the response of PMMA (Figure 3-6).

#### Mode II - General Observations

At low crosshead displacement rates, a stable shear band forms connecting the two pre-cracks. As a consequence of this deformation, the material is locally oriented in the first principal direction. The width

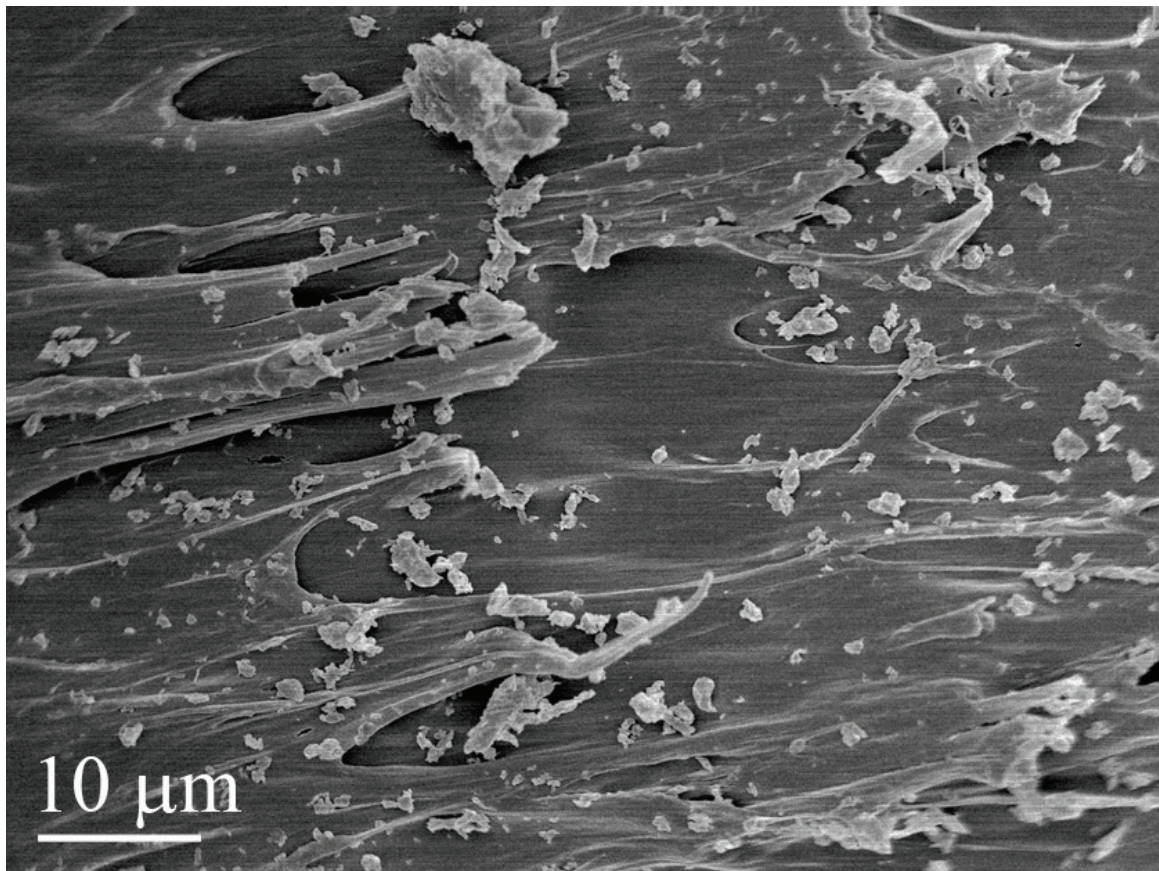


Figure 3-14. SEM image of Mode II fracture surface of PMMA.

of the shear band increases and more material is drawn into the band as a consequence of the strain hardening response. This general process holds many similarities to necking seen in uniaxial tensile tests of polymers. We will take advantage of these similarities later when we develop the condition of shear band stability.

One advantage of the specimen geometry is that, when under a compressive load, the plane containing the two pre-cracks experiences

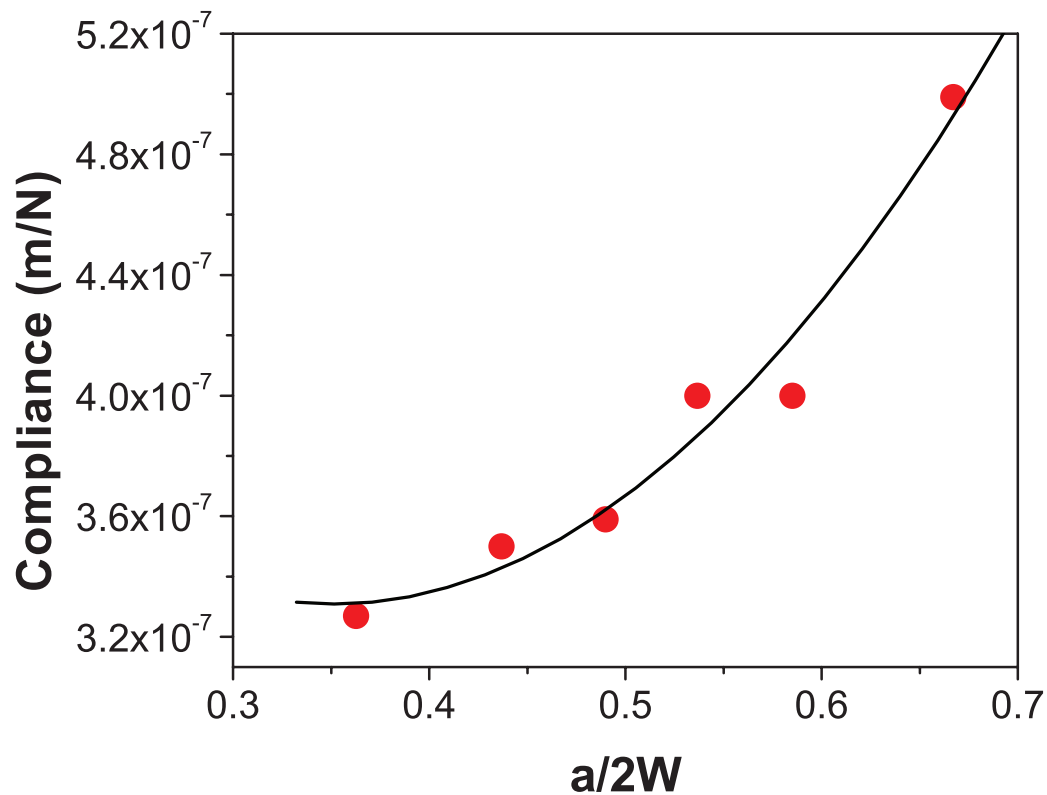


Figure 3-15. Relationship of sample compliance to crack length for Mode II specimens.

Eq 3-1) 
$$G_{IIC} = \frac{P^2}{2b} \frac{\partial C}{\partial a} = \frac{P^2}{2b} \left( C_1 \frac{a}{W^2} + C_2 \frac{1}{W} \right)$$

the maximum shear stress in addition to a compressive stress normal to the plane. This compression suppresses Mode I cracks in the plane of interest. However, tensile stresses do develop at the crack tip and reach a maximum at  $\sim 65^\circ$  with respect to the pre-crack plane, as evidenced by the Mode I kinks that form in PMMA (Figure 3-8). Another advantage of the geometry is that even in the presence of Mode I kinks, the sample still carries a load and the shear stress can continue to increase.

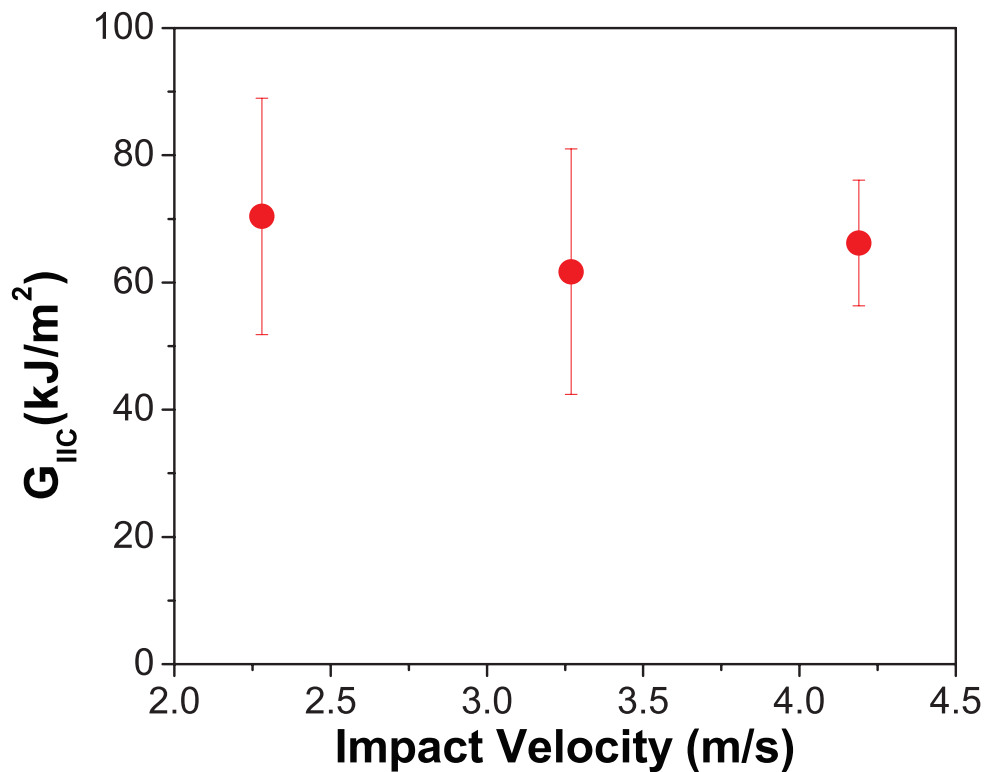


Figure 3-16. Mode II critical strain energy release rate for PMMA.

## PMMA

At shear strain rates from 0.2-394  $\text{min}^{-1}$ , stable shear bands are formed in PMMA with no Mode II fracture (Figures 3-9 and 3-10). As the rate is increased, the maximum shear strain in the band increases as the width of the band narrows. At crosshead displacement rates of 500 mm/min and higher, Mode II fracture is observed.

Eq 3-2) 
$$G = \frac{K^2(1-\nu^2)}{E}$$

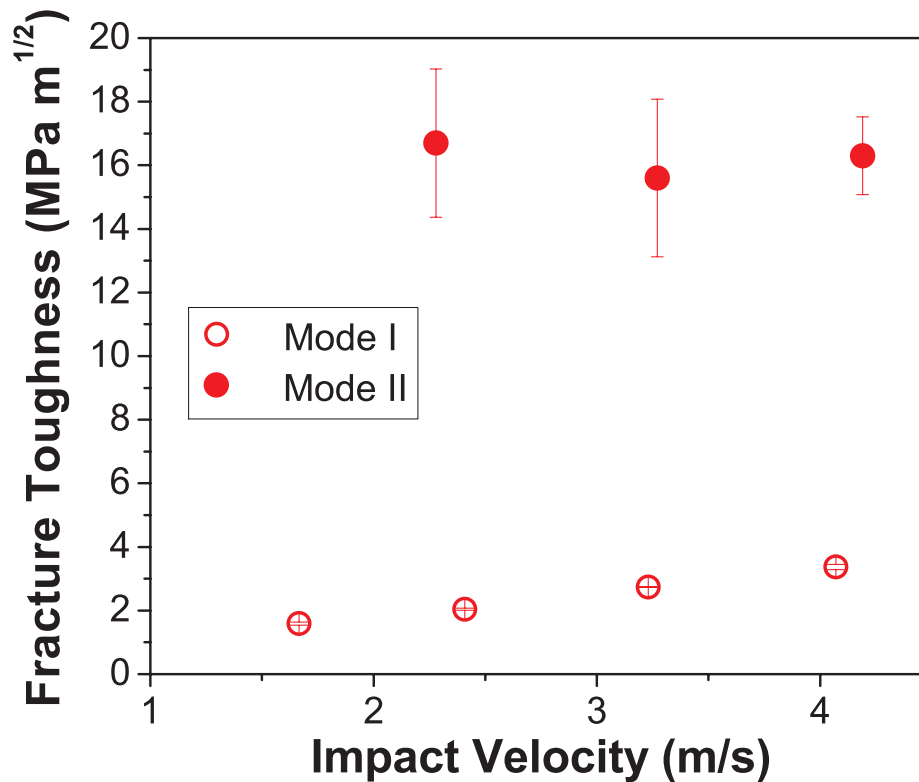


Figure 3-17. Comparison of Mode I and II fracture toughness in PMMA.

For the tests performed in the Dynatup on PMMA, following the Mode II fracture event, the two newly formed surfaces reseal and the load again rises until either all the kinetic energy of the falling mass is spent and the tup rebounds or fracture initiates at the tup-sample contact point.

Occasionally, due to contact stresses, the top portion of the sample will fracture prior to complete Mode II fracture. When this occurs, the release of the load is so quick that it provides a snapshot of the Mode II

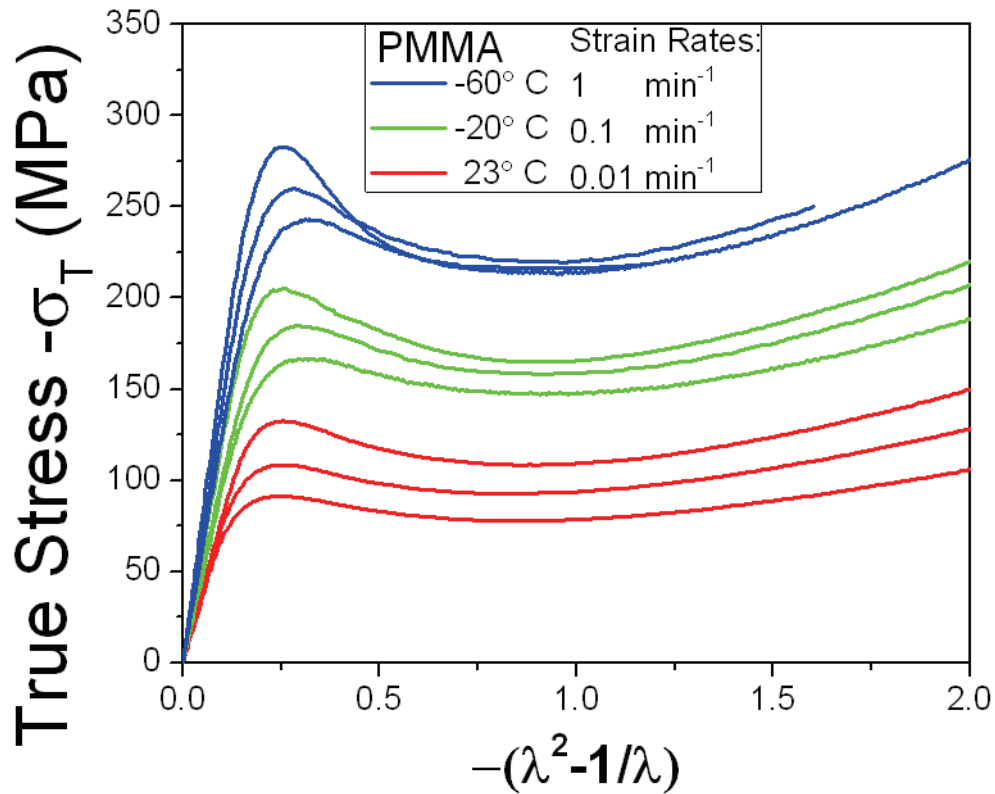


Figure 3-18. True-stress true-strain response of PMMA.

fracture process. Figure 3-11 is a striking example of this. The end of one pre-crack is shown in the top left hand corner of the image while the end of the other pre-crack is just out of view in the opposite corner. The series of black lines oriented at 45° are for reference and were made by tapping a stack of razor blades onto the surface prior to testing. Shear bands can be seen propagating from the tip of each pre-crack. The one on the left side of the image is easily identified as a shear band rather than a Mode I crack by noting the resultant offset in the surface reference

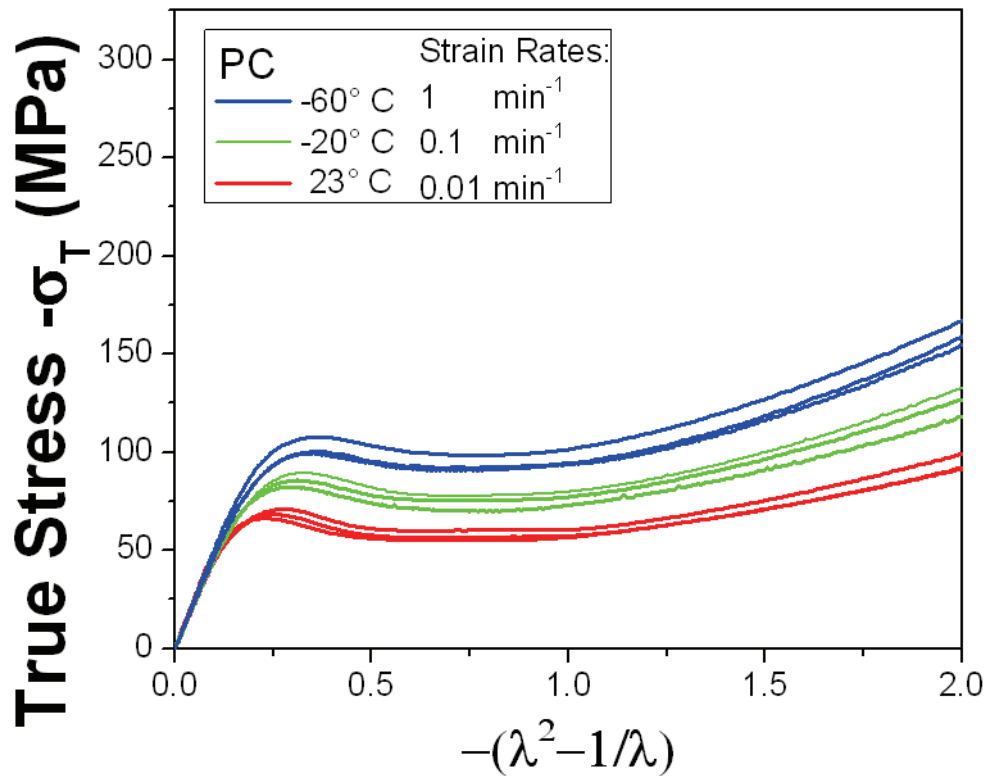


Figure 3-19. True-stress true-strain response of PC.

Table 3-1. Summary of compression testing on PMMA 930 kg/mol (SD = standard deviation).

PMMA 930 kg/mol										
$T$ (°C)	$\dot{\epsilon}$ ( $\text{min}^{-1}$ )	$\sigma_y$ (MPa)	SD	$\sigma_r$ (MPa)	SD	$k_y$	SD	$G_R$ (MPa)	SD	
23	0.01	93	2.5	80	2.2	1.162	0.004	42	3.6	
23	0.1	108	0.1	93	0.2	1.159	0.004	50	1.2	
23	1	130	3.0	104	3.4	1.245	0.012	55	4.6	
-20	0.01	168	0.5	149	1.6	1.126	0.009	62	-	
-20	0.1	190	4.8	165	5.9	1.156	0.013	77	9.9	
-20	1	214	7.6	169	3.8	1.262	0.017	80	-	
-60	0.01	227	15.0	206	8.0	1.101	0.031	97	-	
-60	0.1	254	5.5	221	2.9	1.153	0.030	-	-	
-60	1	273	9.2	210	5.1	1.298	0.012	-	-	

Table 3-2. Summary of compression testing on PC (SD = standard deviation).

PC										
$T$ (°C)	$\dot{\epsilon}$ ( $\text{min}^{-1}$ )	$\sigma_y$ (MPa)	SD	$\sigma_r$ (MPa)	SD	$k_y$	SD	$G_R$ (MPa)	SD	
23	0.01	67	1.5	56	0.6	1.209	0.016	49	2.1	
23	0.1	70	1.6	57	0.4	1.216	0.020	51	4.6	
23	1	71	1.1	60	0.4	1.201	0.023	51	2.5	
-20	0.01	80	1.9	70	1.6	1.145	0.024	68	4.0	
-20	0.1	85	1.2	76	0.4	1.120	0.011	72	1.7	
-20	1	88	0.8	79	0.6	1.120	0.019	76	1.0	
-60	0.01	94	7.3	86	6.3	1.093	0.005	79	9.6	
-60	0.1	99	2.0	92	1.0	1.085	0.012	84	7.5	
-60	1	105	2.9	96	2.7	1.093	0.009	82	8.4	

lines. The shear band on the right side had not yet reached the surface and shows no noticeable perturbation of the reference lines. The relative orientation and width of the shear band was measured by analyzing the birefringence of a cross section of the sample with a LC-Polscope Pro imaging system (Figure 3-12). The width of the shear band is on the order of 100  $\mu\text{m}$ . The maximum birefringence is above  $2.5 \times 10^{-4}$  while outside the shear band the orientation is negligible (Figure 3-13). This data shows that in the early stages of shear band formation, the deformation is highly localized. Between the two shear bands there is a series of horizontal features that because of their orientation to the applied stress field are believed to be micro-tensile cracks. These cracks

were only found on the surface shown in Figure 3-11 and were analyzed using fluorescent penetrant dye and confocal microscopy. The deepest of such cracks propagated to a depth of  $\sim 100 \mu\text{m}$ . The presence of these micro-cracks begs the question, is fracture proceeding through a Mode I process? The fracture mechanism of samples loaded in Mode II is frequently described as the coalescence of micro-tensile cracks rather than a shearing process, which should accompany true Mode II fracture.<sup>48,49</sup> Because of the shallow depth of the micro-cracks and their presence on only one surface, they are likely to have developed at the end of the process. In contrast, the shear bands occupy nearly the entire 6 mm of thickness and have grown past each other. Further evidence of Mode II fracture lies in the fracture surface morphology. The process of micro-tensile crack coalescence leaves a characteristic hackled surface morphology. The SEM image in Figure 3-14 shows the Mode II fracture surface, which does not have a hackled appearance. The surface shows evidence of flowing material indicative of a shearing process.

To determine the critical strain energy release rate,  $G_{IIc}$ , samples were prepared with a range of pre-crack lengths and the sample compliance was measured in an Instron 5800. The data points from the compliance measurements were plotted against  $a/2W$ , where  $a$  is the crack length and  $W$  is the width (Figure 3-15). The polynomial fit to this

data is used to determine  $\partial C/\partial a$  and allows one to arrive at an expression for  $G_{IIC}$ .

The fit gave the values for the constants  $C_1$  and  $C_2$  of  $8.10 \times 10^{-7}$  and  $-5.70 \times 10^{-7}$ , respectively. Using Equation 3-1 and the critical failure loads,  $G_{IIC}$  for PMMA was calculated for three different rates (Figure 3-17). Over the range of velocities tested there is no clear correlation between  $G_{IIC}$  and impact velocity. Strain energy release rate can be related to fracture toughness in the case of plane strain using the relation,

From the data presented in Figure 3-17,  $K_{IIC}/K_{IC} \sim 6.7$ . This value is a conservative estimate since the values for modulus and Poisson's ratio used were measured at quasi-static rates. This result is of great practical significance since it suggests that if one were to suppress Mode I fracture completely, the increases in fracture toughness would be substantial. Previous work by the authors has looked at suppressing Mode I fracture through the superposition of a compressive pre-stress.<sup>35</sup> In those results, even though Mode I fracture was not suppressed completely, significant improvements in impact strength occurred when a shear prestress was superposed with the compressive prestress.

## PC

Qualitatively, the shear band response of PC is similar to that of PMMA in that both show increased shear strain with increased loading rate (Figure 3-9). However, the rate dependence of PC is significantly lower than PMMA (Figure 3-10). Over the entire range of rates, PC was able to form a stable shear band and Mode II fracture was not observed.

### Intrinsic Material Properties

The true-stress true-strain experiments allow for the determination of intrinsic material properties such as the yield stress,  $\sigma_y$ , rejuvenated stress,  $\sigma_r$ , and the strain hardening modulus,  $G_R$  (Figures 3-5, 3-18, and 3-19). These parameters have been used by several authors including Haward, Meijer, Govaert, and Boyce to describe necking behavior in polymers.<sup>50-52</sup> We will now develop the condition for shear band stability based on these intrinsic material properties.

### Condition For Shear Band Stability

As noted earlier, there are some qualitative similarities between shear band and neck growth. In the general sense, once either process has been initiated, propagation proceeds in a self-similar manner as more material is drawn into the oriented state. Taking advantage of these similarities, we will now develop the condition for shear band stability.

The key assumptions in this development are: no change in cross-sectional area during deformation and material incompressibility. In essence this is a force balance between the applied farfield shear stress and the true shear stress in the shear band,  $\tau_0 A_0 = \tau A$ . From incompressibility,  $\lambda_1 \lambda_2 \lambda_3 = 1$  and from constant cross sectional area,  $\lambda_1 \lambda_3 = 1$  and  $\lambda_2 = 1$ . Let  $\lambda_1 = \lambda$ ,  $\lambda_3 = 1/\lambda$ . From rubber elasticity,

$$\text{Eq 3-3)} \quad f = \frac{1}{2} G_R (\lambda_1^2 + \lambda_2^2 + \lambda_3^2 - 3)$$

where  $f$  is the strain energy density,  $G_R$  is the strain hardening modulus and  $\lambda_i$  is the extension ratio in the  $i$  direction. After substitution,

$$\text{Eq 3-4)} \quad f = \frac{1}{2} G_R \left( \lambda - \frac{1}{\lambda} \right)^2$$

Let,

$$\text{Eq 3-5)} \quad \gamma = \lambda - \frac{1}{\lambda}$$

Where  $\gamma$  is the shear strain. Differentiating to obtain the true shear stress,

$$\text{Eq 3-6)} \quad \tau = \frac{\partial f}{\partial \gamma} = G_R \left( \lambda - \frac{1}{\lambda} \right)$$

Stable shear band propagation will occur after strain softening and at a farfield stress of  $\tau_0 = \sigma_y$ . The force balance is then,  $\tau_0 A_0 = \tau_y A_0 = \tau A$ . If there is no change in cross-sectional area, then  $A_0 = A$  and  $\tau_y = \tau$ . After strain softening,

$$\text{Eq 3-7)} \quad \tau_y = \tau_r + G_R \left( \lambda - \frac{1}{\lambda} \right)$$

Introducing the strain softening parameter,  $k_y = \tau_y/\tau_r$ ,

$$\text{Eq 3-8)} \quad \tau_y = \frac{\tau_y}{k_y} + G_R \left( \lambda - \frac{1}{\lambda} \right)$$

Rearranging and substituting for the octahedral shear stress,  $\tau_{oct} = 2^{1/2}\sigma_y/3$

$$\text{Eq 3-9)} \quad \frac{\sqrt{2}\sigma_y}{3G_R} = \frac{\lambda - \lambda^{-1}}{1 - k_y^{-1}}$$

This relationship allows one to relate the intrinsic material properties;  $\sigma_y$ ,  $\sigma_r$ , and  $G_R$  to the amount of orientation in a shear band. This is shown graphically in Figure 3-20. The material properties derived from true-stress true-strain compression tests are used to predict the corresponding orientation within the shear band. During the testing of PMMA at lower temperatures, failure occurred prior to the onset of strain hardening disallowing the calculation of  $G_R$ . In these cases, a master curve of  $G_R$  versus strain rate was used to extrapolate the values of  $G_R$ . In a qualitative sense, the trends seen in Figure 3-20 for PMMA match the experimentally observed results. An increase in strain rate produces a shear band with higher orientation. For PC, the opposite trend is observed. The model predicts a decrease in orientation with an increase in strain rate. This is clearly contrary to the observed behavior in Figure 3-10. One possible source for the discrepancy between the predicted and experimental behavior of PC is that to estimate the response at high

rates, tests were run at lower temperatures. These temperatures begin to approach the  $\beta$  transition of PC ( $T_\beta = -100^\circ\text{C}$ ),<sup>53</sup> significantly lower than the measured amounts of shear strain. Care should be taken in making comparisons between the predicted behavior and the experimentally produced shear bands. The material properties were obtained during isothermal affine deformation at constant strain rate. In contrast, the shear banding experiments likely violate each of these constraints. The conditions of affine deformation and constant strain rate are clearly not

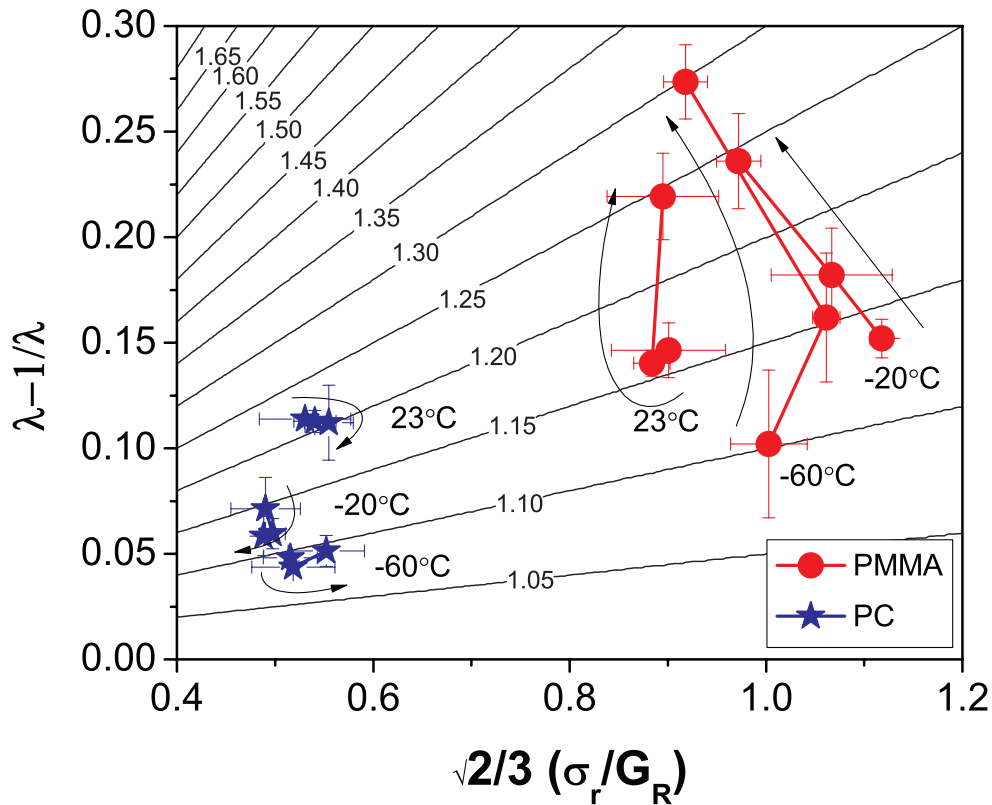


Figure 3-20. Predicted relationship between intrinsic material properties and orientation within a shear band. Contour lines represent steps in  $k_y$ . Arrows indicate direction of increasing strain rate.

met during the shear banding experiments. Since shear banding involves plastic deformation it is reasonable to expect a corresponding increase in temperature especially at the higher rates.<sup>54</sup> If the temperature does increase during the test by a significant amount, the value of  $G_R$  used to predict the response would be artificially high and the model would predict a lower level of orientation.

To see if temperature effects could explain some of the discrepancy between the model and the experimental results, a simplified analysis was performed. The approach taken was to consider if all the mechanical energy put into the sample during shear deformation was converted to heat, would this be enough energy to raise the temperature to get a value of  $G_R$  that would correspond to the observed amount of orientation. The first step in the analysis is to calculate this value of  $G$ ,  $G_{calc}$ . Then by constructing a master curve of  $G_R$  versus  $T$  we can determine the  $\Delta T$  required to achieve  $G_{calc}$ . The mechanical energy put into the sample that could be converted to heat is simply the area under the load-deflection curve less the energy due to elastic loading. The mass of material involved in shear deformation is estimated from the analysis of the images in Figure 3-9. By using the mechanical energy of deformation, the mass of material in the shear band and the specific heat capacity of each material, estimates are made of the temperature increase

$\dot{\gamma}$ ( $\text{min}^{-1}$ )	$\gamma$	$G_R^{\text{calc}}$ (MPa)	Required $\Delta T$ (K)	Mechanical Energy (J)	Mass in Shear Band (mg)	Estimated $\Delta T$ (K)
2.57	0.67	7.6	77	6.09	133	6
21.1	0.69	7.3	78	3.95	150	3
98.5	0.77	6.5	79	8.47	171	6
740	0.80	6.3	80	7.99	155	7

Table 3-3. Required Temperature Increase to Achieve Observed Orientation for PC

during shear deformation (Tables 3-3 and 3-4). These estimates of temperature increase are likely to be overestimates considering Adams and Farris have shown that only 50-80% of the work of deformation is dissipated as heat during cold drawing of PC.<sup>54</sup> Even with these generous estimates, an increase in temperature does not completely account for the discrepancy between predicted and observed orientation.

### Kinematic Limit

To establish a kinematic limit for shear strain in a shear band we will consider the dimensions of the entanglement network. We will

$\dot{\gamma}$ ( $\text{min}^{-1}$ )	$\gamma$	$G_R^{\text{calc}}$ (MPa)	Required $\Delta T$ (K)	Mechanical Energy (J)	Mass in Shear Band (mg)	Estimated $\Delta T$ (K)
0.224	0.71	12	43	3.5	79	7
0.881	0.68	16	37	10.0	78	20
21.0	0.90	21	29	7.3	57	20
50.0	1.01	22	27	4.0	57	11
394	1.17	26	21	0.8	27	5

Table 3-4. Required Temperature Increase to Achieve Observed Orientation for PMMA

assume entanglements behave as permanent crosslinks on the timescale of these experiments. Additional assumptions include constant cross-sectional area and volume. The key parameters describing the entanglement network are,  $M_e$ , the molecular weight between entanglements,  $l_e$ , the chain contour length of a segment of molecular weight  $M_e$  and  $d$ , the entanglement mesh size (Figure 3-21). The extension of a segment to its contour length represents a kinematic limit since further deformation would result in slippage at entanglement points or chain scission. Four entanglement points are deformed under shear until each adjoining chain segment reaches its maximum extension of  $l_e$ . The maximum shear strain,  $\gamma_{max}$ , within the shear band can then be described in terms of the entanglement network parameters,

Using an approach analogous to the one outlined above, Donald and Kramer have made predictions on the maximum extension ratio one

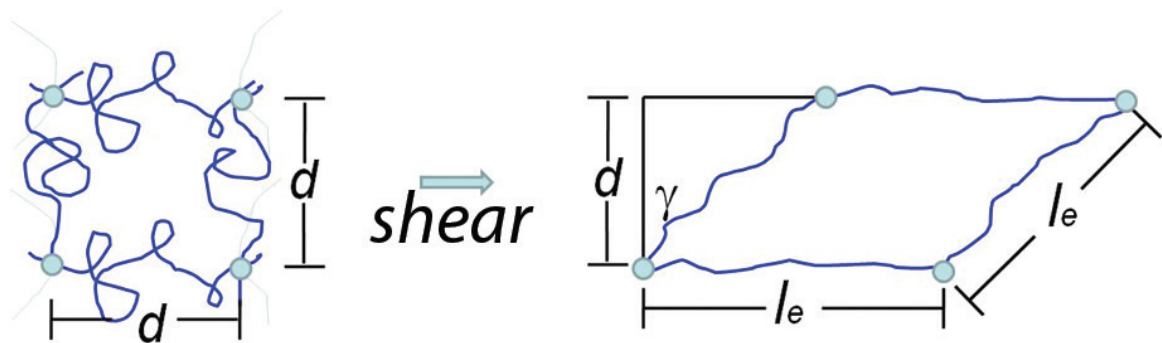


Figure 3-21. Molecular network parameters used to define  $\gamma_{max}$  in shear.

Eq 3-10) 
$$\gamma_{\max} = \cos^{-1} \frac{d}{l_e}$$

might expect in a craze based on dimensions of the entanglement network.<sup>55</sup> Using the values for  $d$  and  $l_e$  from Donald and Kramer this predicts  $\gamma_{\max} = 1.2$  for both PC and PMMA. In Figure 3-10, the shear strain in PMMA increases with rate until Mode II fracture occurs. The maximum shear strain achieved prior to Mode II fracture is just below the predicted kinematic limit of 1.2. It appears that for PMMA, Mode II fracture will occur when the conditions allow the shear band to exceed the kinematic limit. At the highest rates tested, PC still produces stable shear bands and the amount of shear strain is well below the predicted kinematic limit. The highest impact speeds in this study were on the order of 4 m/s. It is interesting to note that Ravi-Chandar et al. have reported Mode II fracture in PC at impact rates exceeding 55 m/s.<sup>42</sup>

PMMA and PC differ greatly in the rate dependence of the intrinsic material properties. PMMA shows greater rate dependence for yield stress, rejuvenated stress, and strain hardening modulus. Some interesting characteristics are revealed when comparing the relative rate dependence of the properties of each material. For example, if one compares the rate dependence of  $\sigma_y$  to that of  $G_R$  in PC, the two display nearly identical trends (Figure 3-22). In stark contrast is the response of

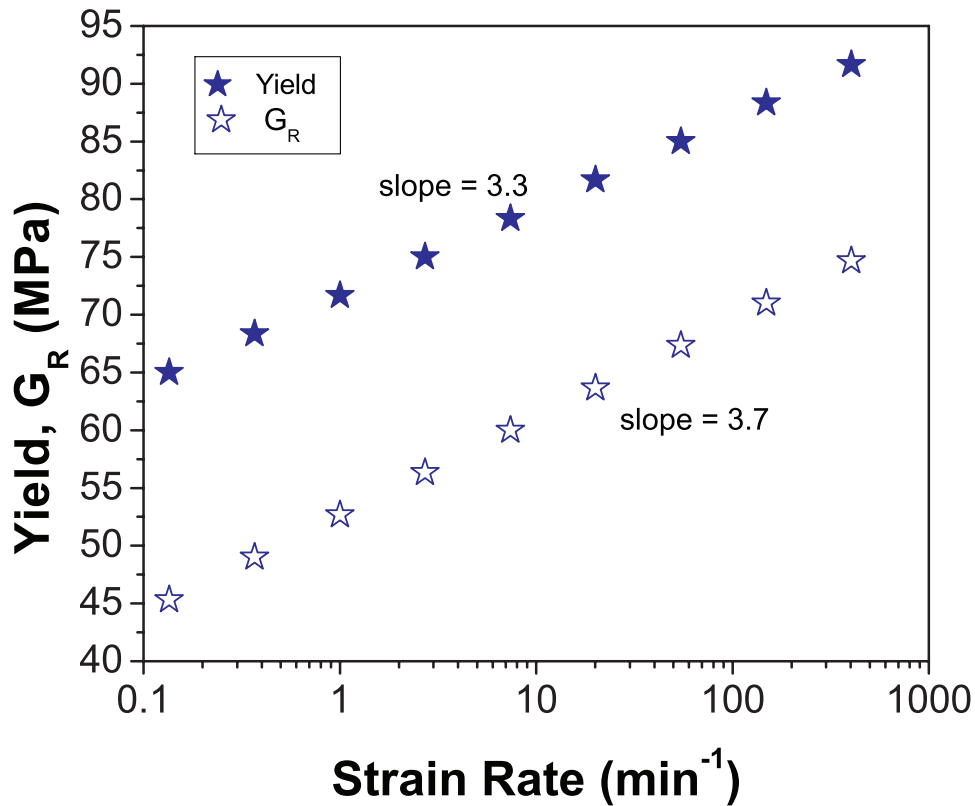


Figure 3-22. Relative rate dependence of yield stress and strain hardening modulus for PC.

PMMA. The rate dependence of  $\sigma_y$  is approximately double the rate dependence of  $G_R$  (Figure 3-23). The strain hardening modulus is a measure of the material's ability to stabilize the localized strain. If a material shows a sufficient increase in  $G_R$  with increases of strain localization, the material will be able to stabilize the shear band and stable propagation will occur as seen in PC. However, if the amount of strain localization increases at a greater rate than  $G_R$ , there will be a rate above which the material is unable to stabilize the shear band and

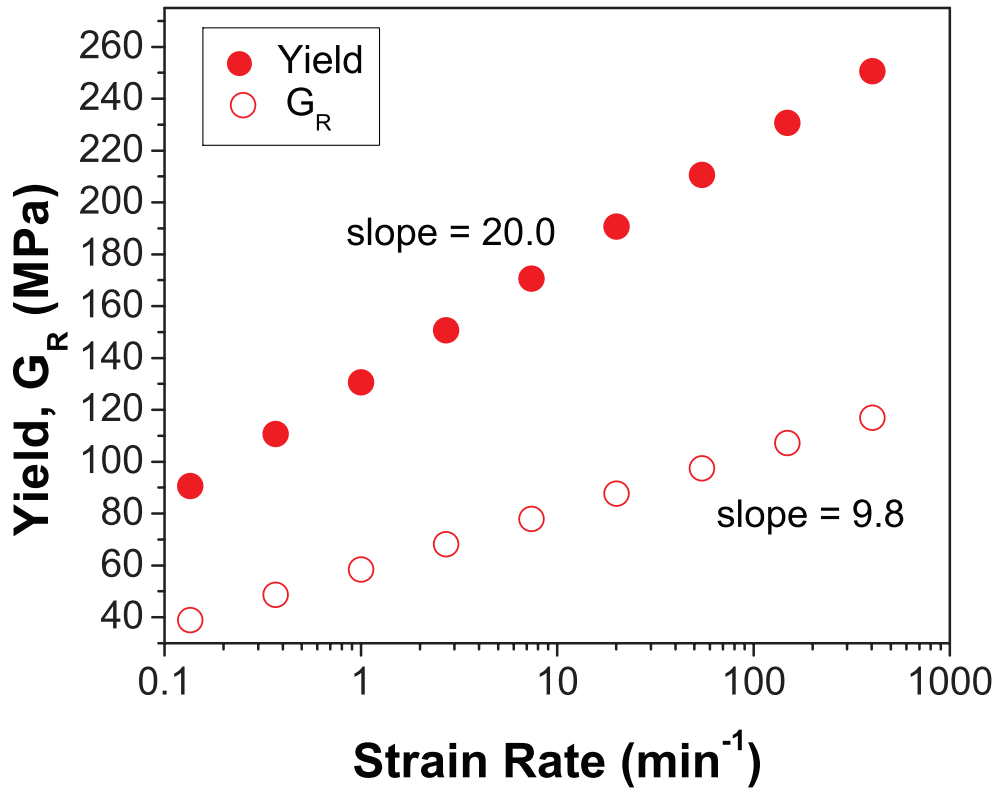


Figure 3-23. Relative rate dependence of yield stress and strain hardening modulus for PMMA.

fracture will occur, as seen in PMMA. This behavior can be captured by plotting the relative rate dependence of the ratio of the post yield stress drop (*PYSD*), to  $G_R$  (Figure 3-24). An increase in  $PYSD/G_R$  represents a greater propensity for unstable shear band growth and Mode II fracture. These trends are further supported by the finite element analysis of shear banding by Wu and van der Giessen.<sup>56</sup>

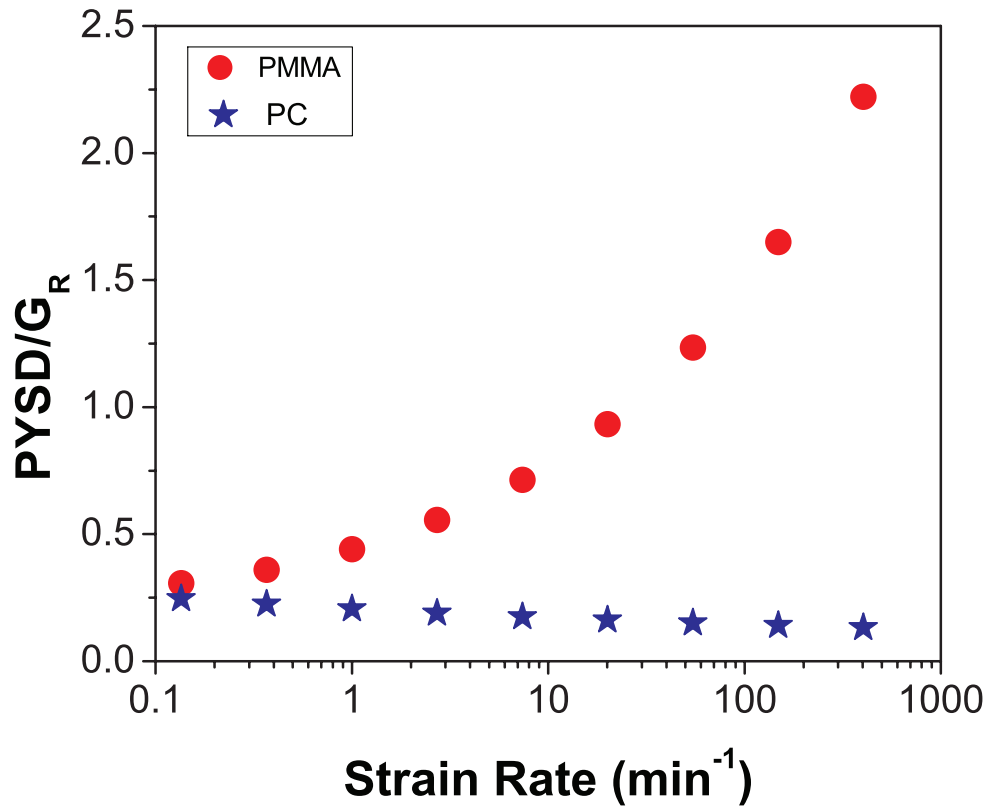


Figure 3-24. Rate dependence of the post yield stress drop (PYSD) normalized by strain hardening modulus ( $G_R$ ).

### Conclusions

The effect of rate on shear band formation was evaluated for PMMA and PC. In both polymers, the maximum shear strain in the shear band increases with rate. Mode II fracture is observed in PMMA above impact rates of 500 mm/min. The Mode II fracture toughness of PMMA is approximately seven times the Mode I fracture toughness. This suggests that if one is able to suppress Mode I fracture, whether through a superposed compressive stress or other means, the impact resistance of

the material will be drastically increased. Mode II fracture was not observed in PC for the range of rates tested. The condition for shear band stability based on intrinsic material properties was developed. This theory agrees qualitatively with the shear band response of PMMA but underestimates the amount of orientation. The kinematic limit of shear strain was determined based on dimensions of the entanglement network. Mode II fracture occurs at the kinematic limit in PMMA.

## References

34. Hsieh, A. J., DeSchepper, D., Moy, P., Dehmer, P. G. & Song, J. W. The Effects of PMMA on Ballistic Impact Performance of Hybrid Hard/Ductile All-Plastic- and Glass-Plastic-Based Composites. *Army Research Laboratories* (2004).
35. Archer, J. S. & Lesser, A. J. Impact resistant polymeric glasses using compressive pre-stress. *J. Appl. Polym. Sci.* **114**, 3704-3715 (2009).
36. Ayatollahi, M. R., Aliha, M. R. M. & Hassani, M. M. Mixed mode brittle fracture in PMMA--An experimental study using SCB specimens. *Materials Science and Engineering: A* **417**, 348-356 (2006).
37. Ayatollahi, M. R. & Aliha, M. R. M. On determination of mode II fracture toughness using semi-circular bend specimen. *International Journal of Solids and Structures* **43**, 5217-5227 (2006).

38. Erdogan, F. & Sih, G. C. On the crack extension in plates under plane loading and transverse shear. *Journal of Basic Engineering* **85**, 519-525 (1963).
39. Melin, S. When does a crack grow under mode II conditions? *Int J Fract* **30**, 103-114-114
40. Broberg, K. B. On Crack Paths. *Engineering Fracture Mechanics* **28**, 663-679 (1987).
41. Kalthoff, J. F. Shadow optical analysis of dynamic fracture. *Optical Engineering* **27**, 835-840 (1988).
42. Ravi-Chandar, K., Lu, J., Yang, B. & Zhu, Z. Failure mode transitions in polymers under high strain rate loading. *Int J Fract* **101**, 33-72 (2000).
43. Rosenfield, A. R. & Kanninen, M. F. The fracture mechanics of glassy polymers. *Journal of Macromolecular Science, Part B: Physics* **7**, 609-631 (1973).
44. Johnson, F. A. & Radon, J. C. Fracture Process and Molecular Kinetics of Pmma. *Journal of Polymer Science Part a-Polymer Chemistry* **11**, 1995-2020 (1973).
45. Beardmore, P. & Fellers, J. Characteristic fracture features of polymethyl methacrylate. *Materials Science and Engineering* **5**, 120-125
46. Bhattacharjee, D. & Knott, J. F. Effect of mixed mode I and II loading on the fracture surface of polymethyl methacrylate (PMMA). *Int J Fract* **72**, 359-381 (1995).
47. Ward, I. M. & Sweeney, J. *An Introduction to the Mechanical Properties of Solid Polymers*. (John Wiley & Sons: West Sussex 1993).

48. Lee, S. M. Mode II Interlaminar Crack Growth Process in Polymer Matrix Composites. *Journal of Reinforced Plastics and Composites* **18**, 1254-1266 (1999).
49. Kwon, H. J. & Jar, P. Y. B. Fracture toughness of polymers in shear mode. *Polymer* **46**, 12480-12492 (2005).
50. Haward, R. N. The application of a simplified model for the stress-strain curves of polymers. *Polymer* **28**, 1485-1488 (1987).
51. van Melick, H. G. H., Govaert, L. E. & Meijer, H. E. H. Localisation phenomena in glassy polymers: influence of thermal and mechanical history. *Polymer* **44**, 3579-3591 (2003).
52. Boyce, M. C. & Arruda, E. M. An Experimental and Analytical Investigation of the Large Strain Compressive and Tensile Response of Glassy-Polymers. *Polymer Engineering and Science* **30**, 1288-1298 (1990).
53. Monnerie, L., Halary, J. & Kausch, H.-H. Deformation, Yield and Fracture of Amorphous Polymers: Relation to the Secondary Transitions. *Intrinsic Molecular Mobility and Toughness of Polymers I* 215-372 (2005).doi:10.1007/b136957
54. Adams, G. W. & Farris, R. J. Latent Energy of Deformation of Bisphenol-a Polycarbonate. *J. Polym. Sci. B Polym. Phys.* **26**, 433-445 (1988).
55. Donald, A. M. & Kramer, E. J. Effect of Molecular Entanglements on Craze Microstructure in Glassy-Polymers. *J. Polym. Sci. B Polym. Phys.* **20**, 899-909 (1982).
56. Wu, P. D. & van der Giessen, E. Analysis of shear band propagation in amorphous glassy polymers. *International Journal of Solids and Structures* **31**, 1493-1517 (1994).



## CHAPTER 4

### 4. RATE SENSITIVITY OF STRAIN LOCALIZATION IN GLASSY POLYMERS

#### Abstract

Shear banding experiments are carried out on model glassy polymers (PMMA and PC) displaying different levels of strain localization and strain rate sensitivity. The deformation response is interpreted through the characterization of the “intrinsic material properties” as measured by compression tests. The relatively high rate sensitivity of PMMA deformed at room temperature is related to the proximity of the beta transition to the test temperature. This is also shown in corollary experiments on PC where deformation near the beta transition is accompanied by an increase in rate sensitivity. Physical aging results in a more narrow alpha transition and is shown to increase strain localization and decrease rate sensitivity at low strain rates.

#### Introduction

The large scale deformation response of glassy polymers is commonly described within the framework of rheologically simple materials. In this case, the yield response is dictated by a single relaxation mode, the alpha process. Depending on the material and the range of rates and temperatures, this approach can describe a significant

portion of the deformation response.<sup>57</sup> PC is a good example of this. The Eyring flow process can be used to describe yielding in PC from -70 to 150° C.<sup>58,59</sup> However, there are some temperature (or strain rate) ranges that fail to be captured with a single relaxation process.<sup>60-63</sup> In PC, for example, the dependence of yield stress on the log of strain rate changes slope below -70° C as molecular motions associated with the  $\beta$  transition begin to be excluded from the process.<sup>59</sup> Below -70° C the dependence of yield stress on temperature increases. Additionally, the post yield response can be affected by secondary processes in rheologically complex materials.<sup>64-66</sup> For a rheologically simple material the post yield stress drop (PYSD) should have no dependence on strain rate. The previous chapter showed that for a reasonable range of strain rates and temperatures, the PYSD is not constant in PMMA and therefore cannot be modeled with a single relaxation process at these rates and temperatures. This chapter will highlight these effects on the rate dependence of strain localization during large scale shear deformation.

One significant difference between PMMA and PC is the beta relaxation temperature. The beta transition of PC, as measured by dynamic mechanical analysis at 1 Hz, is near -100° C while the beta transition of PMMA is near 10° C.<sup>67</sup> Increases in test frequency (strain rate) will result in a shift of the relaxation spectrum to higher

temperatures. At room temperature (23° C), the entire range of motions associated with the beta transition in PC are thermally activated. This can be seen in Figure 4-1 which shows the high temperature onset of the beta peak for PC beginning at approximately 0° C. This low beta transition has been associated with the toughness of PC and its ability to dissipate energy through yielding rather than brittle fracture.<sup>67</sup> When frequency is increased by an order of magnitude (1 - 10 Hz) both the beta and alpha transitions shift to higher temperatures. Since the beta

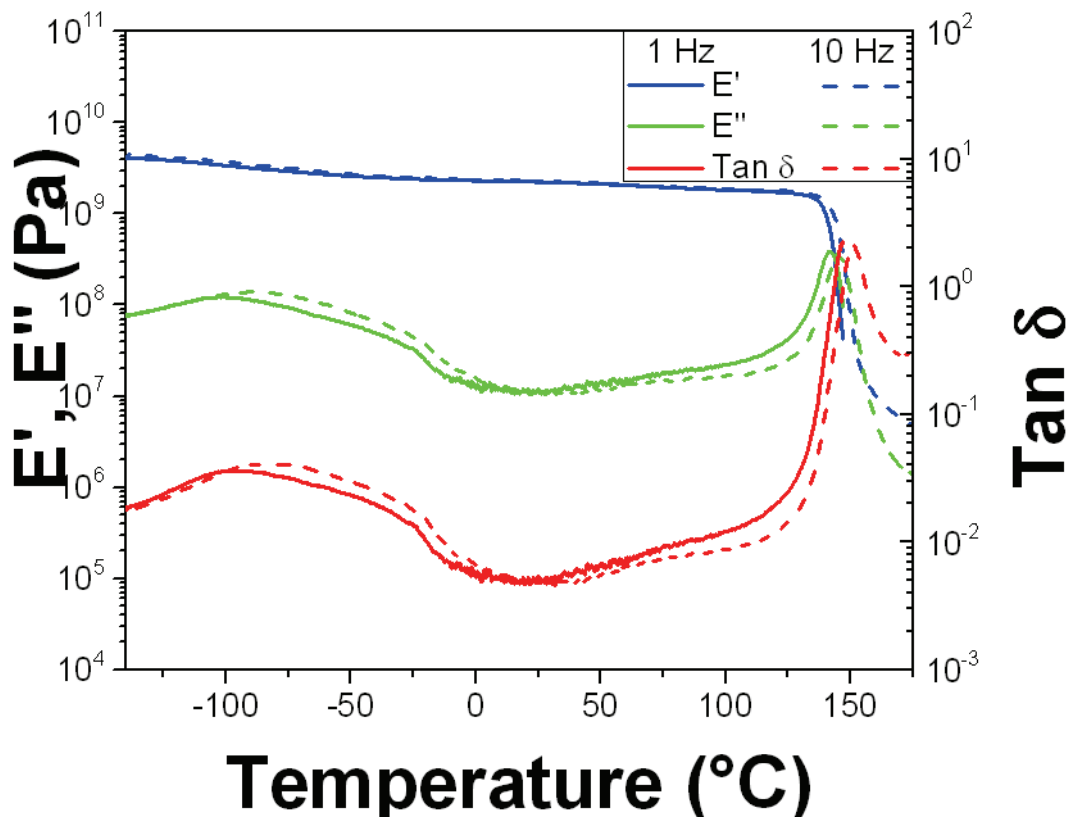


Figure 4-1. Dynamic mechanical analysis on PC at 1 Hz and 10 Hz. The high toughness and ductility in PC is attributed to the low beta transition temperature.

transition is at such a low temperature, the viscoelastic response at room temperature is essentially the same at both frequencies. To the extent that the linear viscoelastic response dictates large scale deformation, very little rate sensitivity is expected in PC at room temperature.

At room temperature and 1 Hz oscillation, PMMA has just over half of the beta transition relaxation spectrum thermally activated (Figure 4-2). When frequency is increased to 10 Hz, both the alpha and beta transitions shift to higher temperatures. The shift of the beta transition

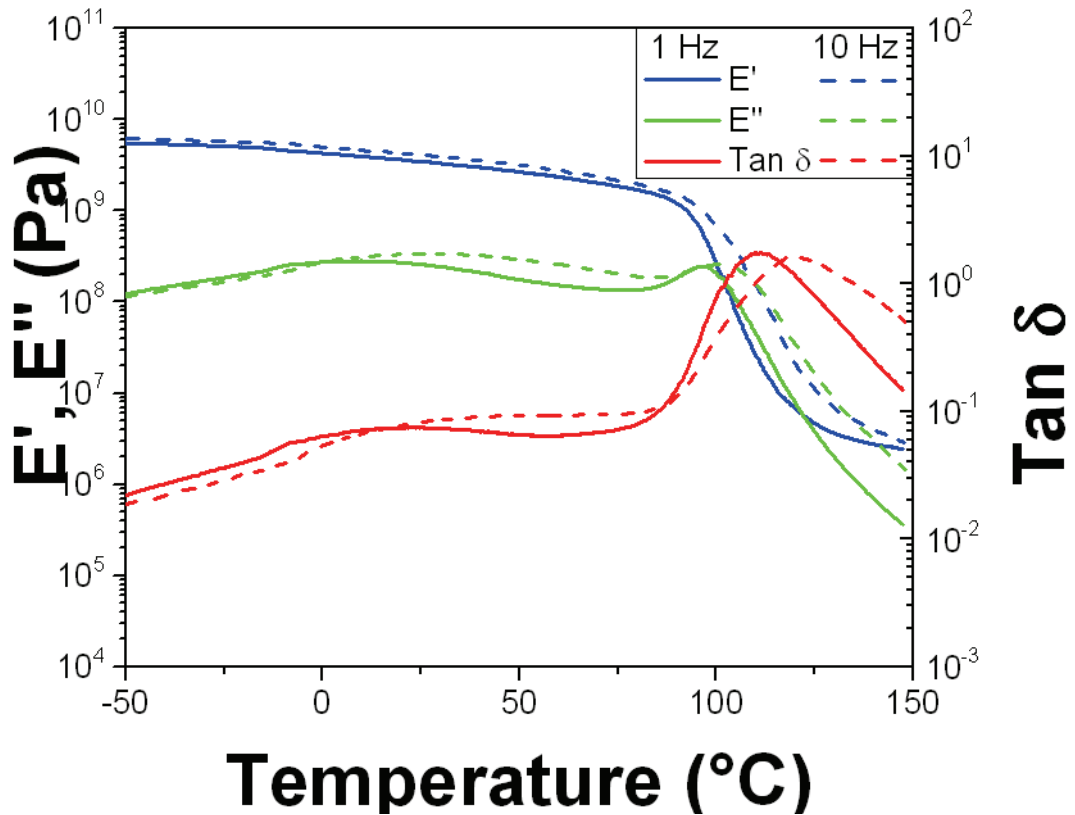


Figure 4-2. Dynamic mechanical analysis of PMMA 930k at 1 Hz and 10 Hz.

is greater in PMMA (~30 C) than in PC (~10 C) for the same change in frequency. This larger shift in combination with the proximity of the beta transition temperature to room temperature results in a dramatically different viscoelastic response at the higher frequency. At 23° C and 10 Hz, less than half of the beta relaxation spectrum is thermally activated. This observation and its effect on shear deformation and strain localization will be explored in this chapter.

An interesting phenomenon observed in glassy polymers is the evolution of structure with time referred to as physical aging. During this process the material densifies as local energetic minima are reached.<sup>68</sup> Physically aged polymers display a change in a number of properties. Of particular interest here is the effect on yield.<sup>69</sup> When looking at the true stress - true strain response, aged polymer glasses show an increase in yield stress followed by strain softening.<sup>65,70</sup> After softening, the response is very similar to the unaged polymer as the material reaches the strain hardening regime. The increase in yield is attributed to the 'rough energy landscape' developed during packing.<sup>71</sup> Higher amounts of energy are required to reach the yield instability and incite flow. Once the strain level is high enough to overcome local energy barriers, the effects of packing are essentially erased. Accordingly, the stress drops to the level seen in the unaged polymer. This return to unaged behavior is the

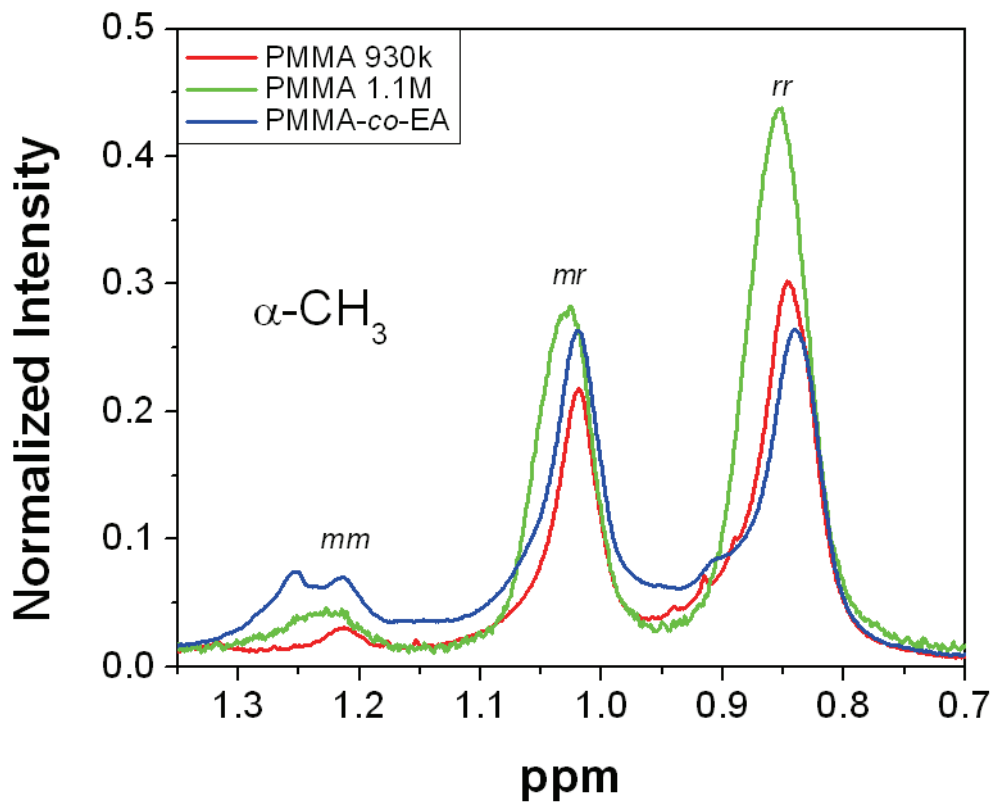


Figure 4-3. Tacticity measurements by NMR.

origin of the term “rejuvenated stress.” This simplistic interpretation of rejuvenation based on work by Struik has been challenged by several authors.<sup>72-74</sup> Through calorimetry and computer simulations it has been shown that mechanical deformation does not erase thermal history but rather brings the material to a new equilibrium.<sup>71,75,76</sup> When the yield stress is increased through aging, the subsequent post-yield strain softening is accompanied by increased strain localization. If the strain hardening modulus is high enough, the localized deformation is stabilized and the polymer will deform in a ductile fashion, otherwise

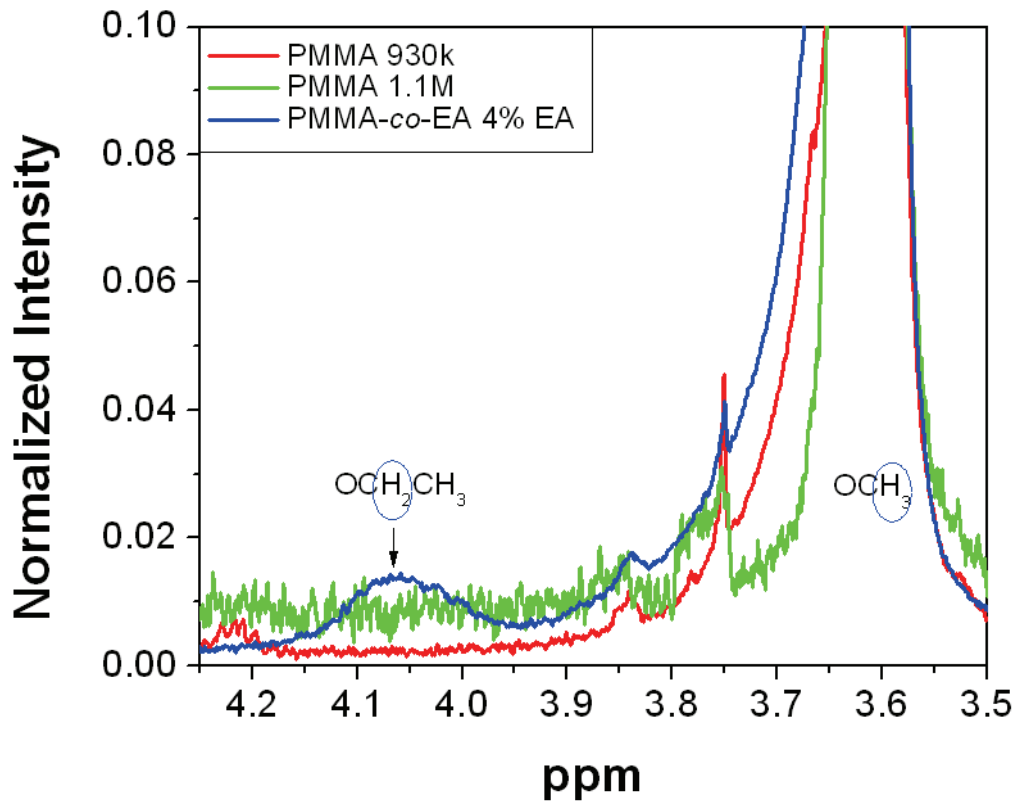


Figure 4-4. Copolymer composition determined by NMR.

strain localization will result in brittle fracture. This process is nicely illustrated by Govaert's work on "mechanical rejuvenation."<sup>77-79</sup> Brittle polystyrene can be made ductile by passing it through calendaring rolls. Taking the material beyond yield mechanically erases physical aging removing its ability to strain localize. Immediately after mechanical rejuvenation, polystyrene can undergo large strains prior to failure. However, as the glass ages over a matter of days, the yield stress and strain softening increase to the point where the brittle response is

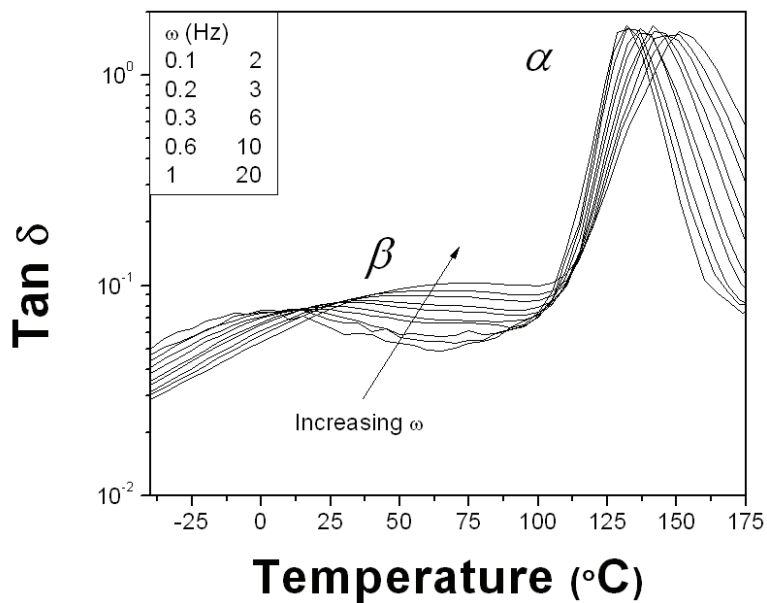


Figure 4-5. PMMA 930 kg/mol tan  $\delta$  at different frequencies as a function of temperature.

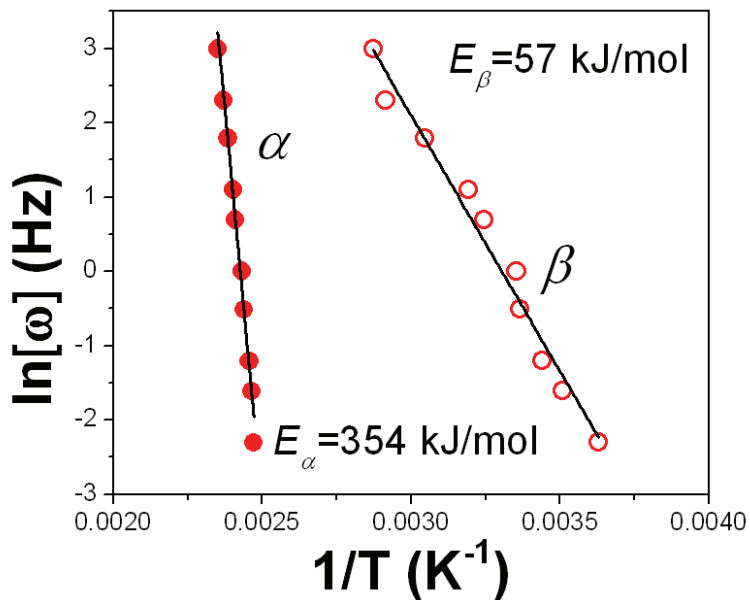


Figure 4-6. PMMA 930 kg/mol activation energies for alpha and beta transitions.

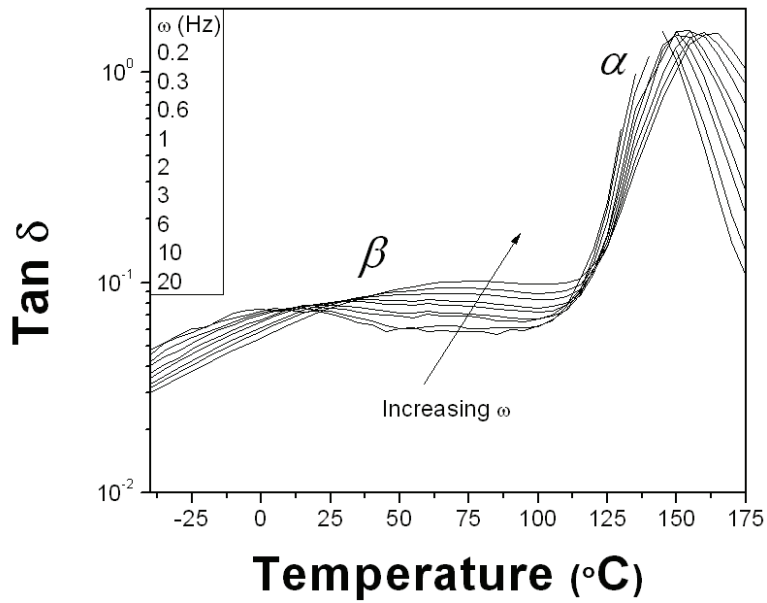


Figure 4-7. PMMA 1,100 kg/mol  $\tan \delta$  at different frequencies as a function of temperature.

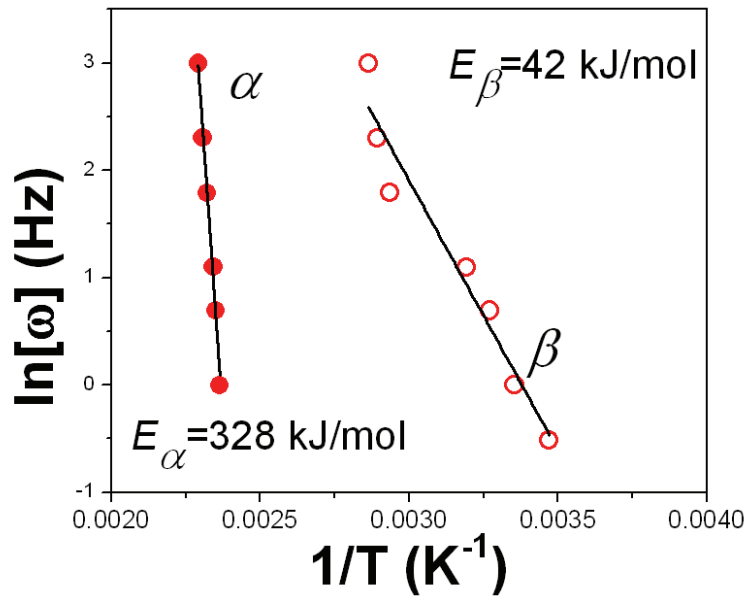


Figure 4-8. PMMA 1,100 kg/mol activation energies for alpha and beta transitions.

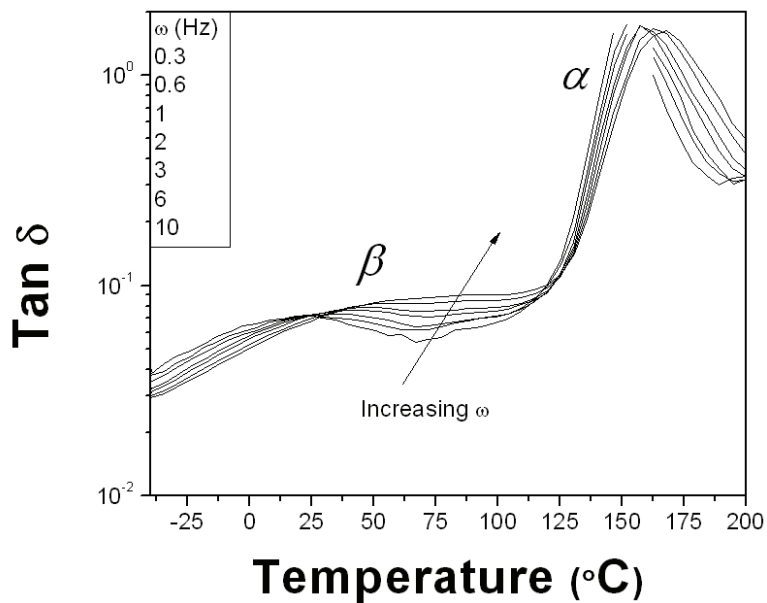


Figure 4-9. PMMA-co-EA  $\tan \delta$  at different frequencies as a function of temperature.

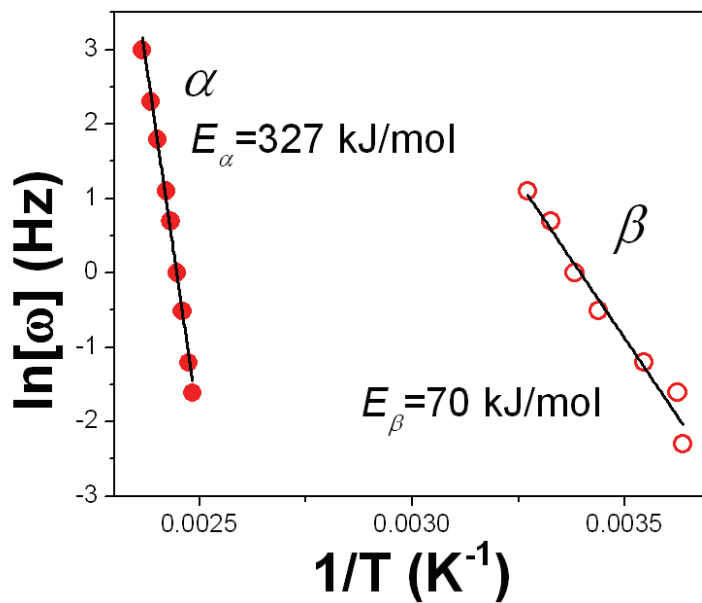


Figure 4-10. PMMA-co-EA activation energies for alpha and beta transitions.

restored.<sup>80</sup> Physical aging and its effect on strain localization will be investigated in this chapter.

Table 4-1. Ratio of isotactic meso-meso (*mm*), atactic meso-racemo (*mr*) and syndiotactic racemo-racemo (*rr*) triads from NMR.

Linear Regression - Relaxation Time			
<i>Model</i>		<i>Factors</i>	<i>P-values</i>
P-value	0.02	Intercept	1.6E-05
Adjusted R <sup>2</sup>	0.70	Stress State	0.01
		MW	0.47

## Experimental

### Materials

The concern of this chapter is primarily the extension of the experimental approach used in the previous chapter to a broader range of molecular architectures with the aim of relating the various architectures to the process of shear band formation. The materials to be compared include: two PMMA homopolymers with molecular weights of 930 and 1,100 kg/mol. Molecular weight was determined by GPC using THF as a solvent and polystyrene standards. A random copolymer of methyl methacrylate and ethyl acrylate with molecular weight of 160 kg/mol is also included. Small amounts of comonomer are typically incorporated into PMMA to increase its thermal stability therefore

enhancing its ability to be thermally processed. The comonomer increases thermal stability by limiting the unzipping mechanism that contributes to the thermal degradation of the homopolymer.<sup>81</sup> The tacticity and copolymer composition of the acrylics were quantified by NMR (Figures 4-3 and 4-4). A homopolymer of PC finishes out the list of materials.

In addition to chemical definitions of architecture, the structure of the materials was altered through physical aging. The 930 kg/mol PMMA homopolymer was aged at  $T_g - 15^\circ \text{C}$  for 85 hours and PC was aged at  $T_g - 25^\circ \text{C}$  for 85 hours, under nitrogen environment. The sheets of material were placed on glass plates to maintain their planarity during the heat treatment. After the aging time was complete, the oven was turned off and allowed to come to room temperature slowly over several hours.

### Compression Testing

Sample preparation and testing was done in accordance to the procedures outlined in the previous chapter. Cylindrical samples with height = diameter = 4.35 mm were deformed at constant strain rates of: 0.01, 0.032, 0.1, 0.32 and  $1 \text{ min}^{-1}$ . Testing was done at  $23^\circ$  and  $80^\circ \text{C}$ . Temperature was controlled with an oven.

## Shear Deformation

Again, methods used here are described in the previous chapter. Machined rectangular samples were pre-cracked at 45° to the loading axis and loaded in compression at constant crosshead displacement rates in an Instron 5800. The local maximum shear strain rate and maximum shear strain in the shear band were determined from optical strain measurements taken from digital images of the deforming sample. The raw data from the experiments can be found in the Appendix.

## Results and Discussion

Use is made of the formalism established in the previous chapter on relating the material properties of yield stress, rejuvenated stress and strain hardening modulus, as measured from uniaxial compression, to

Eq (4-1) 
$$\frac{\sqrt{2}\sigma_y}{3G_R} = \frac{\lambda - \lambda^{-1}}{1 - k_y^{-1}}$$

strain localization in a shear band.<sup>64</sup>

There are several discussion points that arise from the comparison of the predicted and measured levels of shear strain and their dependence on strain rate (Figures 4-11 and 4-12). First, in general there is fair qualitative agreement of the trends seen in the predicted and

measured values. The homopolymers both show similar rate dependencies in the predicted and measured values. The rate dependency can be envisaged by considering the slope of the shear strain vs strain rate data (Figure 4-12). Additionally there is a relative offset between the two materials. The lower molecular weight PMMA homopolymer has predicted and measured levels of strain localization that are higher than the higher molecular weight homopolymer. Whether

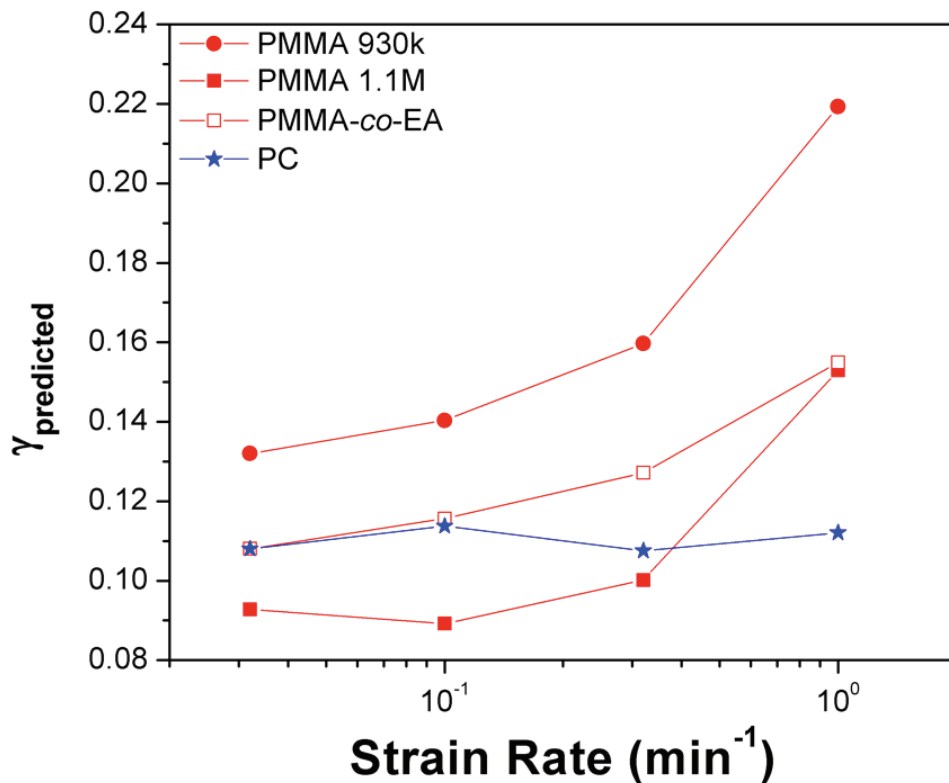


Figure 4-11. Predicted levels of shear strain based on values of  $\sigma_y$ ,  $k_y$  and  $G_R$  as measured by compression tests. The two PMMA homopolymers have very similar rate dependencies. PMMA-co-EA has less rate dependence at the highest strain rates and levels of localization intermediate to the homopolymers. All at 23° C.

or not this behavior can be attributed to the molecular weight will be discussed in the section on Physical Aging. Comparing the copolymer to these materials, the former shows decreased rate sensitivity. The difference is highest at the higher strain rates. The predicted level of localization is intermediate between the two homopolymers. This rings true in the measured quantities only in the intermediate levels of strain

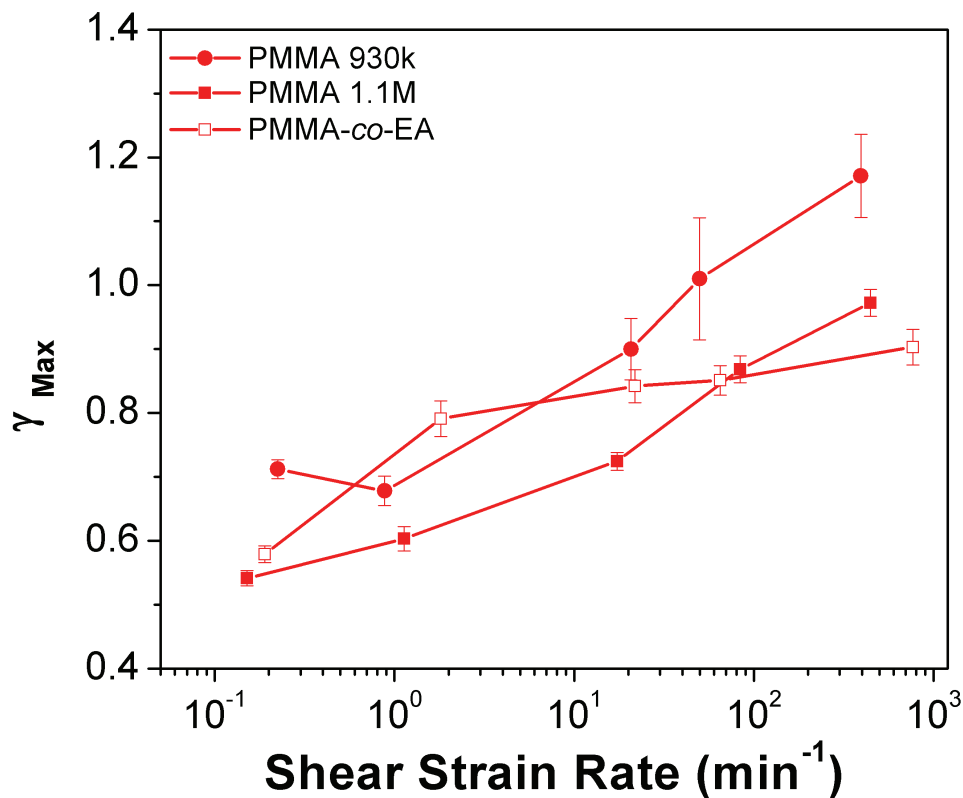


Figure 4-12. Rate dependence of strain localization in shear bands for acrylic polymers. The two PMMA homopolymers have very similar rate dependencies. PMMA-co-EA has less rate dependence. All at 23° C.

rate. For PC, the predicted rate sensitivity is essentially zero, while the measured values show a non-zero rate sensitivity that is less than PMMA.

### Test Temperature and the Beta Relaxation

When PC is deformed at room temperature it is well above its beta transition. Under these conditions, very little rate sensitivity is observed. PMMA was also tested above its beta transition (80° C) to see what effect this would have on rate sensitivity. From the predicted values, one would expect the level of strain localization to decrease with increases in strain

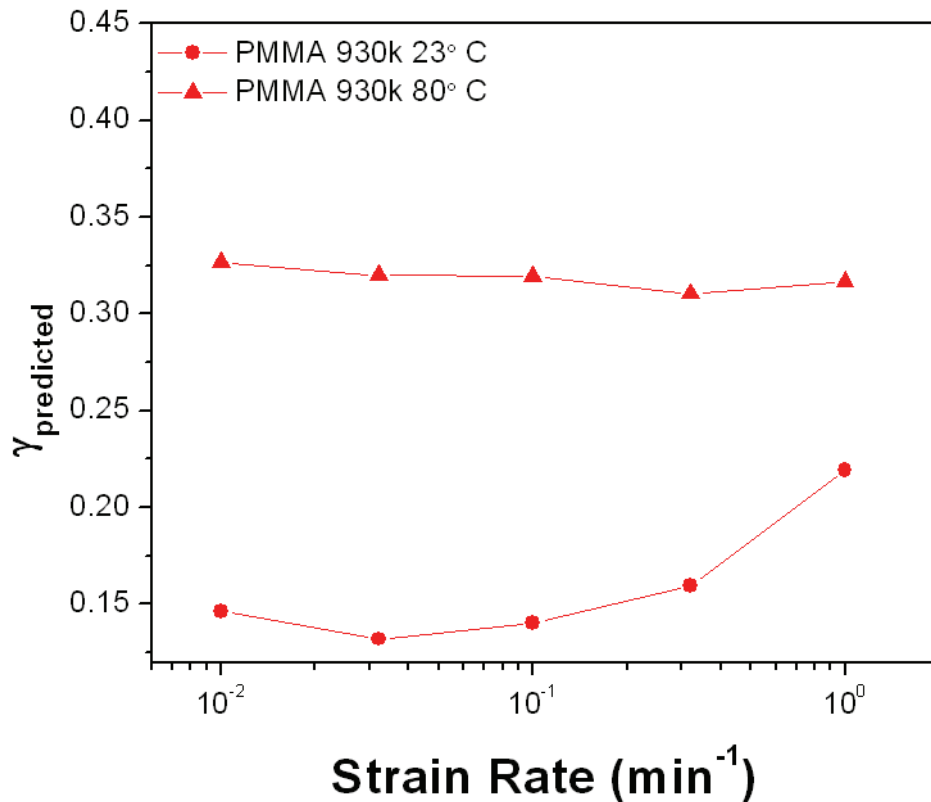


Figure 4-13. Predicted strain localization in PMMA 930k at 80° C (above  $T_{\beta}$ ).

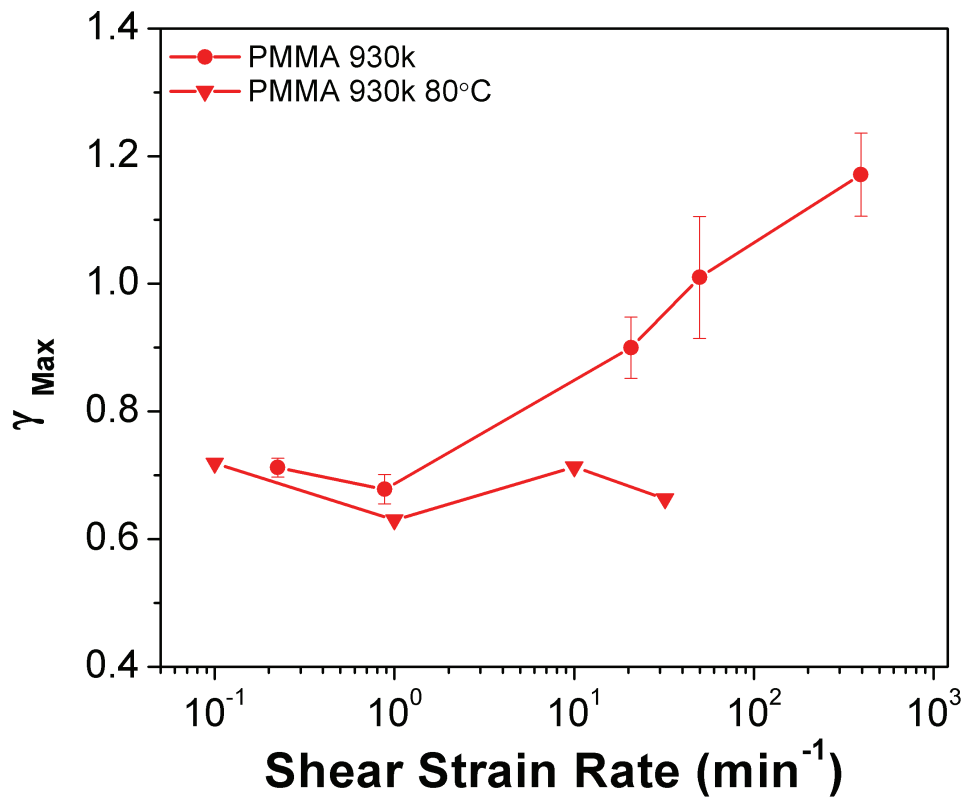


Figure 4-14. Strain localization in shear bands formed in PMMA at 80 °C (above  $T_{\beta}$ ). Rate sensitivity is decreased above the beta transition temperature.

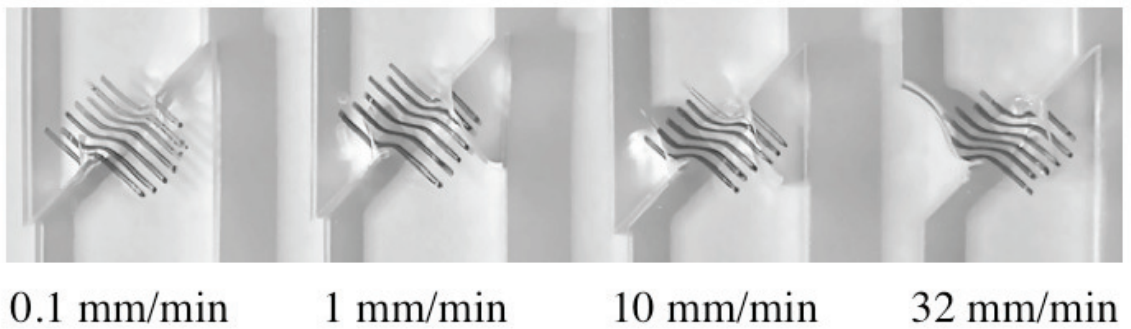


Figure 4-15. Shear bands formed in PMMA at 80° C.

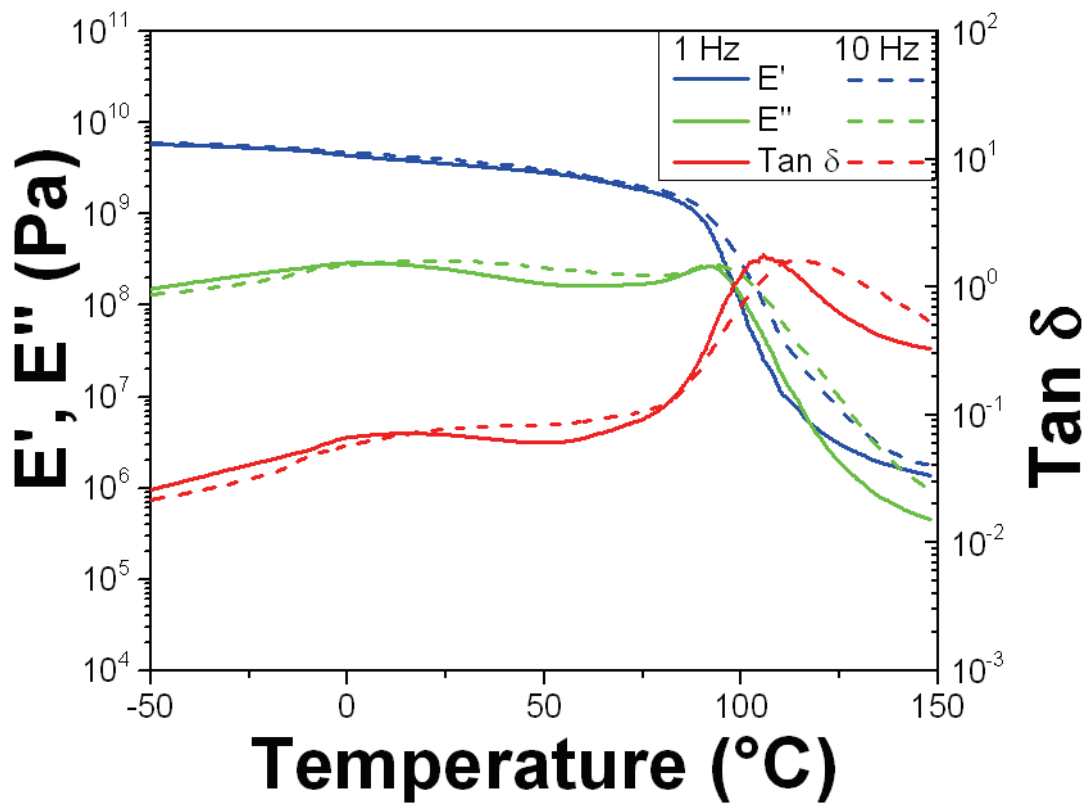


Figure 4-16. Dynamic mechanical analysis of PMMA-co-EA at 1 and 10 Hz.

rate (Figure 4-13). Also, significantly higher levels of localization are predicted. The measured values show very little change in localization with strain rate and levels of localization that are comparable to low strain rate deformation at 23° C (Figure 4-14).

The beta relaxation temperature of PMMA-co-EA is approximately 10° C lower than PMMA 930k homopolymer at 1 Hz (Figure 4-16). Room temperature deformation of this copolymer is less rate sensitive than the

homopolymer. Here again is another example of deformation above the beta relaxation leading to decreased rate sensitivity.

PC was tested at  $-190^{\circ}\text{C}$  (submerged in liquid  $\text{N}_2$ ) to investigate how rate sensitivity and strain localization change at temperatures near the beta transition. When PMMA is deformed near its beta transition it is highly rate sensitive. If high rate sensitivity at the beta transition typifies deformation of glassy polymers, one might expect PC to display higher rate sensitivity when deformed near its beta transition. The results are shown in Figures 4-17 and 4-18. The rate sensitivity of PC is significantly higher when deformation takes place below the beta transition. Additionally, the level of localization is decreased at these lower temperatures. Attempts were made to perform compression tests on PC at  $-190^{\circ}\text{C}$ , but the samples fractured after strain softening.

These results suggest that the proximity of the test temperature to the beta relaxation can have a significant effect on the rate sensitivity of glassy polymers. This observation is consistent with the time - temperature correspondence behavior of polymers. Near the beta relaxation, the linear viscoelastic functions ( $E'$ ,  $E''$  and  $\tan \delta$ ) have an increased dependence on temperature so one would expect a corresponding increase in rate dependence assuming that the transition

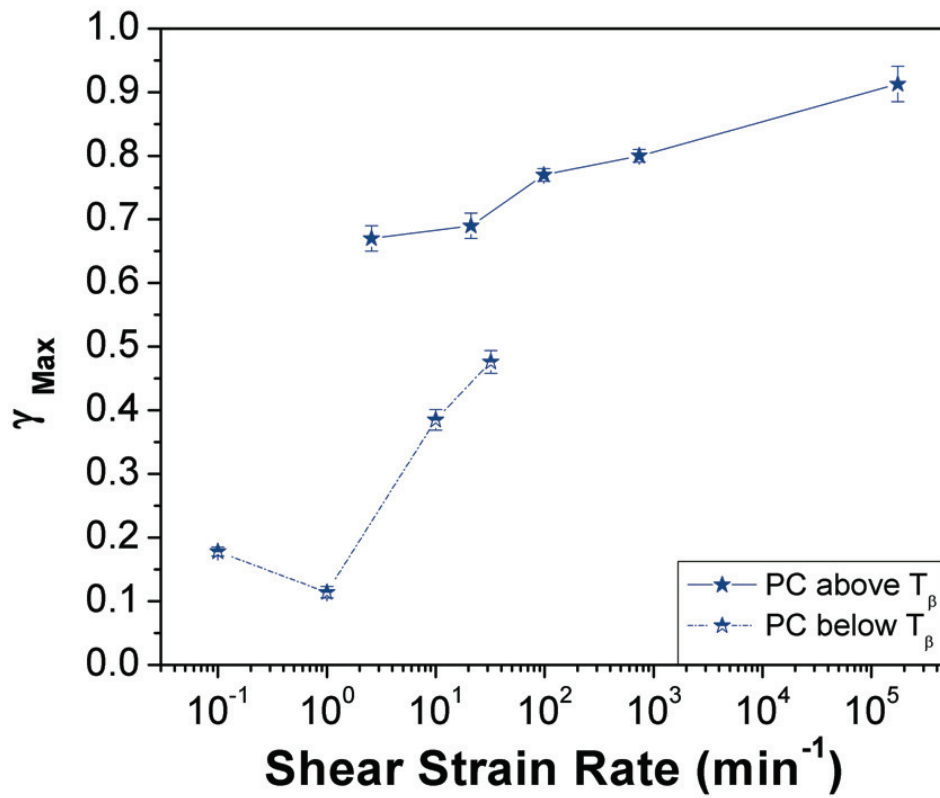


Figure 4-17. Strain localization in shear bands formed in PC at -190° C (below  $T_{\beta}$ ). Rate sensitivity is increased below  $\beta$  transition temperature.

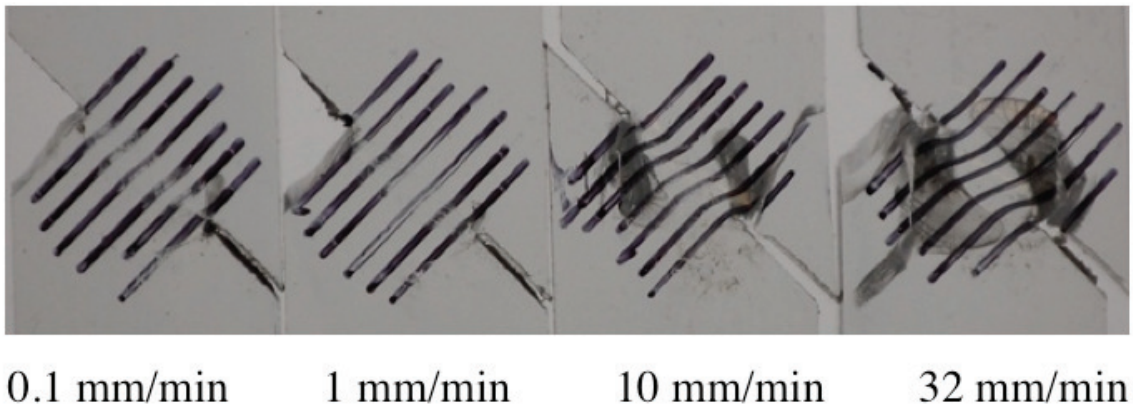


Figure 4-18. Shear bands formed in PC at -190° C.

significantly affects deformation. Strain localization should be strongly correlated with molecular mobility. Higher degrees of mobility allow the polymer to delocalize deformation. When the timescale of deformation is less than the timescale of a given relaxation mode, the contribution of that mode to the delocalization process will be limited. This effect is seen in significant change in localization behavior of PMMA at its beta transition compared to deformation above the transition. At room temperature, increases in rate exclude a significant portion of the relaxation spectrum. Consequently, strain localization is increased. At 80° C, there is enough thermal mobility so that the range of strain rates tested do not exclude enough of the relaxation spectrum to significantly alter the level of strain localization. This effect of the beta transition and test temperature is also seen in PMMA-*co*-EA. Room temperature deformation of this copolymer is about 23° C higher than the beta relaxation temperature so that a greater proportion of the relaxation spectrum is thermally activated. Additionally, the copolymer has a broader beta relaxation than the homopolymer. This is primarily seen on the low temperature side of the transition. The lower beta relaxation temperature and the broader distribution both contribute to increased mobility and decreased rate sensitivity in PMMA-*co*-EA.

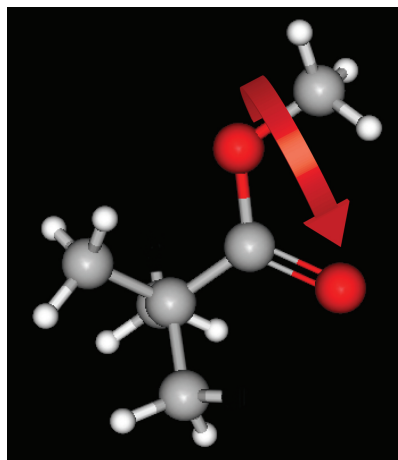


Figure 4-19. A significant contribution to the  $\beta$  relaxation in PMMA is a  $180^\circ$  flip of the pendant group. The flip is coupled to main chain mobility.

Some further insight into these observations might be gained by looking into the molecular origin of the beta relaxations in PMMA and PC. Through the use of multidimensional NMR, Spiess and coworkers have shown that the beta relaxation in PMMA originates from a  $180^\circ$  flip of the pendant group about the C-COO bond (Figure 4-19).<sup>82</sup> An interesting aspect of this process is the coupling of the side group flip to main chain motion. These coupled dynamics are attributed to the asymmetry of the pendant group. After the flip, the pendant group finds itself in a non-identical environment and the main chain adjusts accordingly. These coupled dynamics are likely the cause behind the relative proximity and overlap of the alpha and beta transitions observed in PMMA (Figure 4-2). PC on the other hand owes its beta transition to the  $180^\circ$  flip of phenyl rings (Figure 4-20).<sup>83,84</sup> The structure of the molecule before and after

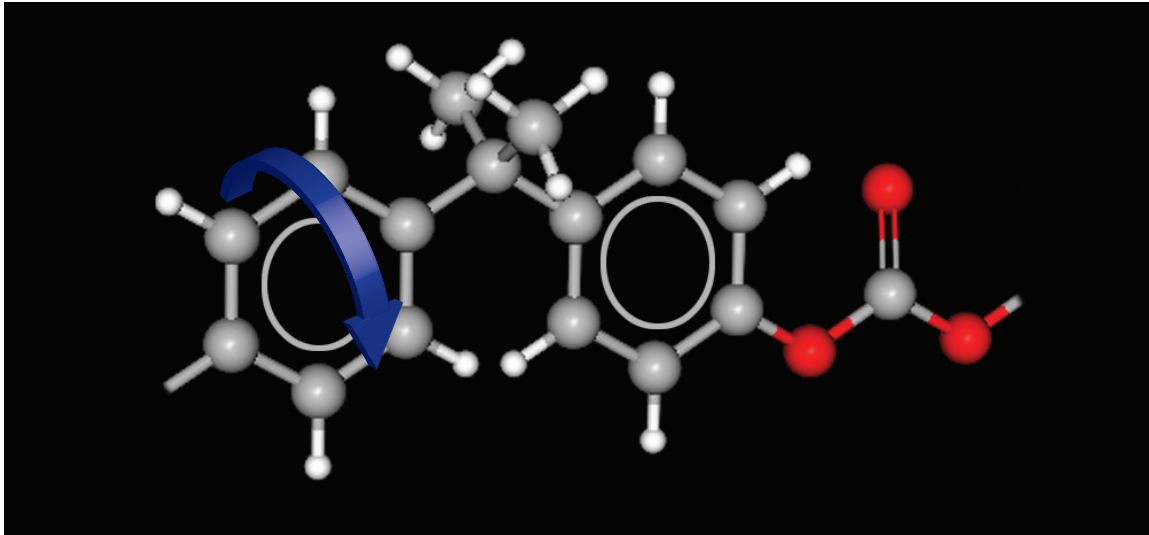


Figure 4-20. A significant contribution to the  $\beta$  relaxation in PC is a  $180^\circ$  flip of phenyl rings in the main chain.

the flip is identical. In this case, the similarity of the arrangement of atoms before and after leads to no change in the local environment of the phenyl ring and accordingly, conformational changes in the backbone are not coupled with the flip. Further evidence for the lack of coupling between the alpha and beta processes in PC is shown in the large temperature difference between the two transitions (Figure 4-1).

In order to more fully describe large scale (post yield) deformation in glassy polymers it is sometimes necessary to incorporate multiple relaxatory modes into the description. One phenomenon that requires such treatment is rate dependence in the post yield stress drop. Goveart and coworkers have been able to successfully model this behavior by the use of two separate viscosity functions in the constitutive equation.<sup>66</sup>

One describes the alpha process while the other describes the material behavior when both alpha and beta processes are active. The effect of the beta process on shear band formation was clearly demonstrated in the previous section. For deformation at room temperature in PMMA, the beta relaxation is at the test temperature and the material is in the  $\alpha+\beta$  regime. When the test temperature is increased above the beta transition the material is in the  $\alpha$  regime as shown by the decrease in rate sensitivity.

### Physical Aging

The characteristic mechanical response to physical aging is an increase in the yield stress. If yield stress is increased leaving the post-yield behavior unaffected, then Equation 4-1 predicts a shift to higher levels of strain localization. This behavior is observed qualitatively in the predicted strain localization from compression testing (Figure 4-21). The physically aged data set is offset to higher levels of localization while maintaining general rate dependencies seen in the as received material. In Figure 4-22 localization measured in shear bands is shown for physically aged PMMA. At low strain rates, higher levels of strain localization are observed while the response at higher rates is similar to that of the un-aged glass. The effect of physical aging on the dynamic mechanical response can be seen in Figure 4-25. Aging primarily affects

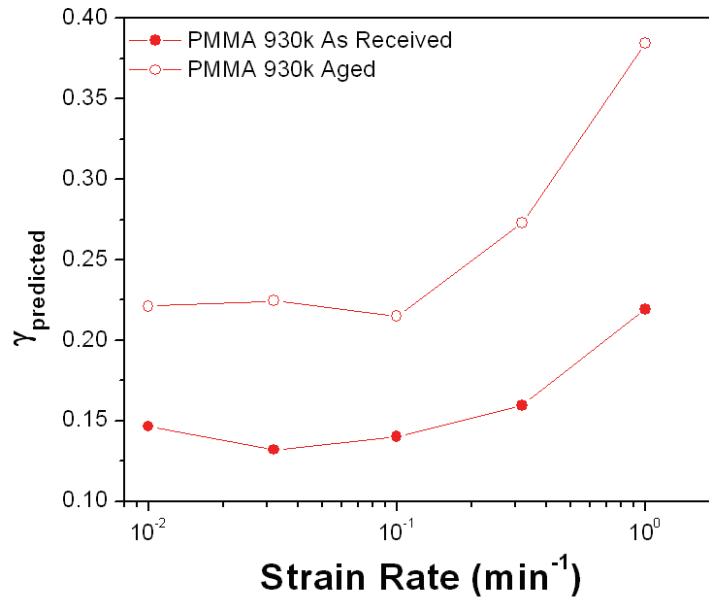


Figure 4-21. Predicted strain localization of physically aged PMMA. At 23° C.

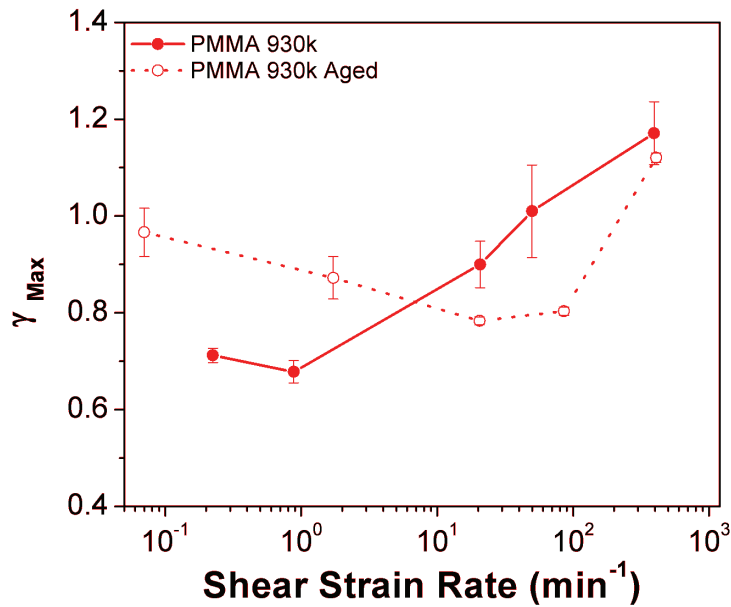


Figure 4-22. Strain localization in physically aged PMMA. Localization is higher at lower strain rates. Rate sensitivity is decreased until the highest rate. At 23° C.

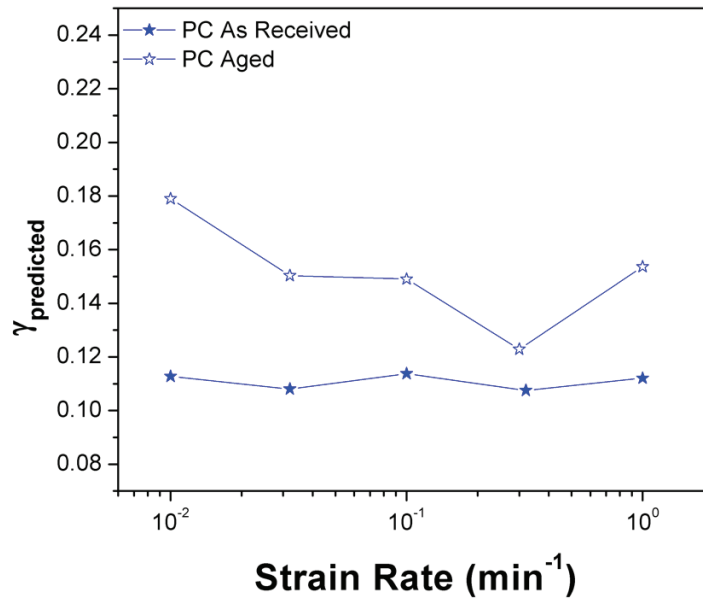


Figure 4-23. Predicted strain localization in aged PC. At 23° C.

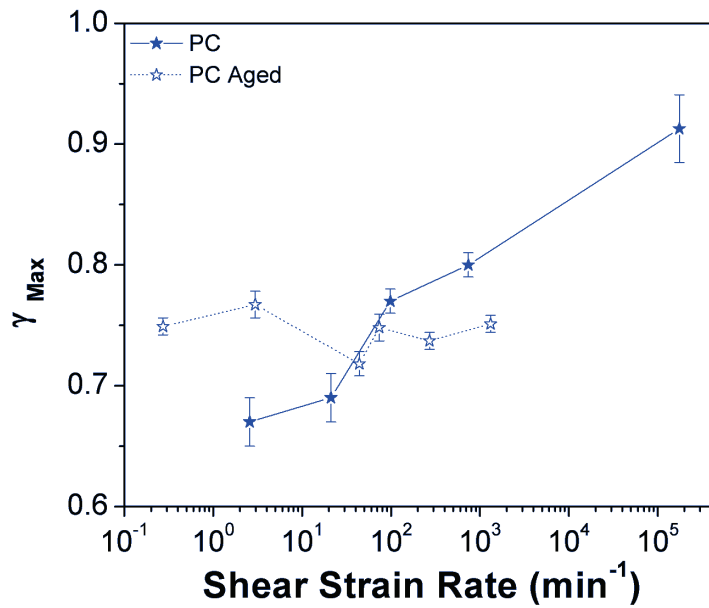


Figure 4-24. Strain localization in physically aged PC. Localization is higher at lower strain rates. Rate sensitivity is decreased. At 23° C.

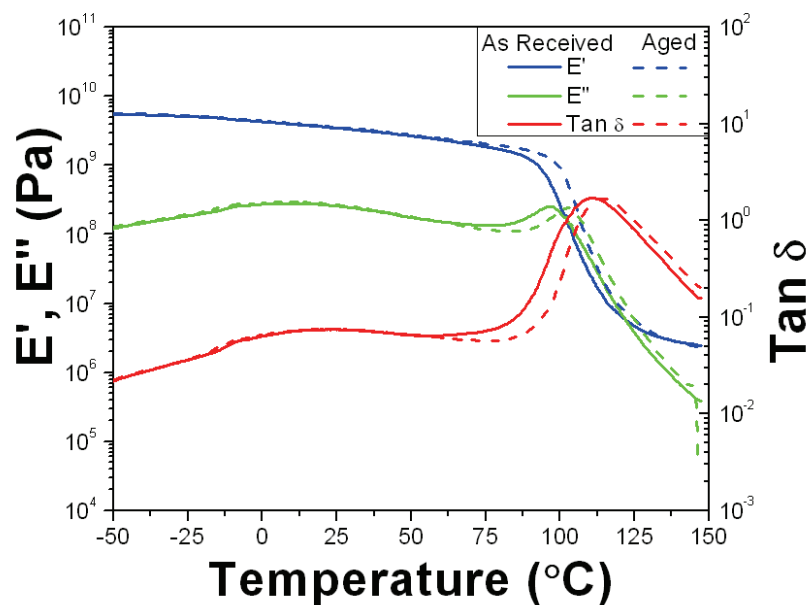


Figure 4-25. DMA on PMMA both as received and after physical aging. Aging results in narrowing of the alpha transition.  $\omega=1$  Hz.

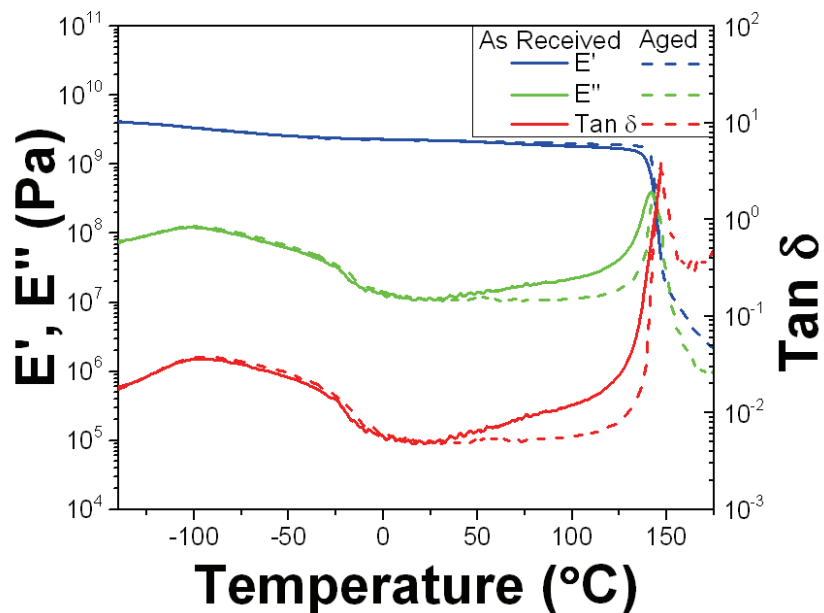


Figure 4-26. DMA on PC both as received and after physical aging. Aging results in narrowing of the alpha transition.  $\omega=1$  Hz.

the alpha transition leaving the beta transition relatively unaltered.<sup>72,85,86</sup> In both PMMA and PC, aging results in a narrowing of the relaxation spectrum associated with the alpha transition. Likewise, one would expect this to have an effect on processes dominated by the alpha transition.

In the low rate / high temperature limit ( $T_\beta < T < T_g$ ), the yield and post-yield response is dominated by the alpha process. As rates increase and/or temperatures decrease to values near  $T_\beta$ , the secondary beta process will contribute more to the deformation response. The similarity of the level of shear strain at the highest strain rate for the aged and as-received PMMA suggests that the beta process contributes more at higher rates.

Aged PC shows almost no rate sensitivity compared to the as-received material. The as received material has a positive slope in the loss modulus and  $\tan \delta$  between 25° and 100° C. The narrowing of the alpha transition in PC results in a plateau in the dynamic mechanical response for the same temperature range.

These results provide a nice counter balance to the section discussing the relation of the test temperature to the beta relaxation.

The process of physical aging leaves the portion of the relaxation spectrum associated with the beta relaxation essentially unchanged. This shows that the strain localization process is not merely affected by local molecular motions but also by cooperative motions associated with the alpha process.

### Conclusions

The strain localization process that accompanies shear band formation depends on many aspects of the structure and state of the glassy polymer. The process is dependent on the correlations of molecular mobility with large scale deformation. It has been demonstrated in this work that both the alpha and beta relaxations contribute to the process in PMMA and PC. The relation of the test temperature to the beta relaxation has a large effect on the relative rate sensitivity of strain localization. When deformation takes place in the region of the beta relaxation temperature, changes in rate exclude or include a larger portion of the relaxation spectrum. The strain localization process results from the polymer's ability to dissipate energy. This process seems to be strongly influenced by mobility of the local structure associated with the beta relaxation. Near the beta relaxation temperature, both PMMA and PC have increased rate sensitivity. In the temperature range above the beta transition and below

the alpha transition, the rate sensitivity is decreased in both PMMA and PC. In this temperature regime there is enough thermal energy to activate the entire relaxation spectrum that contributes to the beta relaxation. Changes in strain rate in this regime were not drastic enough to exclude beta motions, subsequently the rate sensitivity is significantly diminished.

The nature of the alpha transition also affects strain localization. When PMMA or PC are physically aged, there is a narrowing of the alpha transition primarily from the low temperature side. Physical aging has a minimal effect on the beta transition so the localization process is dependent on both alpha and beta transitions. The effect of physical aging on localization is somewhat complicated. At lower strain rates, higher levels of localization are observed while the response resembles the unaged glass at higher rates. One possible explanation for this behavior is a transition from alpha process dominated deformation to beta process dominated deformation.

## References

57. Bauwens Crowet, C., BAUWENS, J. & Homes, G. Tensile yield-stress behavior of glassy polymers. *Journal of Polymer Science Part A-2: Polymer Physics* **7**, 735-742 (1969).
58. Eyring, H. Viscosity, Plasticity, and Diffusion as Examples of Absolute Reaction Rates. *J. Chem. Phys.* **4**, 283 (1936).
59. Bauwens Crowet, C. & BAUWENS, J. Effect of Thermal History on the Tensile Yield Stress of Polycarbonate in the Beta-Transition Range. *Polymer* **24**, 921-924 (1983).
60. Bauwens Crowet, C. & Homes, G. Plastic Deformation of Polymethyl Methacrylate in the Glassy State. *Academie des Sciences Comptes Rendus (Paris)* **259**, 3434 (1964).
61. Roetling, J. A. Yield stress behaviour of polymethylmethacrylate. *Polymer* **6**, 311-317 (1965).
62. Roetling, J. A. Yield stress behaviour of poly(ethyl methacrylate) in the glass transition region. *Polymer* **6**, 615-619 (1965).
63. Roetling, J. A. Yield stress behaviour of isotactic polypropylene. *Polymer* **7**, 303-306 (1966).
64. Archer, J. S. & Lesser, A. J. Shear band formation and mode II fracture of polymeric glasses. *J. Polym. Sci. B Polym. Phys.* **49**, 103-114 (2010).
65. Klompen, E. T. J., Engels, T. A. P., Govaert, L. E. & Meijer, H. E. H. Modeling of the Postyield Response of Glassy Polymers: Influence of Thermomechanical History. *Macromolecules* **38**, 6997-7008 (2005).

66. van Breeman, L. C. A., Engels, T. A. P., Govaert, L. E. & Meijer, H. E. H. Modelling thermorheologically complex phenomena in the post-yield response of glassy polymers. *13th International Conference on Deformation, Yield and Fracture of Polymers, Rolduc Abbey, Kerkrade* (2006).
67. Monnerie, L., Halary, J. & Kausch, H.-H. Deformation, Yield and Fracture of Amorphous Polymers: Relation to the Secondary Transitions. *Intrinsic Molecular Mobility and Toughness of Polymers I* 215-372 (2005).doi:10.1007/b136957
68. Cangialosi, D., Schut, H., van Veen, A. & Picken, S. J. Positron Annihilation Lifetime Spectroscopy for Measuring Free Volume during Physical Aging of Polycarbonate. *Macromolecules* **36**, 142-147 (2012).
69. Heater, K. & Agrawal, C. The effects of physical aging in polycarbonate. *J. Polym. Sci.* (1990).
70. van Melick, H. G. H., Govaert, L. E. & Meijer, H. E. H. Localisation phenomena in glassy polymers: influence of thermal and mechanical history. *Polymer* **44**, 3579-3591 (2003).
71. Lyulin, A. & Michels, M. Time Scales and Mechanisms of Relaxation in the Energy Landscape of Polymer Glass under Deformation: Direct Atomistic Modeling. *Phys. Rev. Lett.* **99**, (2007).
72. Struik, L. *Physical aging in polymers and other amorphous materials*. (Elsevier: Amsterdam, 1978).
73. Struik, L. On the rejuvenation of physically aged polymers by mechanical deformation. *Polymer* **38**, 4053-4057 (1997).

74. Lee, H.-N. & Ediger, M. D. Mechanical Rejuvenation in Poly (methyl methacrylate) Glasses? Molecular Mobility after Deformation. *Macromolecules* **43**, 5863-5873 (2012).
75. McKenna, G. Mechanical rejuvenation in polymer glasses: fact or fallacy? *Journal of Physics: Condensed Matter* (2003).
76. Isner, B. & Lacks, D. Generic Rugged Landscapes under Strain and the Possibility of Rejuvenation in Glasses. *Phys. Rev. Lett.* **96**, (2006).
77. Van Melick, H., Govaert, L., Raas, B., Nauta, W. & Meijer, H. Kinetics of ageing and re-embrittlement of mechanically rejuvenated polystyrene. *Polymer* **44**, 1171-1179 (2003).
78. Govaert, L., Van Melick, H. & Meijer, H. Temporary toughening of polystyrene through mechanical preconditioning. *Polymer* **42**, 1271-1274 (2001).
79. Govaert, L. E., Timmermans, P. H. M. & Brekelmans, W. A. M. The Influence of Intrinsic Strain Softening on Strain Localization in Polycarbonate: Modeling and Experimental Validation. *J Eng Mater Technol* **122**, 177-185 (2000).
80. Kierkels, J. T. A. *Tailoring the mechanical properties of amorphous polymers*. 138 (2006).
81. Manring, L. E. Thermal degradation of poly(methyl methacrylate). 4. Random side-group scission. *Macromolecules* **24**, 3304-3309 (2012).
82. Schmidt-Rohr, K. *et al.* Molecular Nature of the .beta. Relaxation in Poly(methyl methacrylate) Investigated by Multidimensional NMR. *Macromolecules* **27**, 4733-4745 (1994).

83. Yee, A. F. & Smith, S. A. Molecular structure effects on the dynamic mechanical spectra of polycarbonates. *Macromolecules* **14**, 54-64 (2012).
84. Hansen, M. T. *et al.* Influence of tensile stress on the phenylene flips in polycarbonate studied by two-dimensional solid-state NMR. *Macromolecules* **25**, 5542-5544 (2012).
85. Tordjeman, P., Teze, L. & Halary, J. On the plastic and viscoelastic behavior of methylmethacrylate-based random copolymers. *Polymer Engineering & ...* (1997).
86. Muzeau, E., Vigier, G., Vassoille, R. & Perez, J. Changes of thermodynamic and dynamic mechanical properties of poly (methyl methacrylate) due to structural relaxation: low-temperature ageing and modelling. *Polymer* **36**, 611-620

APPENDIX: SHEAR BAND CALCULATIONS AND SUPPLEMENTAL STRESS  
STRAIN DATA

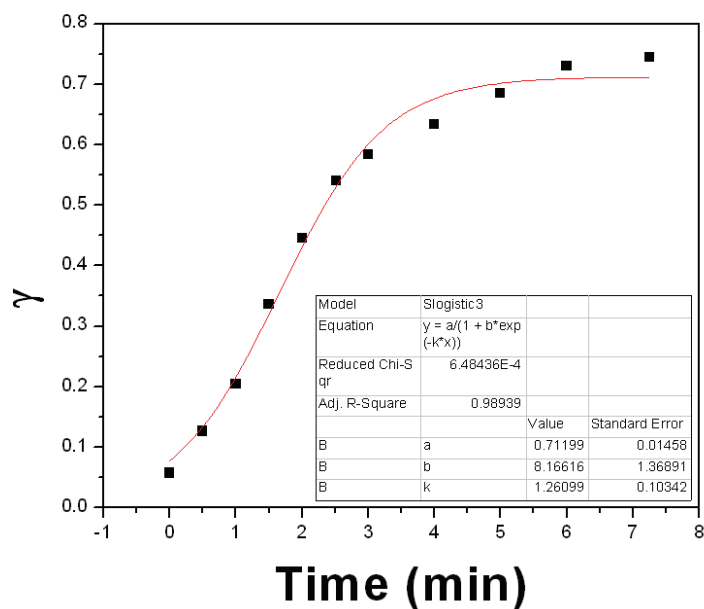


Figure A-1. PMMA 930 kg/mol 0.1 mm/min compression rate shear band strain as a function of time.

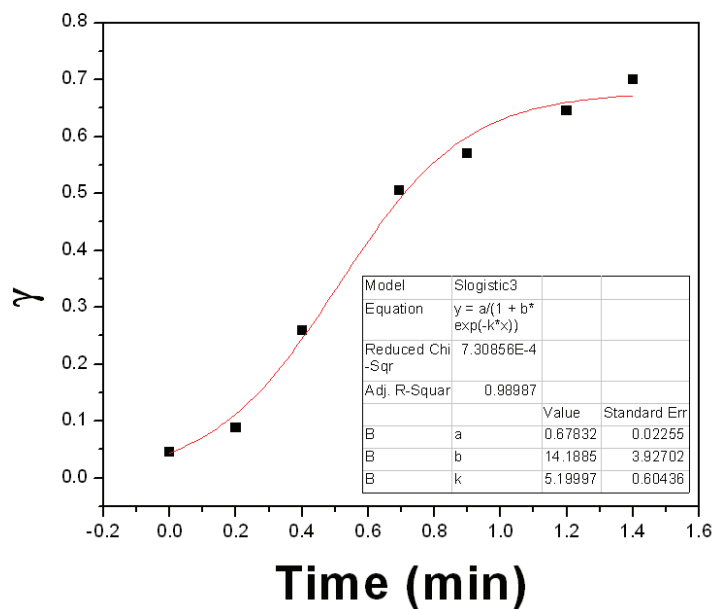


Figure A-2. PMMA 930 kg/mol 1 mm/min compression rate shear band strain as a function of time.

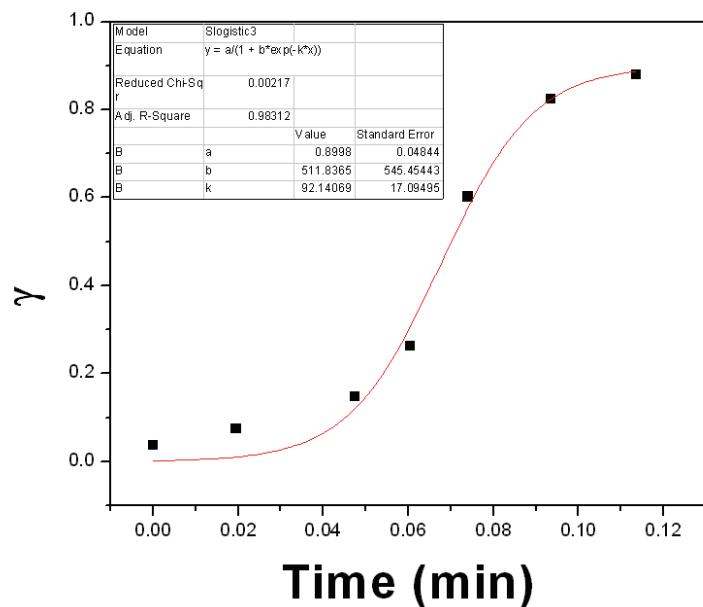


Figure A-3. PMMA 930 kg/mol 10 mm/min compression rate shear band strain as a function of time.

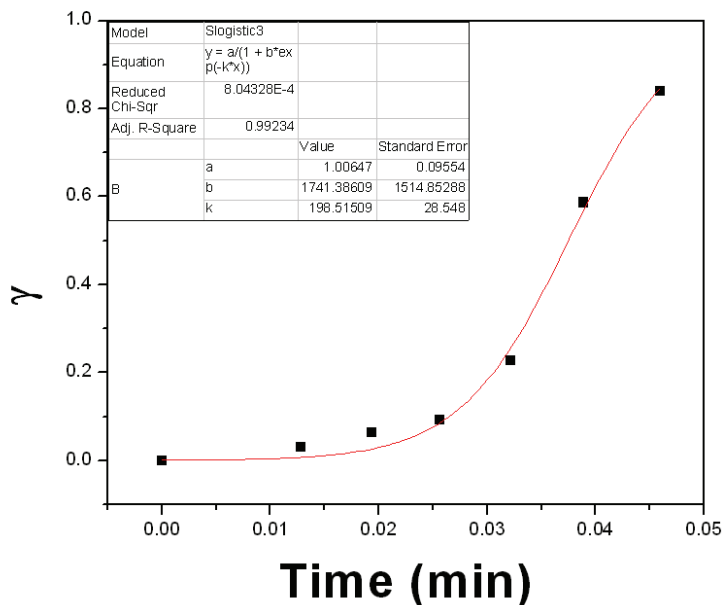


Figure A-4. PMMA 930 kg/mol 32 mm/min compression rate shear band strain as a function of time.

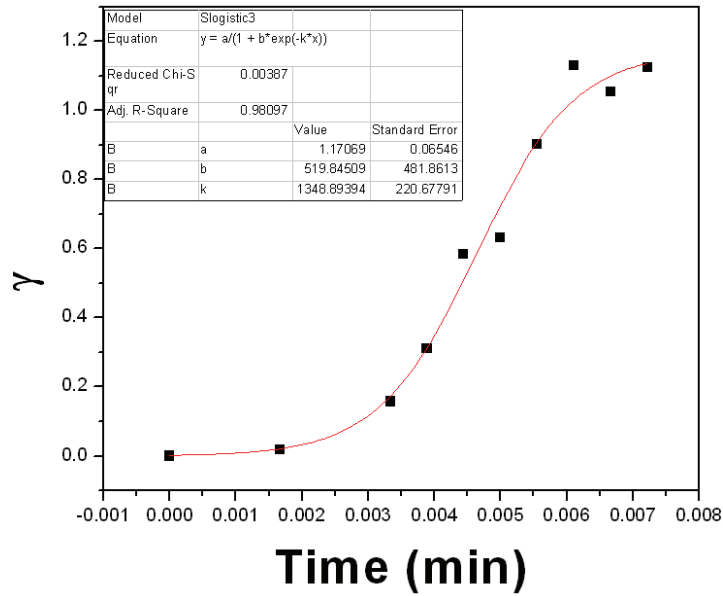


Figure A-5. PMMA 930 kg/mol 100 mm/min compression rate shear band strain as a function of time.

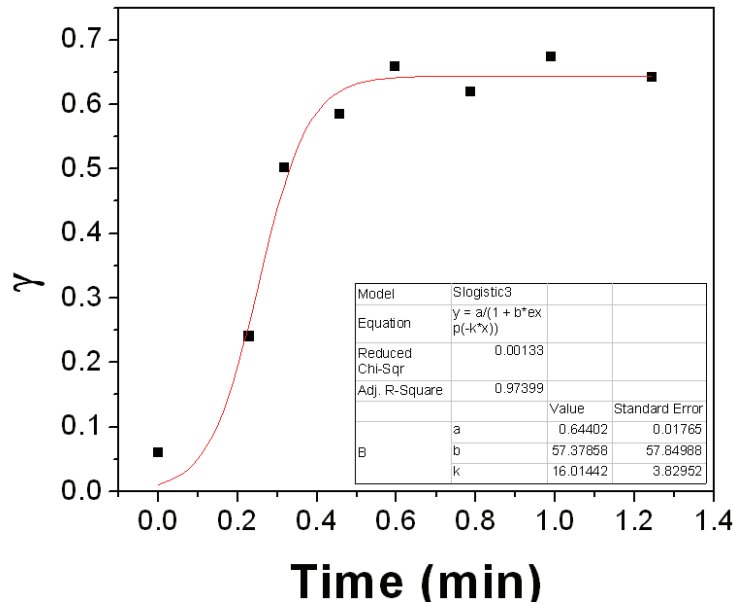


Figure A-6. PC 1 mm/min compression rate shear band strain as a function of time.

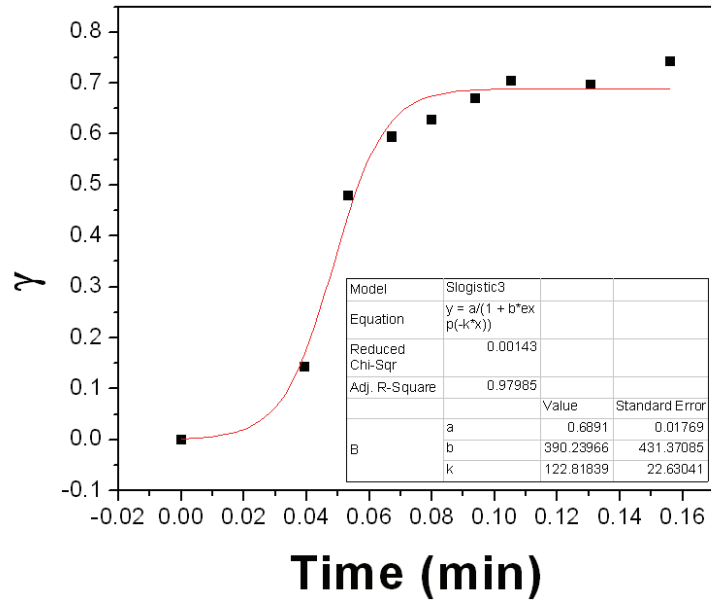


Figure A-7. PC 10 mm/min compression rate shear band strain as a function of time.

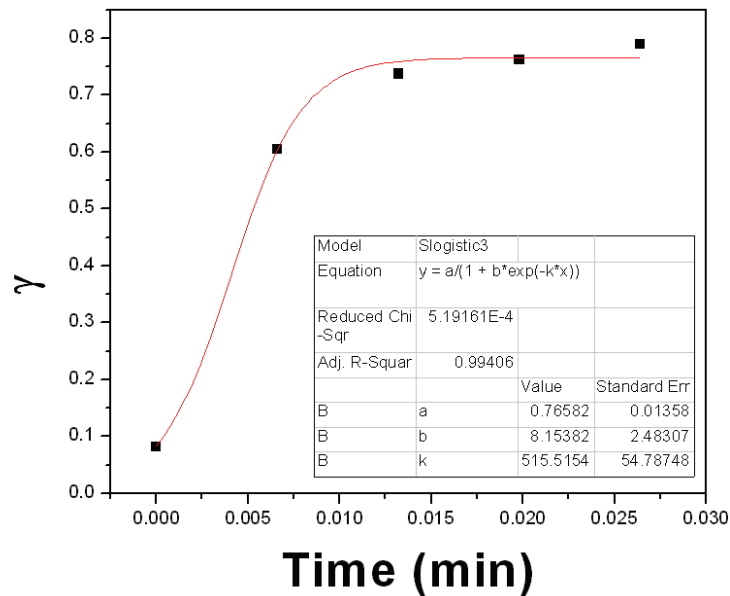


Figure A-8. PC 100 mm/min compression rate shear band strain as a function of time.

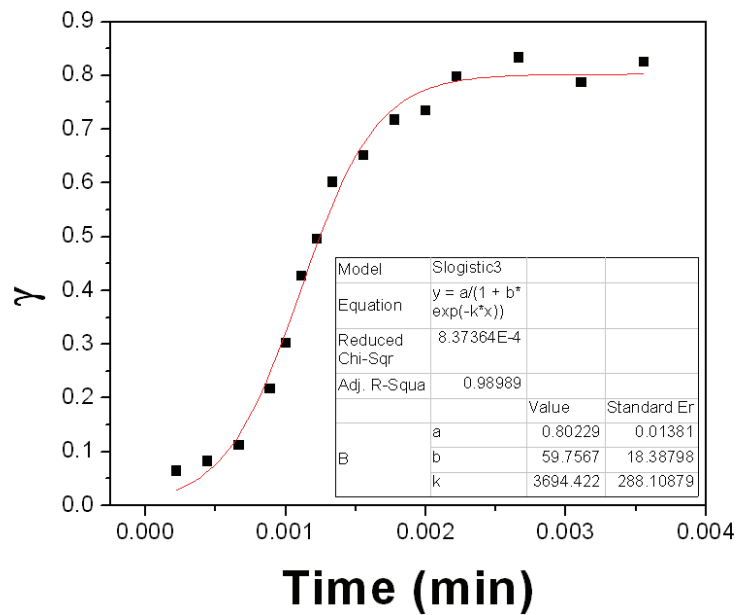


Figure A-9. PC 500 mm/min compression rate shear band strain as a function of time.

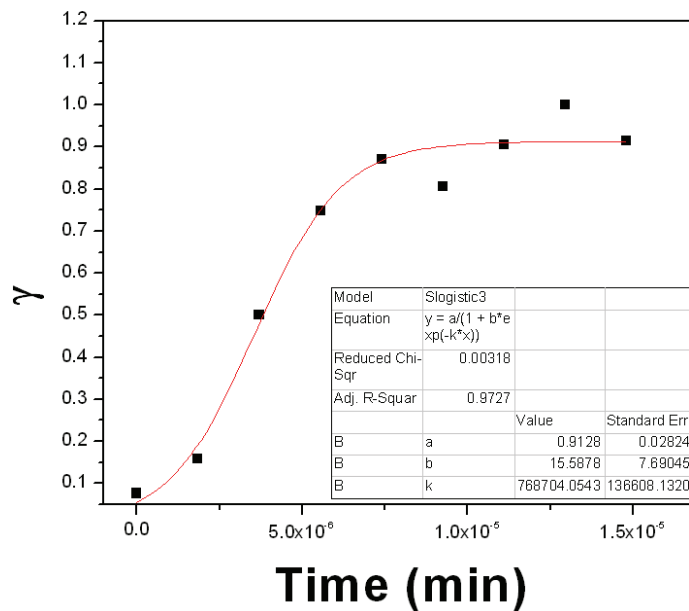


Figure A-10. PC 250 m/min compression rate shear band strain as a function of time.

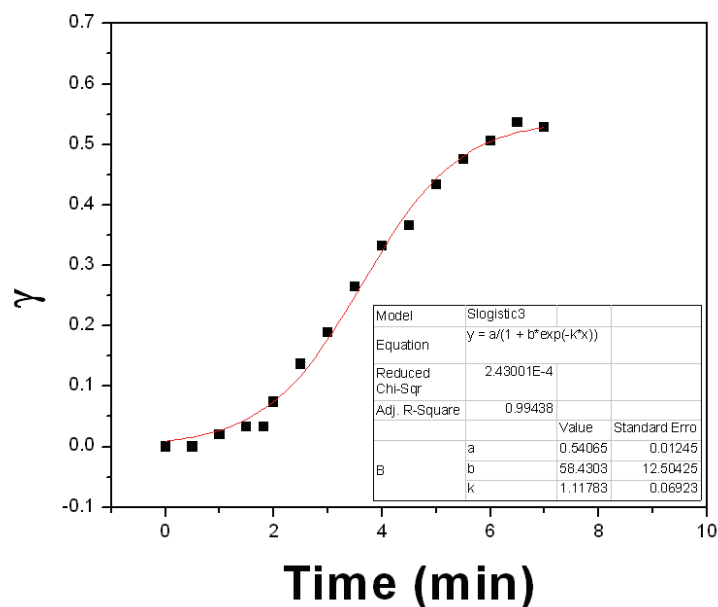


Figure A-11. PMMA 1.1 kg/mol 0.1 mm/min compression rate shear band strain as a function of time.

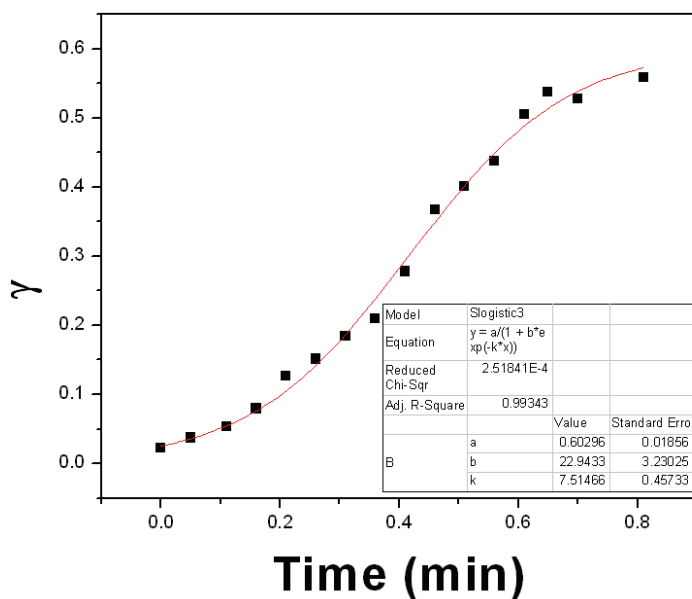


Figure A-12. PMMA 1.1 kg/mol 1 mm/min compression rate shear band strain as a function of time.

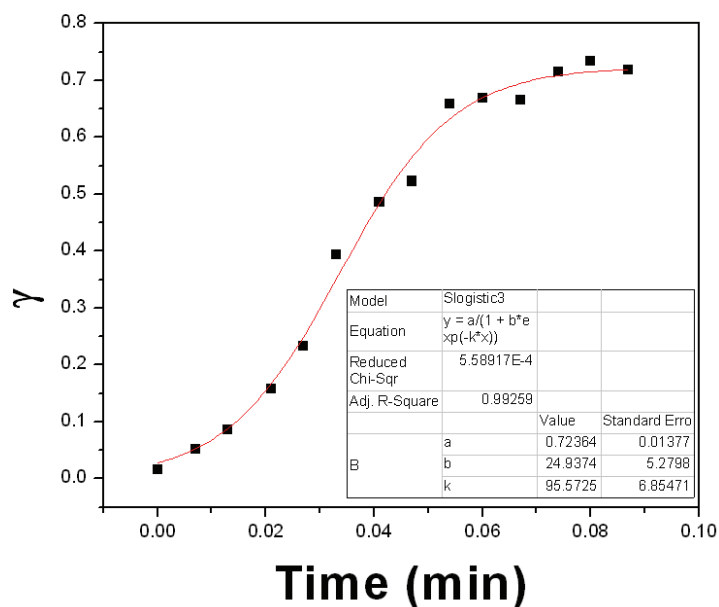


Figure A-13. PMMA 1.1 kg/mol 10 mm/min compression rate shear band strain as a function of time.

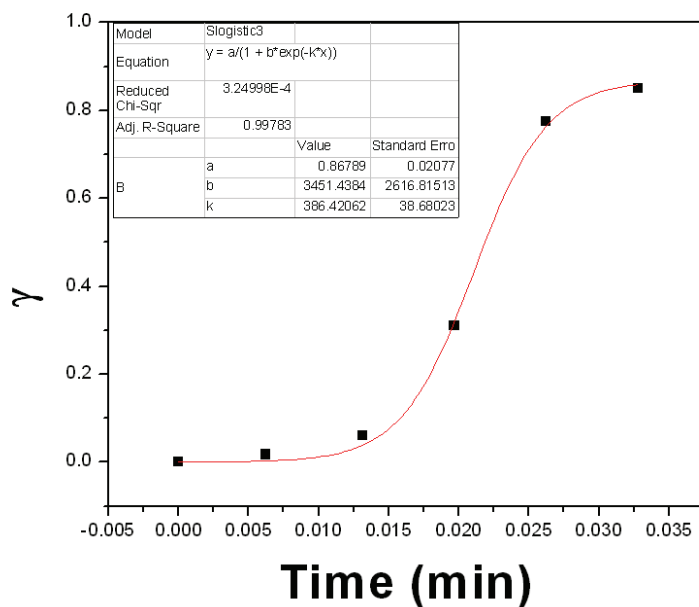


Figure A-14. PMMA 1.1 kg/mol 32 mm/min compression rate shear band strain as a function of time.

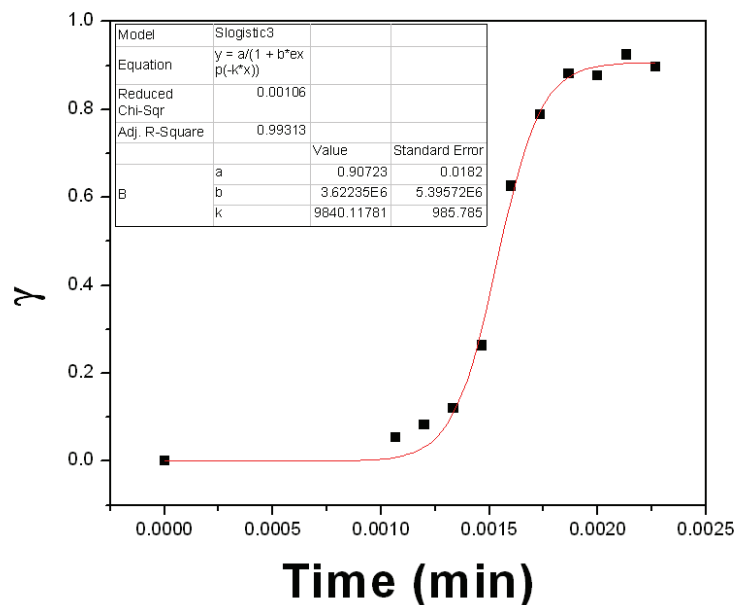


Figure A-15. PMMA 1.1 kg/mol 500 mm/min compression rate shear band strain as a function of time.

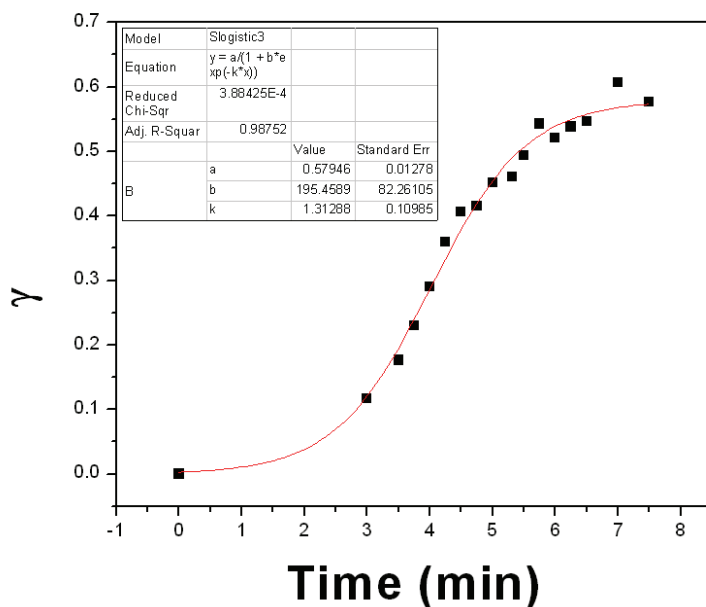


Figure A-16. PMMA-co-EA 0.1 mm/min compression rate shear band strain as a function of time.

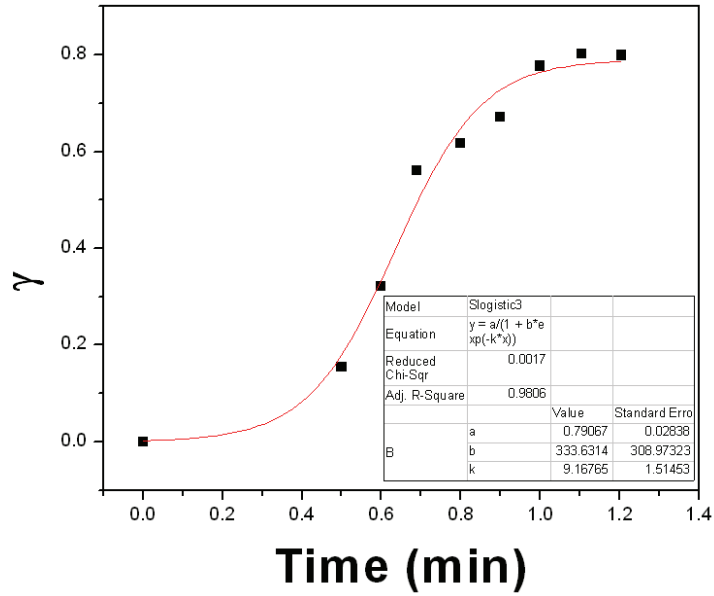


Figure A-17. PMMA-co-EA 1 mm/min compression rate shear band strain as a function of time.

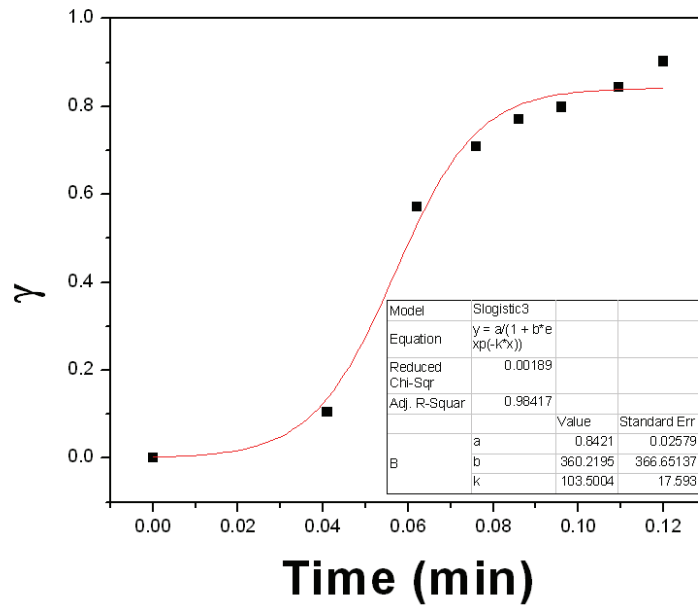


Figure A-18. PMMA-co-EA 10 mm/min compression rate shear band strain as a function of time.

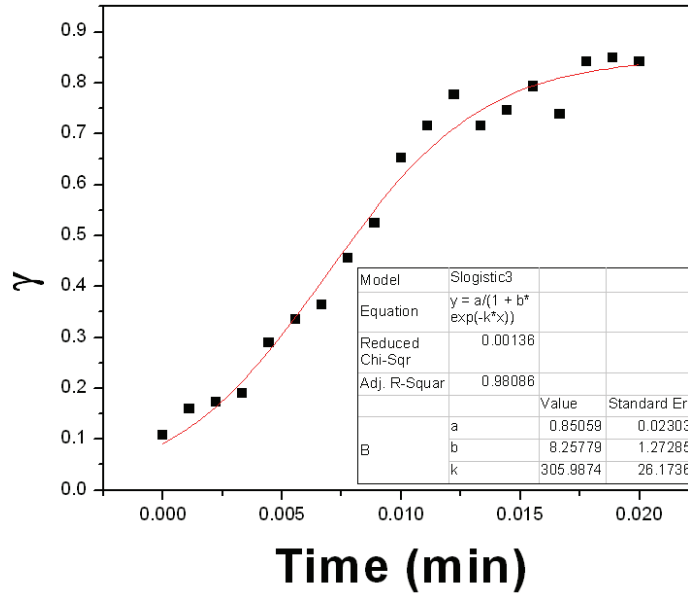


Figure A-19. PMMA-co-EA 32 mm/min compression rate shear band strain as a function of time.

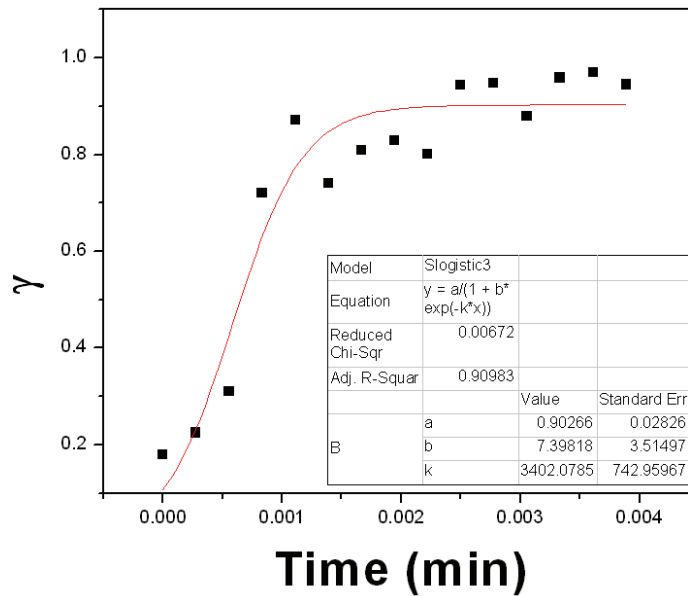


Figure A-20. PMMA-co-EA 100 mm/min compression rate shear band strain as a function of time.

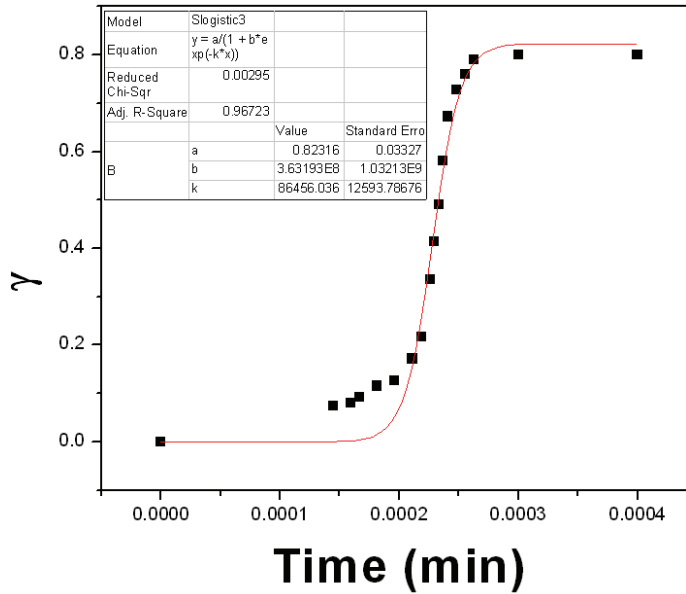


Figure A-21. PMMA-co-EA 500 mm/min compression rate shear band strain as a function of time.

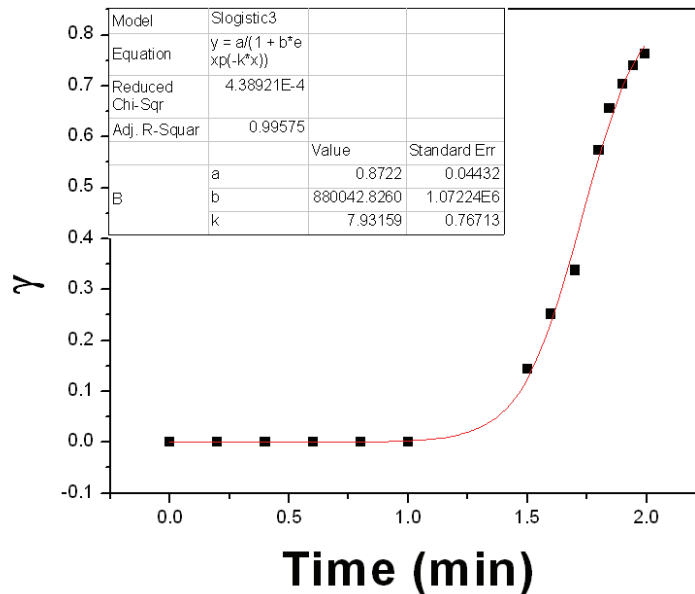


Figure A-22. PMMA 930 kg/mol aged 85 hours 1 mm/min compression rate shear band strain as a function of time.

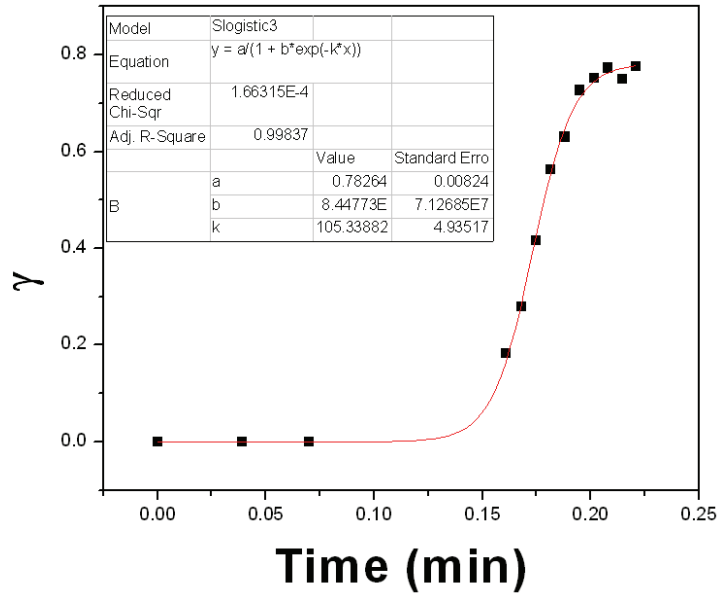


Figure A-23. PMMA 930 kg/mol aged 85 hours 10 mm/min compression rate shear band strain as a function of time.

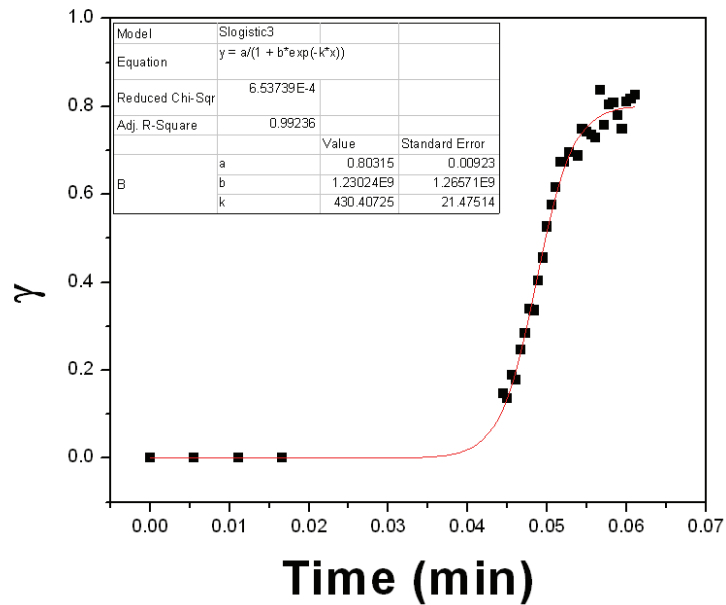


Figure A-24. PMMA 930 kg/mol aged 85 hours 32 mm/min compression rate shear band strain as a function of time.

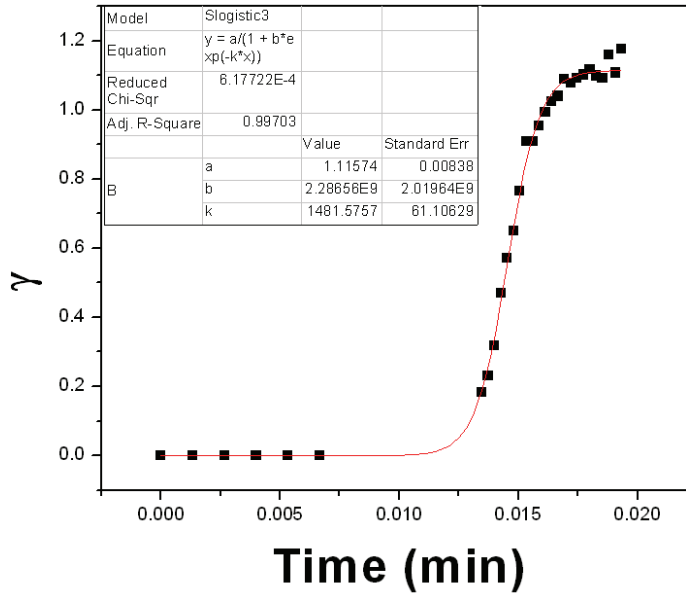


Figure A-25. PMMA 930 kg/mol aged 85 hours 100 mm/min compression rate shear band strain as a function of time.

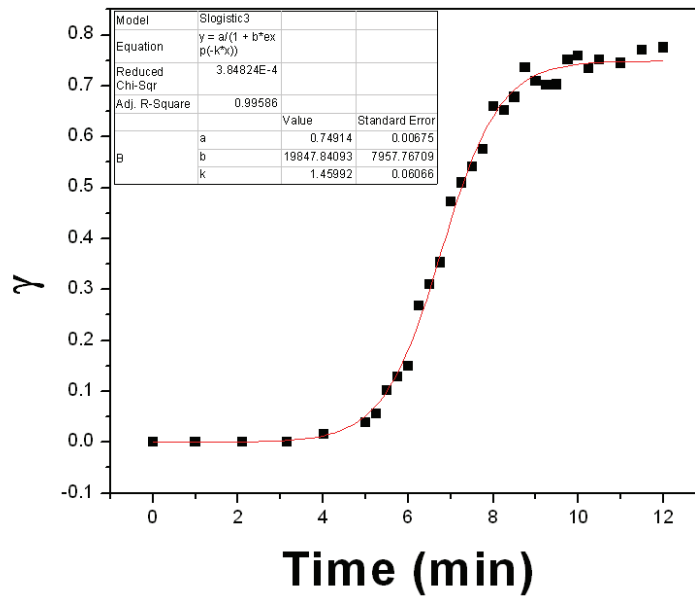


Figure A-26. PC aged 85 hours 0.1 mm/min compression rate shear band strain as a function of time.

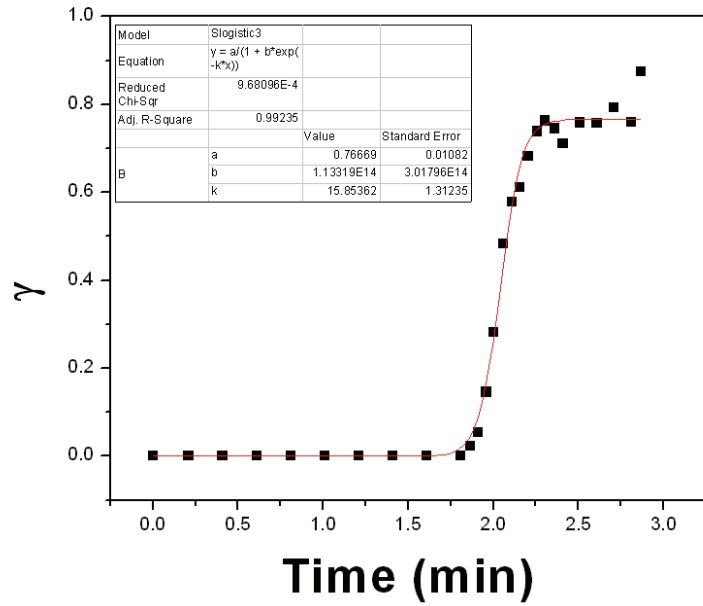


Figure A-27. PC aged 85 hours 1 mm/min compression rate shear band strain as a function of time.

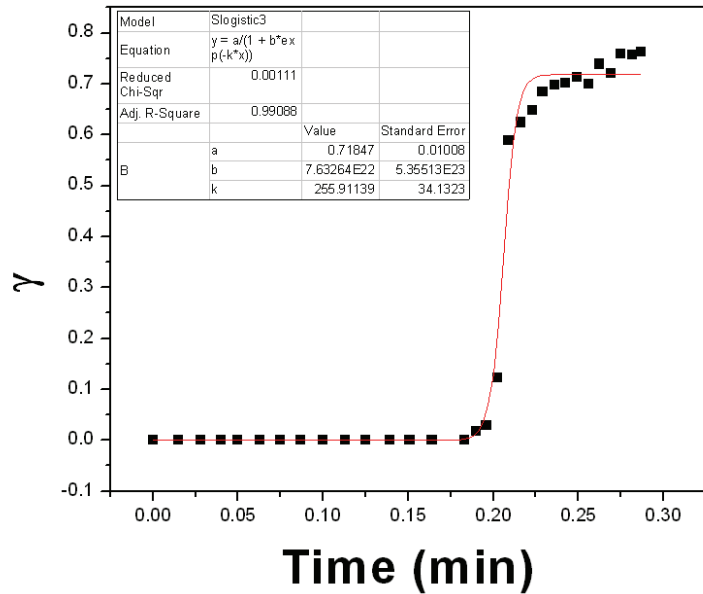


Figure A-28. PC aged 85 hours 10 mm/min compression rate shear band strain as a function of time.

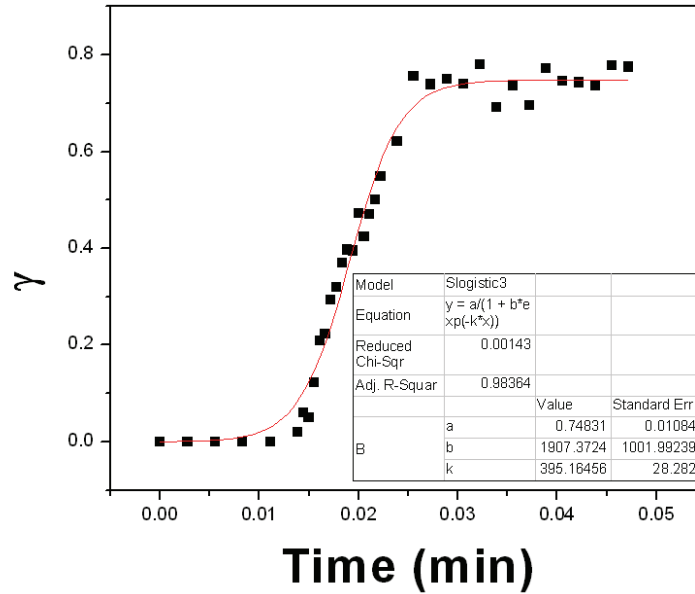


Figure A-29. PC aged 85 hours 32 mm/min compression rate shear band strain as a function of time.

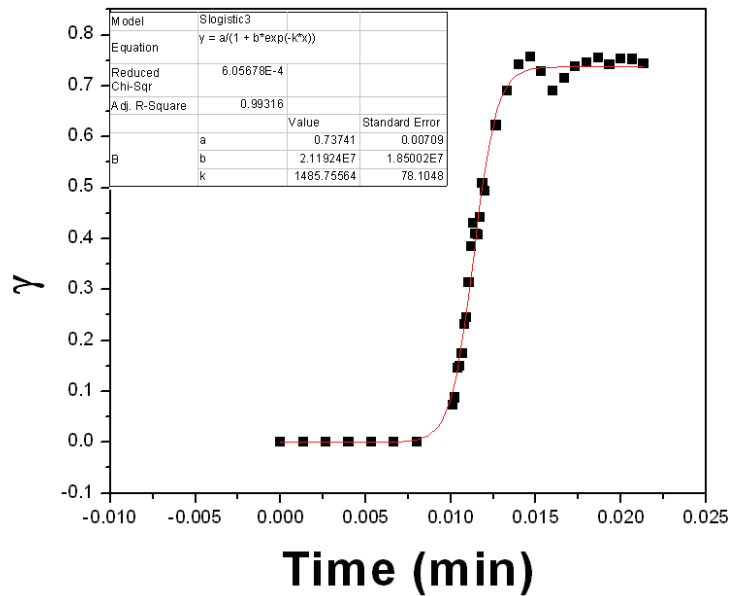


Figure A-30. PC aged 85 hours 100 mm/min compression rate shear band strain as a function of time.

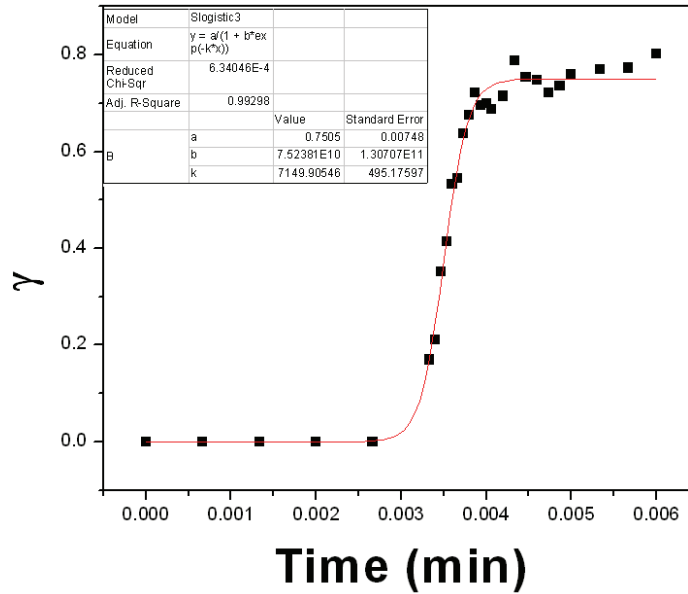


Figure A-31. PC aged 85 hours 500 mm/min compression rate shear band strain as a function of time.

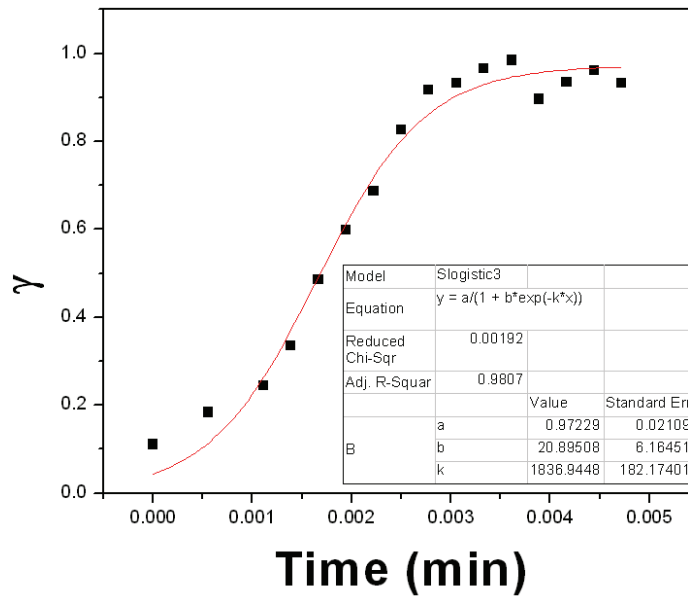


Figure A-32. PMMA 1.1 kg/mol 100 mm/min compression rate shear band strain as a function of time.

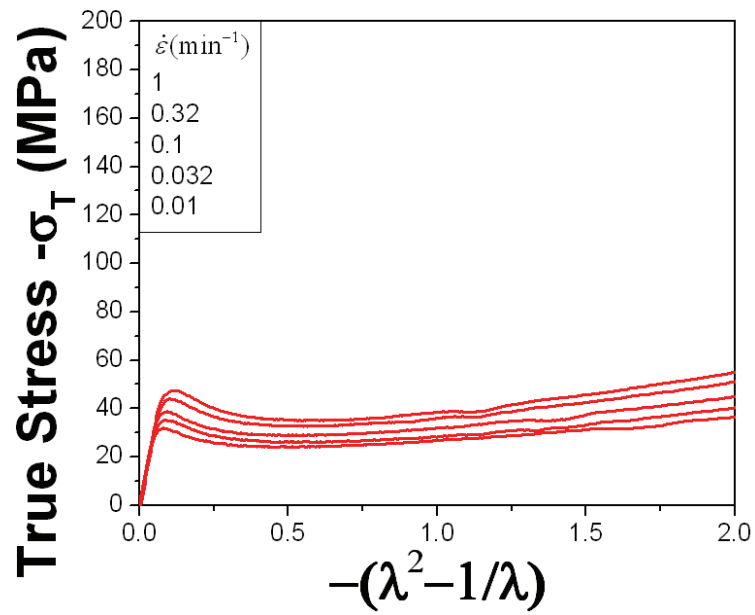


Figure A-33. Compression testing of PMMA 930k above  $T_{\beta}$  (80°C).

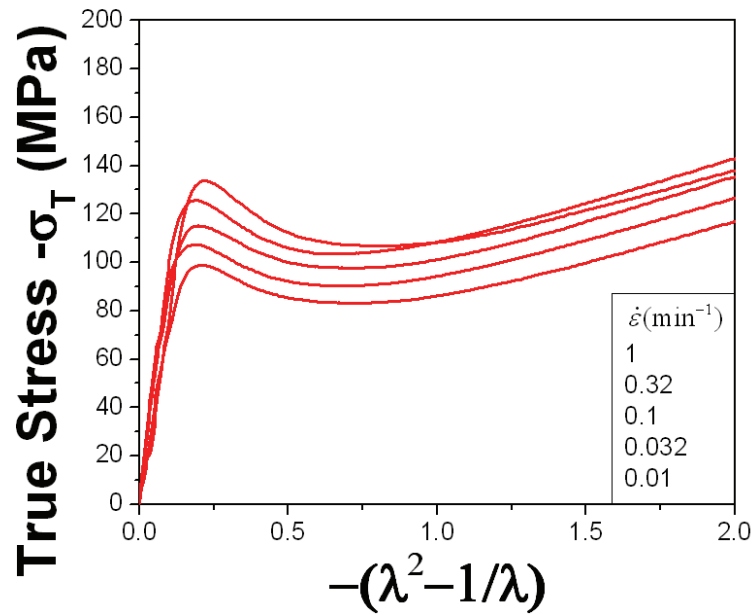


Figure A-34. Compression testing of physically aged PMMA 930k at room temperature.

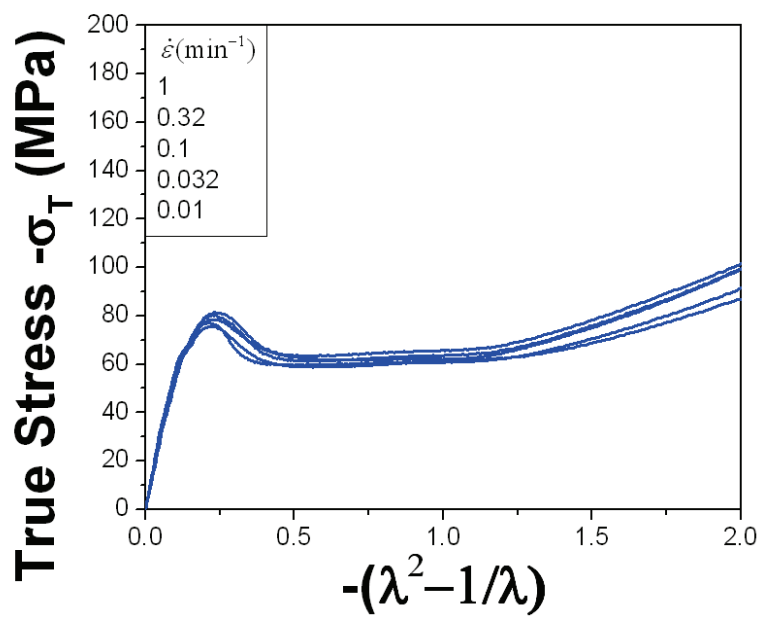


Figure A-35. Compression testing of physically aged PC at room temperature.

## BIBLIOGRAPHY

1. Lewis, G. & Mladi, S. Correlation between impact strength and fracture toughness of PMMA-based bone cements. *Biomaterials* **21**, 775-781 (2000).
2. Hsieh, A. J., DeSchepper, D., Moy, P., Dehmer, P. G. & Song, J. W. The Effects of PMMA on Ballistic Impact Performance of Hybrid Hard/Ductile All-Plastic- and Glass-Plastic-Based Composites. *Army Research Laboratories* (2004).
3. Freyssinet, E. & Seailles, J. US Patent #2080074, Piece of reenforced concrete. (1937).
4. Minor, J. Focus on Glass. *APT bulletin* **32**, 47-50 (2001).
5. T J Holmquist G R Johnson Modeling projectile impact onto prestressed ceramic targets. *J. Phys. IV France* **110**, 597-602 (2003).
6. Bao, Y. Prestressed ceramics and improvement of impact resistance. *Materials Letters* **57**, 518-524 (2002).
7. Motahhari, S. & Cameron, J. Fibre Prestressed Composites: Improvement of Flexural Properties through Fibre Prestressing. *Journal of Reinforced Plastics and Composites* **18**, 279-288 (1999).
8. FANCEY, K. S. Prestressed Polymeric Composites Produced by Viscoelastically Strained Nylon 6,6 Fibre Reinforcement. *Journal of Reinforced Plastics and Composites* **19**, 1251-1266 (2000).

9. Pang, J. W. C. & FANCEY, K. S. Analysis of the tensile behaviour of viscoelastically prestressed polymeric matrix composites. *Composites Science and Technology* **68**, 1903-1910 (2008).
10. FANCEY, K. S. Investigation into the feasibility of viscoelastically generated pre-stress in polymeric matrix composites. *Materials Science and Engineering: A* **279**, 36-41 (2000).
11. FANCEY, K. S. Fiber-reinforced polymeric composites with viscoelastically induced prestress. *Journal of advanced materials* **37**, 21-29 (2005).
12. Pang, J. W. C. & FANCEY, K. S. An investigation into the long-term viscoelastic recovery of Nylon 6,6 fibres through accelerated ageing. *Materials Science and Engineering: A* **431**, 100-105 (2006).
13. FANCEY, K. S. Viscoelastically prestressed polymeric matrix composites - Potential for useful life and impact protection. *Composites Part B: Engineering* **41**, 454-461 (2010).
14. Hsieh, A. J. & Song, J. W. Measurements of Ballistic Impact Response of Novel Coextruded PC/PMMA Multilayered-Composites. *Journal of Reinforced Plastics and Composites* **20**, 239-254 (2001).
15. Hsieh, A. J. High strain-rate behavior of coextruded polycarbonate/PMMA composites. *Shock compression of condensed matter* **505**, 555-558
16. Archer, J. S. & Lesser, A. J. Impact resistant polymeric glasses using compressive pre-stress. *J. Appl. Polym. Sci.* **114**, 3704-3715 (2009).

17. Dally, J. W. & Riley, W. F. *Experimental Stress Analysis*. (McGraw-Hill: New York, 1991).
18. Saada, A. S. *Elasticity: Theory and Applications*. (Krieger: Malabar, Florida, 1993).
19. Frisch-Fay, R. *Flexible Bars*. (Butterworths: Washington DC, 1962).
20. *MatWeb* at <<http://www.matweb.com>>
21. Timoshenko, S. & Woinowsky-Krieger, S. *Theory of Plates and Shells*. (McGraw-Hill: New York, 1959).
22. Beardmore, P. & Fellers, J. Characteristic fracture features of polymethyl methacrylate. *Materials Science and Engineering* **5**, 120-125
23. Bhattacharjee, D. & Knott, J. F. Effect of mixed mode I and II loading on the fracture surface of polymethyl methacrylate (PMMA). *Int J Fract* **72**, 359-381 (1995).
24. Saada, A. S. *Elasticity: Theory and Applications*. (Krieger: Malabar, Florida, 1993).
25. Lu, H. & Knauss, W. G. The role of dilatation in the nonlinearly viscoelastic behavior of PMMA under multiaxial stress states. *Mechanics of Time-Dependent Materials* **2**, 307-334 (1998).
26. Gol'dman, A. Y., Demenchuk, N. P. & Murzakhanov, G. K. Stress relaxation in polymeric materials under hydrostatic pressure. *Mech Compos Mater* **24**, 707-714 (1989).
27. Price, C. Effect of pressure on the formation of poly(methyl methacrylate) glasses. *Polymer* **16**, 585-589

28. Sauer, J. Deformation, yield and fracture of polymers at high pressure. *Polymer Engineering and Science* **17**, 150-164 (1977).
29. Wang, W. C. V., Kramer, E. J. & Sachse, W. H. Effects of high-pressure CO<sub>2</sub> on the glass transition temperature and mechanical properties of polystyrene. *Journal of Polymer Science: Polymer Physics Edition* **20**, 1371-1384 (1982).
30. Quinson, R., Perez, J., Rink, M. & Pavan, A. Yield criteria for amorphous glassy polymers. *J Mater Sci* **32**, 1371-1379 (1997).
31. Hasan, O., Boyce, M., Li, X. & Berko, S. An investigation of the yield and postyield behavior and corresponding structure of poly (methyl methacrylate). *J. Polym. Sci. B Polym. Phys.* **31**, 185-197 (1993).
32. O'reilly, J. M. The effect of pressure on glass temperature and dielectric relaxation time of polyvinyl acetate. *J. Polym. Sci.* **57**, 429-444 (1962).
33. Rabinowitz, S., Ward, I. M. & Parry, J. S. C. The effect of hydrostatic pressure on the shear yield behaviour of polymers. *J Mater Sci* **5**, 29-39 (1970).
34. Hsieh, A. J., DeSchepper, D., Moy, P., Dehmer, P. G. & Song, J. W. The Effects of PMMA on Ballistic Impact Performance of Hybrid Hard/Ductile All-Plastic- and Glass-Plastic-Based Composites. *Army Research Laboratories* (2004).
35. Archer, J. S. & Lesser, A. J. Impact resistant polymeric glasses using compressive pre-stress. *J. Appl. Polym. Sci.* **114**, 3704-3715 (2009).
36. Ayatollahi, M. R., Aliha, M. R. M. & Hassani, M. M. Mixed mode brittle fracture in PMMA--An experimental study using SCB

- specimens. *Materials Science and Engineering: A* **417**, 348-356 (2006).
37. Ayatollahi, M. R. & Aliha, M. R. M. On determination of mode II fracture toughness using semi-circular bend specimen. *International Journal of Solids and Structures* **43**, 5217-5227 (2006).
  38. Erdogan, F. & Sih, G. C. On the crack extension in plates under plane loading and transverse shear. *Journal of Basic Engineering* **85**, 519-525 (1963).
  39. Melin, S. When does a crack grow under mode II conditions? *Int J Fract* **30**, 103-114-114
  40. Broberg, K. B. On Crack Paths. *Engineering Fracture Mechanics* **28**, 663-679 (1987).
  41. Kalthoff, J. F. Shadow optical analysis of dynamic fracture. *Optical Engineering* **27**, 835-840 (1988).
  42. Ravi-Chandar, K., Lu, J., Yang, B. & Zhu, Z. Failure mode transitions in polymers under high strain rate loading. *Int J Fract* **101**, 33-72 (2000).
  43. Rosenfield, A. R. & Kanninen, M. F. The fracture mechanics of glassy polymers. *Journal of Macromolecular Science, Part B: Physics* **7**, 609-631 (1973).
  44. Johnson, F. A. & Radon, J. C. Fracture Process and Molecular Kinetics of Pmma. *Journal of Polymer Science Part a-Polymer Chemistry* **11**, 1995-2020 (1973).
  45. Beardmore, P. & Fellers, J. Characteristic fracture features of polymethyl methacrylate. *Materials Science and Engineering* **5**, 120-125

46. Bhattacharjee, D. & Knott, J. F. Effect of mixed mode I and II loading on the fracture surface of polymethyl methacrylate (PMMA). *Int J Fract* **72**, 359-381 (1995).
47. Ward, I. M. & Sweeney, J. *An Introduction to the Mechanical Properties of Solid Polymers*. (John Wiley & Sons: West Sussex 1993).
48. Lee, S. M. Mode II Interlaminar Crack Growth Process in Polymer Matrix Composites. *Journal of Reinforced Plastics and Composites* **18**, 1254-1266 (1999).
49. Kwon, H. J. & Jar, P. Y. B. Fracture toughness of polymers in shear mode. *Polymer* **46**, 12480-12492 (2005).
50. Haward, R. N. The application of a simplified model for the stress-strain curves of polymers. *Polymer* **28**, 1485-1488 (1987).
51. van Melick, H. G. H., Govaert, L. E. & Meijer, H. E. H. Localisation phenomena in glassy polymers: influence of thermal and mechanical history. *Polymer* **44**, 3579-3591 (2003).
52. Boyce, M. C. & Arruda, E. M. An Experimental and Analytical Investigation of the Large Strain Compressive and Tensile Response of Glassy-Polymers. *Polymer Engineering and Science* **30**, 1288-1298 (1990).
53. Monnerie, L., Halary, J. & Kausch, H.-H. Deformation, Yield and Fracture of Amorphous Polymers: Relation to the Secondary Transitions. *Intrinsic Molecular Mobility and Toughness of Polymers I* 215-372 (2005).doi:10.1007/b136957
54. Adams, G. W. & Farris, R. J. Latent Energy of Deformation of Bisphenol-a Polycarbonate. *J. Polym. Sci. B Polym. Phys.* **26**, 433-445 (1988).

55. Donald, A. M. & Kramer, E. J. Effect of Molecular Entanglements on Craze Microstructure in Glassy-Polymers. *J. Polym. Sci. B Polym. Phys.* **20**, 899-909 (1982).
56. Wu, P. D. & van der Giessen, E. Analysis of shear band propagation in amorphous glassy polymers. *International Journal of Solids and Structures* **31**, 1493-1517 (1994).
57. Bauwens Crowet, C., BAUWENS, J. & Homes, G. Tensile yield-stress behavior of glassy polymers. *Journal of Polymer Science Part A-2: Polymer Physics* **7**, 735-742 (1969).
58. Eyring, H. Viscosity, Plasticity, and Diffusion as Examples of Absolute Reaction Rates. *J. Chem. Phys.* **4**, 283 (1936).
59. Bauwens Crowet, C. & BAUWENS, J. Effect of Thermal History on the Tensile Yield Stress of Polycarbonate in the Beta-Transition Range. *Polymer* **24**, 921-924 (1983).
60. Bauwens Crowet, C. & Homes, G. Plastic Deformation of Polymethyl Methacrylate in the Glassy State. *Academie des Sciences Comptes Rendus (Paris)* **259**, 3434 (1964).
61. Roetling, J. A. Yield stress behaviour of polymethylmethacrylate. *Polymer* **6**, 311-317 (1965).
62. Roetling, J. A. Yield stress behaviour of poly(ethyl methacrylate) in the glass transition region. *Polymer* **6**, 615-619 (1965).
63. Roetling, J. A. Yield stress behaviour of isotactic polypropylene. *Polymer* **7**, 303-306 (1966).
64. Archer, J. S. & Lesser, A. J. Shear band formation and mode II fracture of polymeric glasses. *J. Polym. Sci. B Polym. Phys.* **49**, 103-114 (2010).

65. Klompen, E. T. J., Engels, T. A. P., Govaert, L. E. & Meijer, H. E. H. Modeling of the Postyield Response of Glassy Polymers: Influence of Thermomechanical History. *Macromolecules* **38**, 6997–7008 (2005).
66. van Breeman, L. C. A., Engels, T. A. P., Govaert, L. E. & Meijer, H. E. H. Modelling thermorheologically complex phenomena in the post-yield response of glassy polymers. *13th International Conference on Deformation, Yield and Fracture of Polymers, Rolduc Abbey, Kerkrade* (2006).
67. Monnerie, L., Halary, J. & Kausch, H.-H. Deformation, Yield and Fracture of Amorphous Polymers: Relation to the Secondary Transitions. *Intrinsic Molecular Mobility and Toughness of Polymers I* 215–372 (2005).doi:10.1007/b136957
68. Cangialosi, D., Schut, H., van Veen, A. & Picken, S. J. Positron Annihilation Lifetime Spectroscopy for Measuring Free Volume during Physical Aging of Polycarbonate. *Macromolecules* **36**, 142–147 (2012).
69. Heater, K. & Agrawal, C. The effects of physical aging in polycarbonate. *J. Polym. Sci.* (1990).
70. van Melick, H. G. H., Govaert, L. E. & Meijer, H. E. H. Localisation phenomena in glassy polymers: influence of thermal and mechanical history. *Polymer* **44**, 3579–3591 (2003).
71. Lyulin, A. & Michels, M. Time Scales and Mechanisms of Relaxation in the Energy Landscape of Polymer Glass under Deformation: Direct Atomistic Modeling. *Phys. Rev. Lett.* **99**, (2007).
72. Struik, L. *Physical aging in polymers and other amorphous materials*. (Elsevier: Amsterdam, 1978).

73. Struik, L. On the rejuvenation of physically aged polymers by mechanical deformation. *Polymer* **38**, 4053–4057 (1997).
74. Lee, H.-N. & Ediger, M. D. Mechanical Rejuvenation in Poly (methyl methacrylate) Glasses? Molecular Mobility after Deformation. *Macromolecules* **43**, 5863–5873 (2012).
75. McKenna, G. Mechanical rejuvenation in polymer glasses: fact or fallacy? *Journal of Physics: Condensed Matter* (2003).
76. Isner, B. & Lacks, D. Generic Rugged Landscapes under Strain and the Possibility of Rejuvenation in Glasses. *Phys. Rev. Lett.* **96**, (2006).
77. Van Melick, H., Govaert, L., Raas, B., Nauta, W. & Meijer, H. Kinetics of ageing and re-embrittlement of mechanically rejuvenated polystyrene. *Polymer* **44**, 1171–1179 (2003).
78. Govaert, L., Van Melick, H. & Meijer, H. Temporary toughening of polystyrene through mechanical preconditioning. *Polymer* **42**, 1271–1274 (2001).
79. Govaert, L. E., Timmermans, P. H. M. & Brekelmans, W. A. M. The Influence of Intrinsic Strain Softening on Strain Localization in Polycarbonate: Modeling and Experimental Validation. *J Eng Mater Technol* **122**, 177–185 (2000).
80. Kierkels, J. T. A. *Tailoring the mechanical properties of amorphous polymers*. 138 (2006).
81. Manring, L. E. Thermal degradation of poly(methyl methacrylate). 4. Random side-group scission. *Macromolecules* **24**, 3304–3309 (2012).
82. Schmidt-Rohr, K. *et al.* Molecular Nature of the .beta. Relaxation in Poly(methyl methacrylate) Investigated by Multidimensional NMR. **27**, 4733–4745 (1994).

83. Yee, A. F. & Smith, S. A. Molecular structure effects on the dynamic mechanical spectra of polycarbonates. *Macromolecules* **14**, 54-64 (2012).
84. Hansen, M. T. *et al.* Influence of tensile stress on the phenylene flips in polycarbonate studied by two-dimensional solid-state NMR. *Macromolecules* **25**, 5542-5544 (2012).
85. Tordjeman, P., Teze, L. & Halary, J. On the plastic and viscoelastic behavior of methylmethacrylate-based random copolymers. *Polymer Engineering & ...* (1997).
86. Muzeau, E., Vigier, G., Vassoille, R. & Perez, J. Changes of thermodynamic and dynamic mechanical properties of poly (methyl methacrylate) due to structural relaxation: low-temperature ageing and modelling. *Polymer* **36**, 611-620